中国科学院大学
University of Chinese Academy of Sciences

前沿交叉科学学院
School of Advanced Interdisciplinary Sciences

中国科学院大学2025年研究生前沿交叉学科学术论坛

墙报成果汇编

中国科学院大学前沿交叉科学学院

二零二五年十一月

一、人工智能方向墙报目录

编号	姓名	题目
A01	刘子提	Automatic network structure discovery of physics informed neural networks via knowledge distillation（已发表）
A02	雷杰睿	基于潜图结构自适应的多媒体时间序列预测
A03	贾庆涛	基于迁移学习的颗粒增强铝基复合材料力学性能预测
A04	张硕	基于不确定性量化的直线压缩机行程检测和两阶段控制策略
A05	丁伯文	A Fast HDR Image Reconstruction Pipeline for Hybrid Event-Frame Camera
A06	陈家坤	融合大语言模型与岩石物理模型的智能测井分析框架
A07	李明丽	Mechanism of Ru-catalyzed C-O bond fracture in epoxy resin
A08	邵风红	基于高温压电振动传感器的信息采集系统
A09	畅皎帆	多尺度理论方法在金属有机骨架气体吸附与分离研究中的评估
A10	张瀚文	数据驱动的Cu_2O纳米花结构催化剂设计用于高效电催化CO_2制乙醇
A11	钟鸣	面向大规模网格的单射注意力神经算子

一、人工智能方向墙报目录

编号	姓名	题目
A12	高卓乐	A Low-Cost and Flexible Eye-Tracking Platform for Visual Training in Non-Human Primates
A13	刘珺	基于知识增强的大模型辅助过时测试用例修复
A14	王思淇	基于多序列磁共振成像的多分支注意力网络用于肝纤维化分期
A15	张东旭	Conditional diffusion model for arbitrary-size synthetic aperture radar image despeckling with multi-scale and dual attention mechanism
A16	王亮	MolSpectra: Pre-training 3D Molecular Representation with Multi-modal Energy Spectra
A17	黄雨培	基于视觉-惯性-声学传感器融合的水下自主定位方法
A18	陶锐	智能机器人助力大科学装置FAST运维
A19	刘洋	CityGaussian Series for High-quality Large-Scale Scene Reconstruction with Gaussians

二、集成电路方向墙报目录

编号	姓名	题目
B01	王丽霞	A-site Halogen Substitution in Lead-Free Double Perovskites for Enhanced X-ray Detection and Low-Dose Communication
B02	谭锦源	EUV光刻掩模三维模型
B03	李子涵	基于垂直双栅 IGZO TFT 的高密度三维集成 DRAM
B04	林雨澄	面向半导体超声的声-电混合异构发射芯片设计与超声医学成像调控应用研究
B05	张驰	Efficient and Stable Organic Solar Cells Achieved by Synergistic Optimization of Extended End-Capped Groups and Fluorinated Quinoxaline Central Cores in Nonfullerene Acceptors
B06	芮定海	基于掩模热-力耦合效应的高精度套刻误差补偿方法
B07	李旭帆	基于表面势的紧凑模型建立框架：驱动IGZO-DRAM的DTCO

三、量子科技方向墙报目录

编号	姓名	题目
C01	刘皓天	基于可调耦合多比特超导量子处理器直接实现高性能三量子比特门
C02	韩笑	On-surface sulfur-to-metal single-atom editing of surface-bound thiourea into adatom-bound carbene SAMs
C03	范钲威	Effective regulation of Li2MnO3-like single-component in high-nickel Li-rich layered oxides by trace Sb doping for remarkable performance improvement
C04	于琦	基于拉索控制合成手性碳纳米环中的二次谐波效应
C05	贾复麟	自组装超顺磁性纳米粒子单层膜中的无序超均匀性
C06	丛培卿	基于苯并二呋喃的低成本酯基聚合物用于有机太阳能电池
C07	梁 浩	一种新型手性L-赖氨酸碳点作为“开-关-开”荧光传感器用于汞(II)和谷胱甘肽的高效测定

四、生物制造方向墙报目录

编号	姓名	题目
D01	储晨晨	Light-Controlled Dynamic Vacancy Engineering in $mSiO_2$-PtSANs: Unveiling OV-Enhanced Oxidase-Like Mechanisms for Biomedical Applications
D02	于思琪	Design of a Rare Earth-Based Nanotherapeutic Platform for Pyroptosis-Mediated Cancer Immunotherapy
D03	高晓宇	靶向诱导肿瘤焦亡的细菌外膜囊泡用于治疗免疫冷肿瘤的研究
D04	张瑞佳	时间分辨光致发光法研究纳米纤维与蛋白质相互作用的动态自组装
D05	张小瑜	基于 ATTEC 技术降解脂滴及受损线粒体治疗肥胖相关代谢综合征的研究
D06	黄焱娟	多价金属-核苷酸纳米激动剂增强先天免疫用于肿瘤金属免疫治疗
D07	夏晨峰	基于集成磁流体装置的循环肿瘤细胞高纯度富集用于单细胞分析（英文：High-Purity Enrichment of Circulating Tumor Cells Using an Integrated Magnetic-Fluidic Device for Single-Cell Analysis）
D08	罗锐	通过分析可电离脂质空间构象实现体内靶向mRNA递送的人工智能引导LNP设计
D09	欧莹	生物信息学辅助冷冻膜保护肽设计
D10	纽一宁	A Sequential Drug Delivery System Targets the Circadian Machinery to Reverse Doxorubicin Resistance in Breast Cancer
D11	刘冠宇	Transport and biological effects of microplastics from intestine tomesentery

四、生物制造方向墙报目录

编号	姓名	题目
D12	徐慧中	多肽-核酸相互作用的定量测量与作用机制探究
D13	周伟贤	Surface structure change properties: Auto-soft bionic fibrous membrane in reducing postoperative adhesion
D14	李佳怡	Crosslinker Based Electron Microscope-based Antibody Epitope Mapping
D15	阳卉茹	以α1受体为靶点的冷冻自组装纳米药物抑制前列腺癌骨转移的研究
D16	韩渊越	调节脂肪组织胶原交联辅助干预脂肪性肝病的研究
D17	Muhammad Abrar	Hydrochar Mitigates Saturated LCFA Inhibition and Enhances DIET-Mediated Methane production
D18	贾通通	面向非正态过程的监控新方案：基于似然比检验的瑞利分布控制图（聚焦生物制造领域应用）
D19	沈耀邦	自组装多肽调控视网膜色素上皮透过性
D20	孙慧珍	生物活性水凝胶调控血管重塑
D21	张淑慧	纳米剂型奥沙利铂缓解疼痛的效应机制研究
D22	卢悄佳	基于时间生物学的病原真菌防控靶点开发
D23	韩群	新型氮代谢途径直接氨氧化细菌的多样性

基于知识蒸馏的物理信息神经网络自动结构发现

中国科学院大学 University of Chinese Academy of Sciences
前沿交叉科学学院 School of Advanced Interdisciplinary Sciences

刘子提[1,2]，刘洋[2]，闫循石[3]*，刘文[2]，聂聆[2]，郭帅旗[2]，张陈安[2]*
[1]前沿交叉科学学院，中国科学院大学，中国北京，100049
[2]空天飞行高温气动全国重点实验室，中国科学院力学研究所，中国北京，100190
[3]核能与新能源研究院，清华大学，中国北京，100084

引言 Introduction

偏微分方程（PDE）是模拟复杂物理过程的基础，通常表现出对称性和守恒定律等结构特征。虽然物理知情神经网络（PINN）可以模拟和反演偏微分方程，但它们主要依赖于外部损失函数来进行物理约束，因此很难自动发现和嵌入物理上一致的网络结构。我们提出了一种基于物理知情蒸馏的物理结构知情神经网络发现方法，该方法通过师生网络中的分阶段优化将物理正则化和参数正则化解耦。蒸馏后，使用聚类和参数重建来提取和嵌入具有物理意义的结构。拉普拉斯方程、伯格斯方程和泊松方程以及流体力学的数值实验表明，该方法可以自动提取相关结构，提高准确性和训练效率，增强结构适应性和可转移性。这种方法为结构化神经网络的高效建模和自动发现提供了新的视角。

01 研究方法 Methodology

方法基于三个步骤：物理蒸馏-结构提取-网络重建。

- 物理蒸馏：使用数据驱动方法进行物理场重建，教师网络产生包含物理信息的数据作为学生网络的有监督学习输入。
- 结构提取：学生网络稀疏化后进行结构提取，建立参数约束；
- 网络重建：根据参数间关系约束，重置可训练参数，形成新的包含结构关系的神经网络

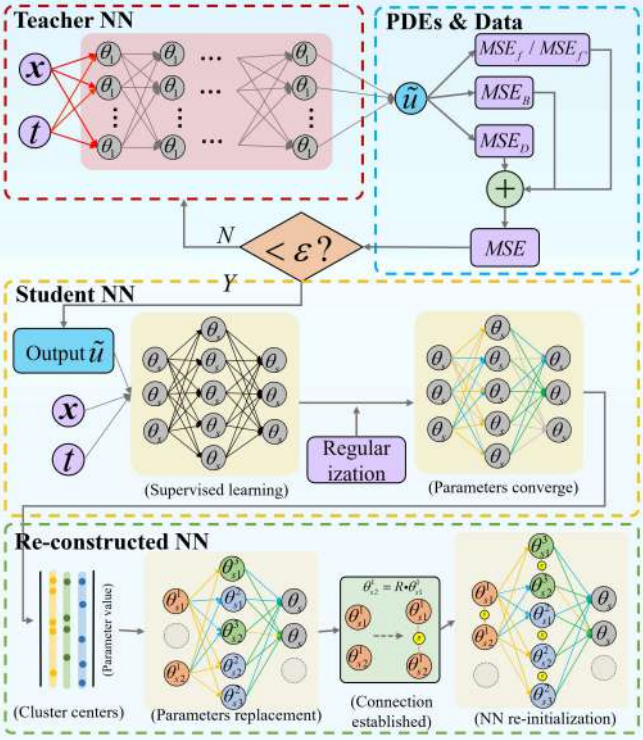

02 研究结果 Results

ψ-NN方法的聚类-提取过程：可解释性

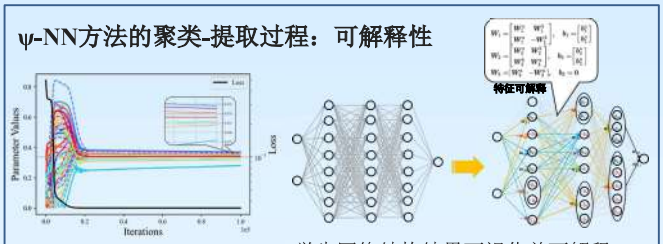

Ψ-NN的学生网络第二层的可训练参数成为聚类中心

学生网络结构结果可视化并可解释。通过结构提取和网络重建，ψ-NN包含可训练参数维度小，节省计算资源

Laplace 方程结果：强拟合能力

均方误差（MSE）对比。Ψ-NN表现出了更快的收敛速度和更低的损失精度

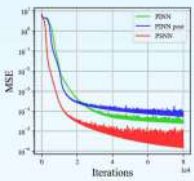

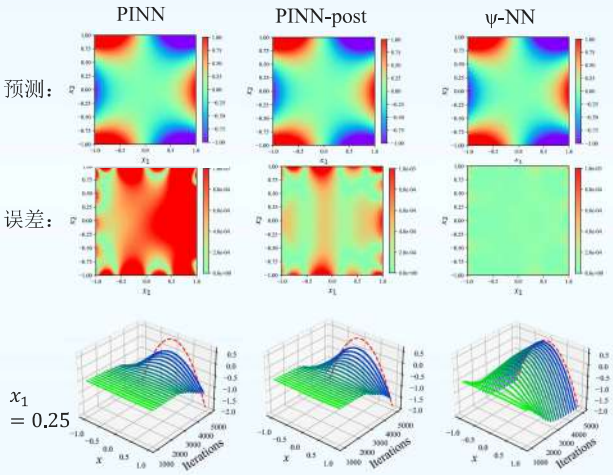

Ψ-NN在更短的迭代步数内达到真实值（红色虚线）附近

Burgers 方程结果：广适用性

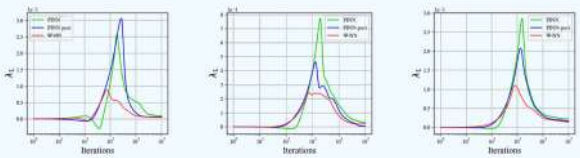

Burgers方程中，粘性系数 $\mu = \frac{0.01}{\pi}$，$\mu = \frac{0.04}{\pi}$，$\mu = \frac{0.08}{\pi}$时，ψ-NN均寻找到更短优化路径。

本文仓库：

03 研究结论 Conclusion

Ψ-NN提出一种物理知识驱动的蒸馏框架，该框架能够自动发现物理一致的网络结构，从而提升各类偏微分方程问题的准确性、效率及迁移能力。

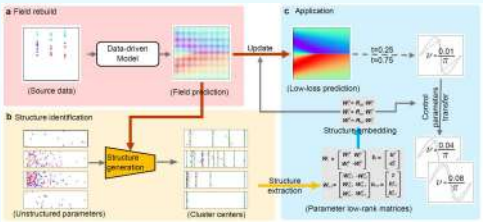

姓名：刘子提　　单位：中国科学院大学前沿交叉科学学院　　邮箱：liuizti22@mails.ucas.ac.cn

基于潜图自适应的多媒体时序预测

雷杰睿[1] 陈芳政[2] 张文剑[3] 杨卿怡[4] 张旭东[1] 唐海娜*

[1]中国科学院大学人工智能学院 [2]重庆大学计算机学院 [3]中山大学智能工程学院 [4]华中科技大学计算机科学与技术学院

引言 Introduction

随着传感器技术的进步以及现实世界中数字媒体的日益多样化，将时间序列与多种外源模态相结合对精准预测至关重要。图结构学习在时空预测中的兴起，为应对复杂的时空关联与模态异质性提供了强有力的解决方案，其应用已涵盖传统“多变量”与新兴“多模态”场景（例如通过外部文本辅助）的多媒体时序预测。尽管多媒体时间序列本身缺乏显式的先验图信息，但数据驱动的自适应图能够从数据中学习可训练的变量嵌入，进而推断出变量间复杂的隐式关联。立足“多变量”与“多模态”双视角，我们分别设计出能够适配于多媒体异质性的通用图结构。

针对“多变量”时间序列，我们提出了自适应“广义图”伴随的多视角频率学习网络（AGGA - MVFLN），该结构能够同时建模多元时间序列中的三大关键依赖关系：变量间关联、时序动态变化及潜在交互作用。为应对多图学习中固有的噪声干扰与异质性挑战，我们创新性地引入多视角频域学习方法。该方法通过挖掘“广义图”重构全局视图与局部视图中独特的时空特征，将其作为互补信息源，通过多任务损失函数的无缝整合优化广义图质量。在九个真实世界多元时间序列预测数据集上的大规模实验表明，我们提出的AGGA - MVFLN 框架在预测精度、运算效率和泛化能力方面均展现出超越SOTA的显著优势。相关工作已被多媒体领域旗舰会议ICMR2025所录用（*AGGA-MVFLN: Multivariate Time Series Forecasting via Adaptive Generalized Graph Accompanied with Multi-View Learning in Frequency Domain. In Proceedings of the 2025 International Conference on Multimedia Retrieval*）

另一方面，尽管Transformer与预训练语言模型（PLM）是多模态分析的核心支柱，然而粗粒度的模态间对齐与模态内的分布偏移现象，又会引入显著噪声。为此，我们提出解耦双自适应时序图（DDATG）——一种基于Transformer- PLM骨干的文本-时间序列双模态通用GNN插件，亮点在于：(1)解耦时间模态的局部残差项，以重构全局时间模式，增强局部-全局语义发现并丰富注意力机制；(2)显式构建文本模态的逐点上下文连接并强化聚合操作，促进跨模态语义对齐。通过跨6大经典Transformer变体和7大领域多模态时间序列预测数据集的广泛实验，我们验证了 DDATG 的有效性。相关工作已被IEEE Signal Processing Letters 录用（*Transformer-PLM Enhanced Multimodal Time Series Forecasting via Decoupled Dual-Temporal Graph Adaptation*）

01 研究方法 Methods

(A) “多变量”视角：自适应广义图伴随着多视角的频域学习

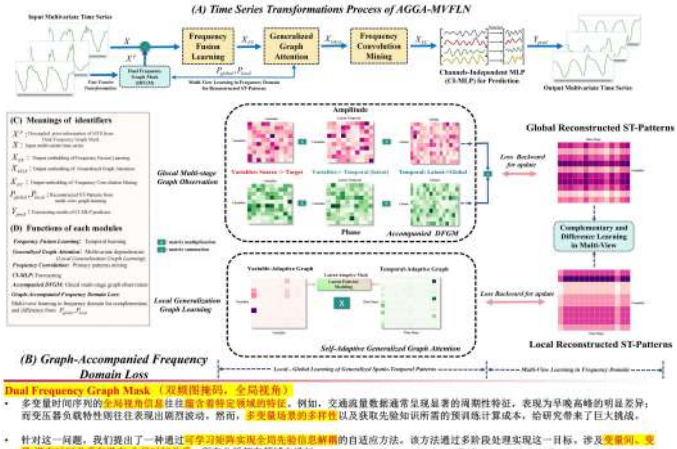

Dual Frequency Graph Mask（双频图掩码，全局视角）

- 多变量时间序列的全局视角信息往往蕴含着特定领域的特征。例如，交通流量数据通常呈现显著的周期性特征，表现为早晚高峰的明显差异；而变压器负载特性则往往表现出周期波动。然而，多变量场景的多样性以及获取先验知识所需的预训练计算成本，给研究带来了巨大挑战。
- 针对这一问题，我们提出了一种通过可学习矩阵实现全局先验信息解耦的自适应方法。该方法通过多阶段处理实现这一目标。涉及变量间、变量-潜在时间关系和潜在-全局时间关系。所有分析都在频域中进行。

频域实虚部投影

$$X(f)_{real}, X(f)_{imag} = \mathcal{F}(X(t)) = \left(\int_{-\infty}^{+\infty} X(t)\cos(2\pi ft)\,dt, -\int_{-\infty}^{+\infty} X(t)\sin(2\pi ft)\,dt\right)$$

虚部与实部解耦的双重残码法

$$X^p(f)_{real} = X(f)_{real} \times G^{real}_{vv} \times G^{real}_{vt}, \quad \in \mathbb{R}^{b\times c\times\lfloor \frac{s}{2}\rfloor+1},$$
$$X^p(f)_{imag} = X(f)_{imag} \times G^{imag}_{vv} \times G^{imag}_{vt}, \quad \in \mathbb{R}^{b\times c\times\lfloor \frac{s}{2}\rfloor+1},$$
$$X^p(t) = \mathcal{F}^{-1}(X^p(f)_{real}, X^p(f)_{imag}), \quad \in \mathbb{R}^{b\times c\times s},$$
$$X(t) = X(t) + X^p(t).$$

全局模式重建

$$P_{global} = G^{real}_{vt} \times G^{real}_{tt} \times G^{real}_{vt} \times G^{imag}_{vt} \times G^{imag}_{tt} \times G^{imag}_{vt}.$$

通过双频图掩码可视化解耦的先验信息，为从全局视角重建时空模式奠定了基础

Generalized Graph Attention（广义图注意力，局部视图）

频域融合嵌入 $X_G = \text{Dropout}(\text{Tanh}(\text{MLP}(\text{CI-MLP}(X_{real}) + \text{CI-MLP}(X_{imag}))))$

变量自适应图 $G_v = \text{Softmax}(\text{Relu}(C_{emb}W_E \times (C_{emb}W_E)^T) + C_{mask})$

时序自适应图 $G_t = \text{Softmax}(\text{Relu}(T_{emb}W_E \times (T_{emb}W_E)^T) + T_{mask})$

潜在自适应图 $X_{fusion} = X_{[1:,:,F]} \cdot G_v + X_{[1:,:,F]} \cdot G_t.$

$X_{latent} = X_E \cdot \text{Tanh}(M_{emb} \cdot (X_{fusion} - X_E)), \quad \in \mathbb{R}^{b\times c\times s}.$

局部模式重建 $P_{local} = (\sum_{-L} G_0) \times (\sum_{-L} G_t)^T.$

Graph-Accompanied Frequency Domain Loss（图伴随频域损失，多视图学习）

$$L(P_{global}, P_{local}) = \frac{1}{c\times(\lfloor \frac{s}{2}\rfloor+1)}\sum_{i=1}^{c}\sum_{j=1}^{\lfloor \frac{s}{2}\rfloor+1}|\mathcal{F}(P_{global}) - \mathcal{F}(P_{local})|.$$

采用双频图掩码作为辅助图来提升广义图的质量，因为其解耦的先验信息主要用于补偿领域特性，而最终精确的多元依赖关系则由广义图决定。

整体损失函数 $\mathcal{L}(Y_{true}, Y_{pred}) = \|Y_{true} - Y_{pred}\|_1 + \lambda\mathcal{L}(P_{global}, P_{local}) + \beta\|w\|_2$

(B) “多模态”视角：解耦双自适应时序图插件

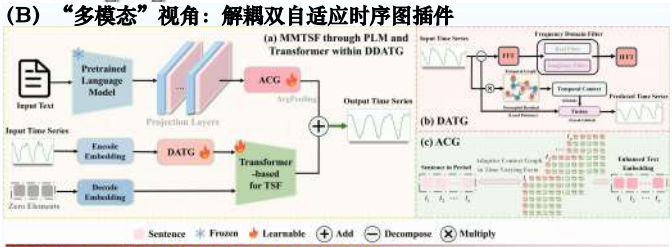

时序模态：解耦自适应时序图（DATG）

- 我们的充分发挥了频率滤波在分离特定信号分量方面的优势，并利用其频率响应特性。
- 首先应用可学习的实部-虚部分量滤波器，本质上实现了希尔伯特变换的自适应可训练变体：

$$X^h_{de} = \mathcal{F}^{-1}\{\text{Tanh}(\mathcal{F}\{X^h_{time}\}_{real} \odot \mathcal{W}_{real}) \times \mathcal{F}\{X^h_{time}\}_{real},$$
$$\text{Tanh}(\mathcal{F}\{X^h_{time}\}_{imag} \odot \mathcal{W}_{imag}) \times \mathcal{F}\{X^h_{time}\}_{imag}\},$$
$$X^h_{res} = X^h_{time} - X^h_{de}, \quad \in \mathbb{R}^{L_{ht}}$$

- 随后，我们通过可训练的时间点嵌入交互构建时序图，同时通过考虑整个回溯窗口来推导全局动态上下文权重：

$$G_{tg} = \text{Softmax}(\text{ReLU}(T_{emb} \times T^T_{emb})), \quad \in \mathbb{R}^{L_{ht}\times L_{ht}},$$
$$\mathcal{W}_{gdc} = \text{GeLU}(\text{Dropout}(X^h_{time} \times G_{tg})), \quad \in \mathbb{R}^{L_{ht}\times L_{ht}},$$
$$X^h_{tenc} = \sum_{L_{ht}}(X^h_{res} \times \mathcal{W}_{gdc}) + X^h_{res}, \quad \in \mathbb{R}^{L_{ht}},$$
$$X^f_{tenc} = \text{Transformer}(X^h_{tenc}), \quad \in \mathbb{R}^{L_{ft}},$$

- 最终的嵌入将联合全局-局部语义增强Transformer生成模态感知自注意力分布的能力。

文本模态：自适应上下文图（ACG）

- 冻结参数的 PLM 首先对文本进行编码表示，随后通过堆叠线性投影层进行微调，使文本嵌入维度与时间预测范围保持一致：

$$X^h_{tenc} = \text{MLPs}(\text{PLM}(X^h_{text})), \quad \in \mathbb{R}^{L_{ht}\times L_{ft}},$$

- 与时间图构建类似，我们为文本模态生成标记位置嵌入，并通过自转置矩阵乘法推导出上下文图：

$$G_{cg} = \text{Softmax}(\text{ReLU}(K_{emb} \times K^T_{emb})), \quad \in \mathbb{R}^{L_{ht}\times L_{ht}},$$
$$\mathcal{W}_{adc} = \text{GeLU}(\text{Dropout}(X^h_{tenc} \times G_{cg})), \quad \in \mathbb{R}^{L_{ht}\times L_{ft}},$$
$$X^f_{tenc} = \text{AvgPool}((X^h_{tenc} \times \mathcal{W}_{adc}) + X^h_{tenc}), \quad \in \mathbb{R}^{L_{ft}},$$

- 时变图表示可实现文本模态中所有时间步的上下文消息传递的完整聚合。

02 研究结论 Conclusion

(C) 对比实验：真实世界数据集上的SOTA预测性能（多变量场景）

Method	AGGA-MVFLN		FilterNet		iTransformer		MGSNet		CrossGNN		TimesNet		PatchTST		DLinear		Time-LLM	
Metrics	MAE	MSE	MAE	MSE	MAE	MSE	MAE	MSE	MAE	MSE	MAE	MSE	MAE	MSE	MAE	MSE	MAE	MSE
ETTm1	**0.389**	0.394	0.401	**0.392**	0.410	0.407	0.411	0.398	0.404	0.393	0.406	0.400	0.412	0.406	0.407	0.403	0.402	0.394
ETTm2	**0.318**	**0.277**	0.328	0.285	0.332	0.288	0.330	0.288	0.330	0.282	0.333	0.291	0.340	0.294	0.401	0.350	0.330	0.284
ETTh1	**0.428**	**0.437**	0.439	0.441	0.448	0.454	0.452	0.452	0.434	**0.437**	0.450	0.458	0.446	0.450	0.452	0.456	0.443	0.446
ETTh2	**0.398**	**0.379**	0.405	0.384	0.407	0.415	0.417	0.396	0.418	0.393	0.427	0.414	0.432	0.415	0.515	0.559	0.402	**0.379**
Weather	**0.251**	**0.220**	0.272	0.245	0.272	0.256	0.278	0.249	0.289	0.247	0.287	0.259	0.297	0.258	0.317	0.265	0.276	0.263
Traffic	**0.284**	0.500	0.310	0.463	0.296	**0.459**	0.381	0.660	0.323	0.583	0.336	0.620	0.331	0.594	0.383	0.625	0.311	0.526
Electricity	**0.257**	**0.162**	0.268	0.173	0.270	0.178	0.300	0.194	0.300	0.201	0.295	0.195	0.290	0.205	0.300	0.212	0.289	0.210
Exchange	**0.390**	**0.342**	0.400	0.561	0.403	0.360	0.430	0.399	0.395	0.345	0.443	0.416	0.435	0.404	0.414	0.354	0.400	0.355
Solar	**0.219**	0.224	0.258	0.303	0.242	**0.221**	0.257	0.245	0.271	0.265	0.263	0.259	0.221	0.270	0.251	0.291	0.241	0.229
Average	**0.326**	**0.326**	0.343	0.339	0.342	0.334	0.362	0.365	0.352	0.350	0.360	0.368	0.356	0.366	0.382	0.391	0.344	0.342

(D) 通用性：Transformer-PLM骨干的插件性能提升（多模态场景）

Backbones	Datasets	Traffic		Security		Economy		Social Good		Environment		Agriculture		Climate		Average	
	Metric	MSE	MAE	MSE	MAE	MSE	MAE	MSE	MAE	MSE	MAE	MSE	MAE	MSE	MAE	MSE	MAE
Transformer	origin	0.1770	0.3050	131.5438	6.6248	0.4900	0.6613	0.8430	0.4470	0.4730	0.5140	0.2290	0.3350	1.0790	0.8120	19.2621	1.3856
	a+DDATG	0.1725	0.2778	120.3430	6.4103	0.2303	0.3703	0.7990	0.4410	0.4450	0.4990	0.2030	0.3010	1.0190	0.7940	18.9190	1.3096
	improve	**1.98%**	**8.93%**	**1.49%**	**2.17%**	**57.09%**	**44.01%**	**5.22%**	**1.57%**	**5.92%**	**2.92%**	**11.35%**	**10.15%**	**5.56%**	**1.72%**	**1.78%**	**5.49%**
Informer	origin	0.2123	0.3695	130.0965	6.5400	0.9868	0.9590	0.8780	0.4538	0.4830	0.5211	0.4555	0.5275	1.0993	0.8230	19.1702	1.4540
	a+DDATG	0.1650	0.2770	129.3738	6.4643	0.4588	0.6245	0.8193	0.4223	0.4728	0.5198	0.3298	0.4028	1.0945	0.8165	18.9591	1.3609
	improve	**22.26%**	**25.17%**	**0.56%**	**1.16%**	**52.58%**	**33.49%**	**6.69%**	**6.94%**	**2.12%**	**0.29%**	**27.61%**	**23.65%**	**0.43%**	**1.27%**	**1.10%**	**6.40%**
Autoformer	origin	0.2125	0.2973	127.5498	5.7335	0.0713	0.2098	1.0743	0.5608	0.5573	0.5688	0.1075	0.2413	1.1978	0.8808	18.6815	1.2131
	a+DDATG	0.2038	0.2930	116.5768	5.3498	0.0550	0.1870	1.0348	0.5330	0.5543	0.5658	0.1015	0.2270	1.1693	0.8725	17.0993	1.1469
	improve	**4.12%**	**1.43%**	**8.60%**	**6.69%**	**22.81%**	**10.85%**	**3.68%**	**4.95%**	**0.54%**	**0.53%**	**5.58%**	**5.91%**	**2.38%**	**0.94%**	**8.47%**	**5.46%**
Nonstationary	origin	0.1948	0.2775	120.5435	5.6305	0.0218	0.1190	1.3830	0.5213	0.4330	0.4958	0.0853	0.2033	1.1693	0.8818	17.6901	1.1613
	a+DDATG	0.1945	0.2801	116.2510	5.3280	0.0205	0.1155	1.2370	0.4858	0.4135	0.4843	0.0847	0.1993	1.1613	0.8770	17.0546	1.1115
	improve	**0.13%**	-1.17%	**3.56%**	**5.37%**	**5.75%**	**2.94%**	**10.56%**	**6.81%**	-0.12%	**0.30%**	**0.65%**	**1.97%**	**0.68%**	**0.54%**	**3.59%**	**4.29%**
PatchTST	origin	0.2065	0.2968	114.0253	5.2633	0.0198	0.1125	1.1335	0.4960	0.4788	0.4953	0.0945	0.2075	1.2338	0.9073	16.7418	1.1055
	a+DDATG	0.1995	0.2890	111.8578	5.1725	0.0188	0.1103	0.9728	0.4273	0.4753	0.4933	0.0893	0.1998	1.2153	0.9013	16.4041	1.0795
	improve	**3.39%**	**2.63%**	**1.90%**	**1.72%**	**5.06%**	**1.78%**	**14.18%**	**13.86%**	**0.73%**	**0.40%**	**5.56%**	**3.73%**	**1.58%**	**0.63%**	**2.02%**	**2.37%**
iTransformer	origin	0.2080	0.2929	118.6463	5.6523	0.0375	0.1063	1.3185	0.4929	0.4183	0.4778	0.0913	0.2023	1.1265	0.8708	17.4062	1.1476
	a+DDATG	0.1990	0.2513	115.6408	5.4338	0.0173	0.1048	1.1743	0.4535	0.4150	0.4790	0.0867	0.1980	1.1975	0.8915	16.9615	1.1160
	improve	**4.33%**	**0.30%**	**2.53%**	**3.52%**	**1.43%**	**1.41%**	**12.27%**	**7.83%**	**0.06%**	-0.26%	**4.96%**	**2.08%**	-6.30%	-2.38%	**2.55%**	**2.76%**

(D) 可解释性实验：时空相关性捕获和跨模态异质性克服

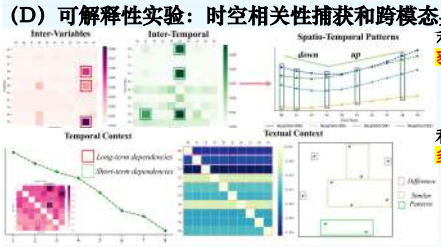

利用变量与时序自适应图联合捕获多变量场景中的时空相关性：

（1）变量间相似的趋势

（2）序列具体的波动趋势

利用时序与文本自适应图分别建模多模态场景中的异质相关性：

（1）回溯窗口的局部-全局演化

（2）全局标记到文本的对齐关系

（3）多尺度语义层次聚类

(E) 预测可视化提升（AGGA-MVFLN的广义图插件）

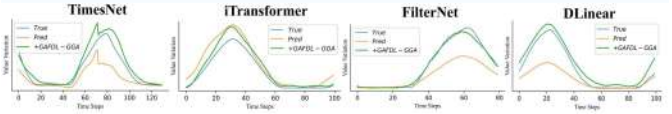

(F) 预测可视化提升（DDATG双模态图插件+Transformer-PLM）

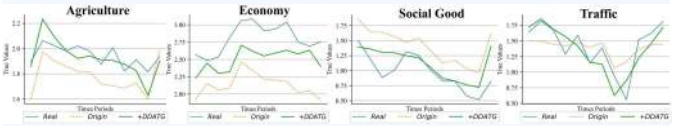

(G) 计算效率（适宜内存占用开销与高效的训练时间）

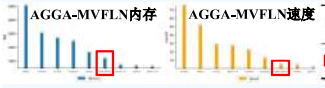

Variants	DDATG												Average
	Forecasting Length												
	48		96		192		384		768				
	Mem.	Time	Mem.	Time	Mem.	Time	Mem.	Time	Mem.	Time			
Origin	1930	0.0872	2048	0.0884	2900	0.0926	3308	0.1065	5182	0.1332			3366 / 0.1022
+DDATG	2126	0.0932	2928	0.0940	2304	0.0953	3614	0.1077	5452	0.1430			3739 / 0.1074
r(%)	9.03	6.88	8.28	6.33	8.16	4.85	6.81	3.26	5.21	4.92			8.25 / 5.00

(H) 相关研究发表引用

[1] *Jierui Lei, Fangzheng Chen, and Haina Tang. 2025. AGGA-MVFLN: Multivariate Time Series Forecasting via Adaptive Generalized Graph Accompanied with Multi-View Learning in Frequency Domain. In Proceedings of the 2025 International Conference on Multimedia Retrieval (ICMR '25). Association for Computing Machinery, New York, NY, USA, 653–661. https://doi.org/10.1145/3731715.3733272*

[2] *J. Lei, W. Zhang, Q. Yang, X. Zhang and H. Tang, "Transformer-PLM Enhanced Multimodal Time Series Forecasting via Decoupled Dual-Temporal Graph Adaptation," in IEEE Signal Processing Letters, doi: 10.1109/LSP.2025.3630087.*

本研究获得了国家自然科学基金的资助：*National Natural Science Foundation of China (NSFC) (Grant No. 52071312)*

(I) 相关研究单位特别鸣谢

姓名：雷杰睿　　单位：前沿交叉科学学院　　邮箱：leijierui24@mails.ucas.ac.cn

中国科学院大学
University of Chinese Academy of Sciences
前沿交叉科学学院
School of Advanced Interdisciplinary Sciences

基于迁移学习的颗粒增强铝基复合材料力学性能预测

贾庆涛，徐凯，常可可*
宁波材料技术与工程研究所，中国科学院大学，浙江，宁波，315201
E-mail: *changkeke@nimte.ac.cn

引言

颗粒增强铝基复合材料（PAMCs）因其高比强度和可加工性，在结构部件轻量化中有良好的应用前景。本研究提出了一种基于迁移学习的PAMCs-MP集成预测模型，克服目前PAMCs的小数据集限制，用于PAMCs**组分设计、热处理工艺优化**，实现具有复杂材料特征的PAMCs力学性能预测，为小数据限制复杂材料体系的多目标优化任务提供可行路径。

01 研究方法与模型构建

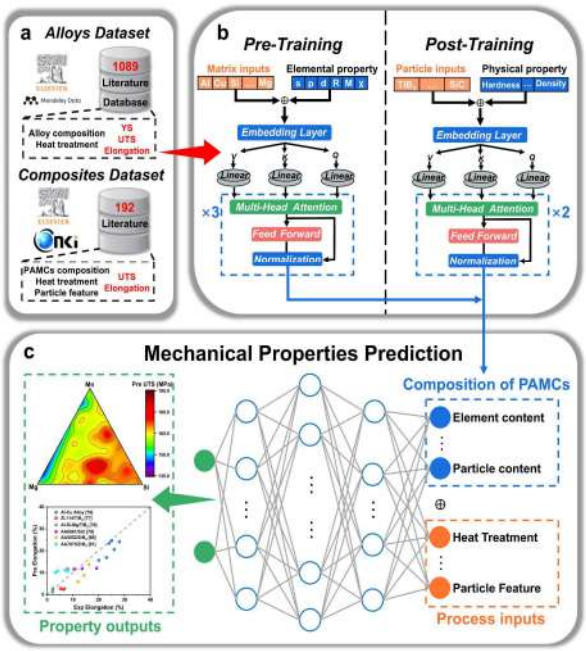

图1. 基于迁移学习的铝基复合材料力学性能预测流程图

- 结合迁移学习和Transformer基神经网络，构建铝基复合材料力学性能的多目标预测框架
- 通过自注意力机制和消融实验，识别铝合金与铝基复合材料的共性经验知识

02 模型预测效果

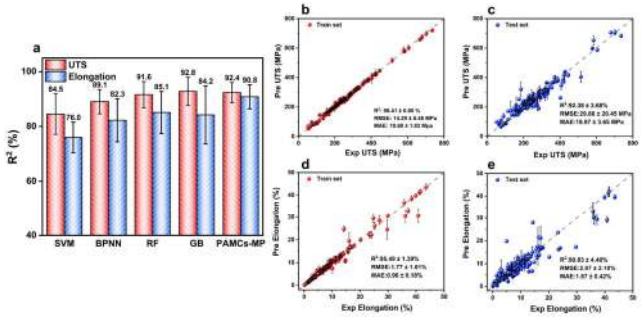

图 2. PAMCs-MP与常用机器学习模型预测精度对比

- 小数据集限制下, PAMCs-MP具有更高的预测精度；R^2分别为，抗拉强度 (92.4±3.7%)，延伸率 (90.8±4.4%)

03 模型可解释性分析

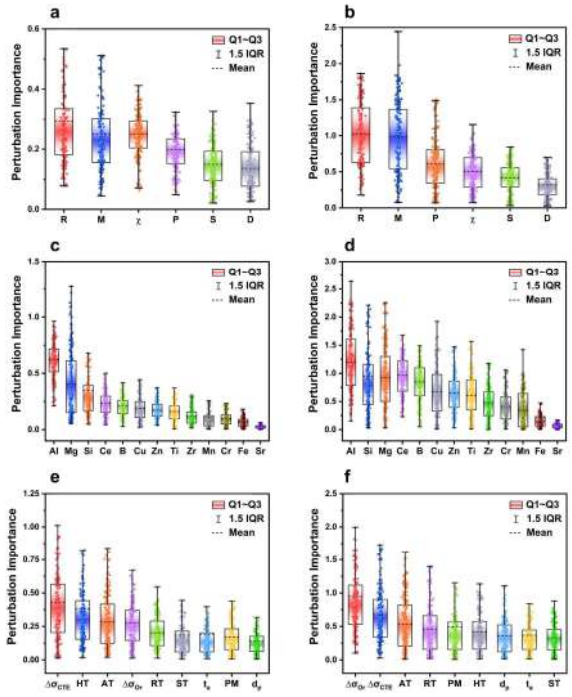

图3. PAMCs-MP输入参数的扰动特征重要性排序

- Al与Si，Mg以及变质元素之间的相互作用，对铝基复合材料的力学性能有显著影响
- 纳米颗粒引入的$\Delta\sigma_{CTE}$，$\Delta\sigma_{Or}$等位错增强机制，对显著影响PAMCs-MP的模型预测性能

04 力学性能调控

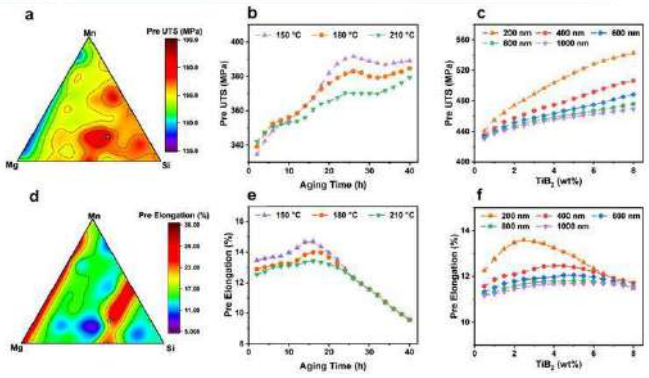

图4. 采用PAMCs-MP模型实现成分，热处理工艺设计以及增强颗粒优化

姓名：贾庆涛　　单位：中国科学院宁波材料技术与工程研究所　　邮箱：jiaqingtao@nimte.ac.cn

中国科学院大学
University of Chinese Academy of Sciences
前沿交叉科学学院
School of Advanced Interdisciplinary Sciences

基于不确定性量化的直线压缩机外推场景下两阶段行程控制策略研究

张硕，邹慧明*
前沿交叉科学学院，中国科学院大学，北京，怀柔，100049

引言 Introduction

Uncertainty quantification-based two-stage scheduling strategy for TDC control and stroke detection in linear compressors considering extrapolation scenarios

01 研究方法 Methods

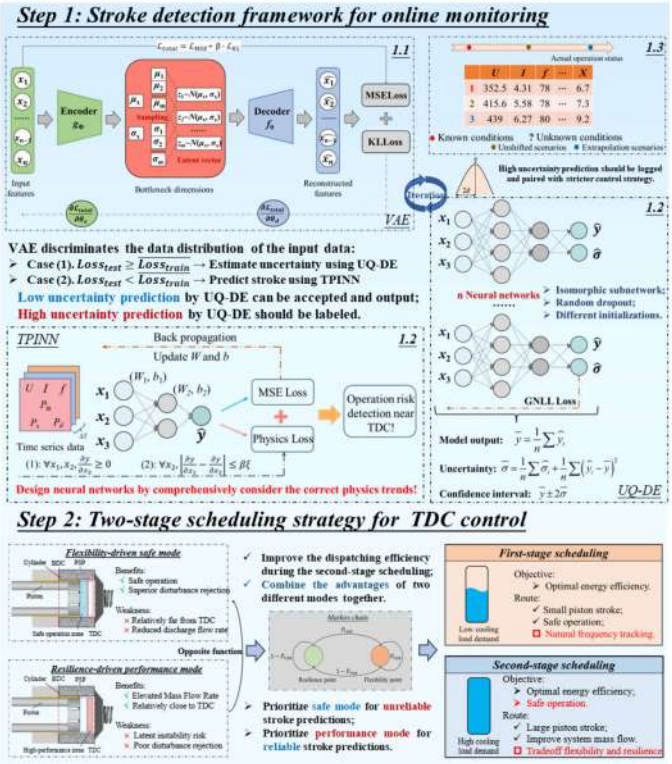

02 研究结果 Results

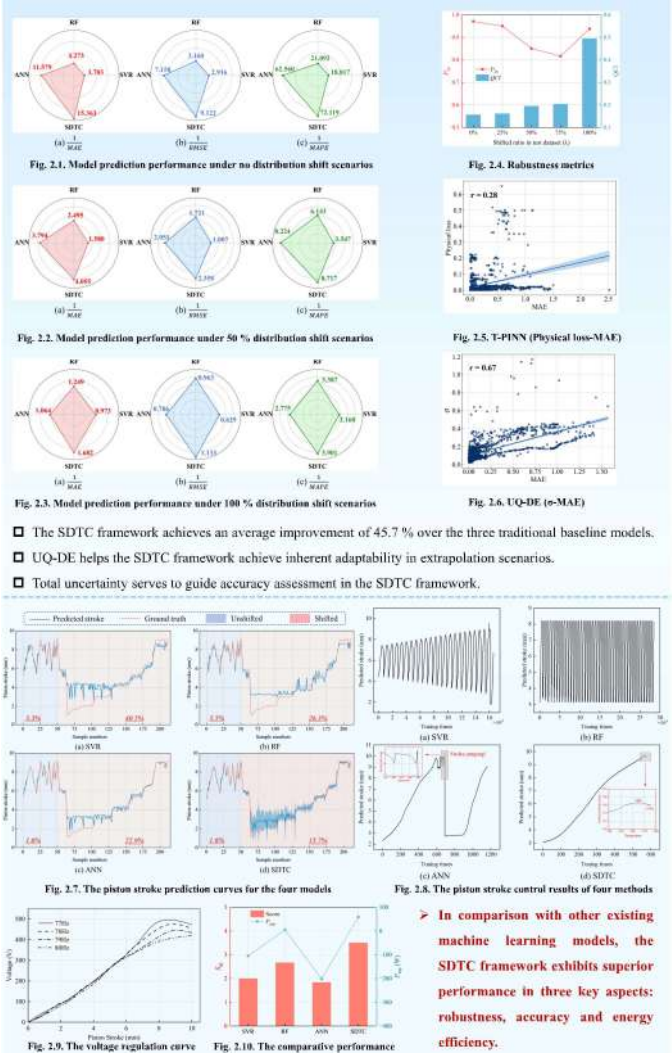

03 研究结论 Conclusion

(1) The decline in stroke prediction accuracy for linear compressors under variable operating conditions is primarily attributed to the distribution shift between training and test datasets. **Machine learning models that rely on specific inductive biases exhibit more pronounced performance degradation as the shifted ratio in the test set increases.** In contrast, **the SDTC framework maintains superior prediction accuracy over traditional models across all shift levels.**

(2) Ensemble learning methods significantly enhance the robustness of data-driven models. **A strong positive correlation exists between the magnitude of model uncertainty and prediction error. The proposed uncertainty-quantified stroke prediction model features self-adaptive confidence intervals that dynamically adjust to operating conditions.**

(3) The designed physical loss function enables the SDTC framework to effectively detect operational risks. **The Markov chain-based two-stage scheduling strategy achieved a 96.3 % average reduction in control time and a 61.5 % improvement in the average performance score compared to traditional models,** thereby significantly enhancing the operational safety of the linear compressor.

(4) The natural frequency tracking and TDC control mechanisms of SDTC framework enable superior energy efficiency and operational stability compared to traditional machine learning models. By utilizing the optimized electrical parameters derived from the SDTC framework, **the average compressor power consumption is reduced by 10.4 %.**

04 研究前景 Prospects

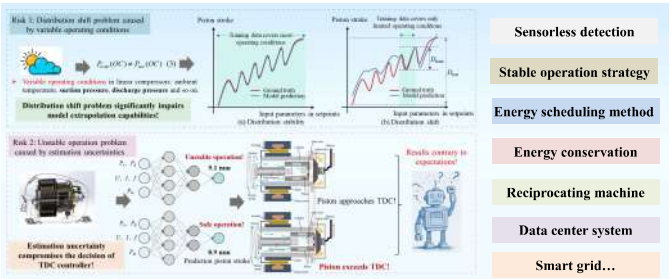

姓名：张硕　　单位：中国科学院大学前沿交叉科学学院　　邮箱：zhangshuo21@mails.ucas.ac.cn

中国科学院大学
University of Chinese Academy of Sciences

前沿交叉科学学院
School of Advanced Interdisciplinary Sciences

A Fast HDR Image Reconstruction Pipeline for Hybrid Event-Frame Camera

Bowen Ding, Xu Yang*, Shuangming Yu, Runjiang Dou and Liyuan Liu
State Key Laboratory of Semiconductor Physics and Chip Technologies, Institute of Semiconductors, Chinese Academy of Sciences, Beijing 100083, China
School of Advanced Interdisciplinary Sciences, University of Chinese Academy of Sciences, Beijing 101408, China

引言 Introduction

Hybrid event-frame cameras provide relative intensity events under HDR conditions and absolute intensity frames. Existing deep learning methods rely on synthetic data with poor generalization, while model-based computational vision methods suffer slow processing due to event-driven strategies. This paper presents a fast HDR reconstruction pipeline with Deblur, Calibration, and Fusion modules, achieving 54% faster speed than state-of-the-art computational vision methods while maintaining quality.

01 研究方法 Methods

The pipeline includes three modules executed in temporal pipelining. Deblur uses a first-order linear approximation to minimize integration errors, reducing error via linear interpolation of event intervals. Calibration aligns event and frame intensity using a mask to preserve normally exposed regions and a scale factor to correct decompression errors globally across pixels. Fusion employs nonlinear ridge regression with 3×3 windows, solving polynomial coefficients via least squares and averaging overlapping window results to reduce noise. Integral image techniques enable O(M) complexity for efficient box filter computations, ensuring parallel processing adaptability.

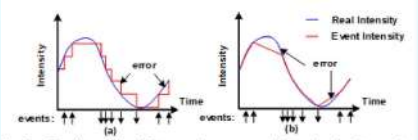

Fig. 2. The illustration of the error between actual intensity time integration and event-accumulated intensity time integration. (a) Error for Eq. (4), (b) Error for Eq. (5).

02 研究结果 Results

TABLE I
QUANTITATIVE COMPARISON OF FIVE RECONSTRUCTION METHODS

Method	HDR/AHDR MSE[a]↓	SSIM↑	Q-score↑	LPIPS↓
E2VID [9]	8.73/9.23	0.58/0.36	4.53/4.23	0.28/0.23
ECNN [19]	12.33/18.7	0.37/0.1	3.51/3.53	0.27/0.29
CF [12]	2.37/4.25	0.84/0.73	5.17/5.85	0.27/0.21
AKF [4]	**1.84**/3.94	**0.89**/0.79	6.04/**6.48**	0.14/0.11
Ours	1.89/**3.7**	**0.89/0.83**	**6.44**/6.45	**0.11/0.10**

Best results are highlighted in bold.
MSE[a] value $\times 10^{-2}$.

TABLE II
AVERAGE PROCESSING TIME AND FLOPS OF THREE METHODS

Method	HDR Time(s)	AHDR Time(s)	FLOPs ($\times 10^6$)
CF	1.11	**0.51**	31.5
AKF	2.23	1.17	60.3
Ours	**1.07**	**0.51**	**29.2**

TABLE III
ABLATION STUDY ON HDR AND AHDR DATASETS

Method	HDR/AHDR MSE[a]↓	SSIM↑	Q-score↑	LPIPS↓
Baseline	2.04/6.3	0.871/0.77	6.11/6.15	0.146/0.172
w/o Deblur	1.98/5.5	0.875/0.79	6.18/6.29	0.126/0.148
w/o Cali	1.94/4.86	0.885/0.79	6.37/6.30	0.133/0.148
w/ Eq. (4)	1.95/4.68	0.884/0.80	6.22/6.32	0.116/0.112
w/ Eq. (5)	**1.89/3.7**	**0.890/0.83**	**6.44/6.45**	**0.105/0.101**

MSE[a] value $\times 10^{-2}$.

03 研究结论 Conclusion

The proposed pipeline addresses computational overhead and noise through Deblur, Calibration, and Fusion. Deblur's linear approximation minimizes integration errors; Calibration's mask and scale factor correct decompression errors globally; Fusion's nonlinear regression and window averaging reduce event noise. Temporal pipelining enhances hardware efficiency. Experiments confirm superior metrics: on HDR/AHDR datasets, MSE, SSIM, and LPIPS are comparable or better than AKF, with 54% faster speed. Event accumulation eliminates per-event operations, integral image techniques lower complexity, and mask strategies focus on valid regions—all boosting performance. This balances accuracy and efficiency, offering a practical solution for edge devices requiring real-time HDR imaging.

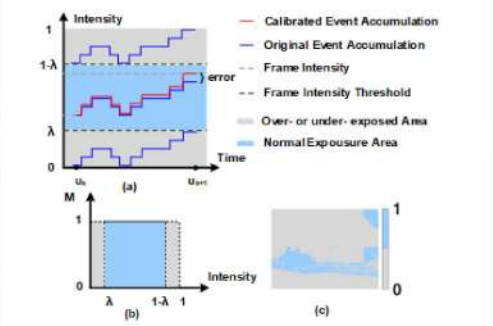

Fig. 3. The illustration of events accumulation between two LDR images, visual mask function and LDR mask. (a) Calibrated events accumulation and original events accumulation from u_k to u_{k+1}, (b) Visual mask function, (c) LDR mask example.

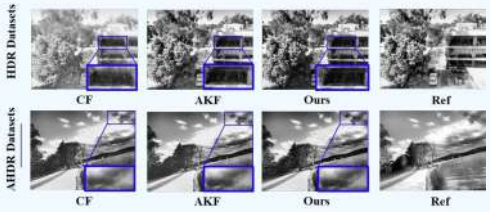

04 研究前景 Prospects

Future work will optimize adaptive mask thresholds for dynamic scenes, explore multi-scale window fusion to enhance local details, and integrate hardware acceleration (e.g., FPGA/ASIC) for sub-millisecond latency. Extensions include real-time HDR video reconstruction and mobile applications, leveraging the pipeline's low complexity to enable on-device deployment in challenging lighting conditions.

姓名：丁伯文　　单位：中国科学院前沿交叉科学学院　　邮箱：dingbowen211@mails.ucas.ac.cn

中国科学院大学
University of Chinese Academy of Sciences

前沿交叉科学学院
School of Advanced Interdisciplinary Sciences

An Intelligent Well-Logging Analysis Framework Integrating Large Language Model and Petrophysical Modeling

Jiakun Chen[1,2],Yuan Li[3]

1 University of Chinese Academy of Sciences, Beijing 101408, China
2 Institute of Geology and Geophysics,Chinese Academy of Sciences,Beijing 100029,China
3 Kazan (Volga Region) Federal University, Kazan 420111, Russia

Introduction

The development of deep learning and large-scale models has brought new possibilities to well-logging data analysis. This study introduces the next-generation large language model GPT-5.1 into the logging workflow and proposes an intelligent "GPT-5.1 + well logging" analytical framework aimed at improving efficiency and objectivity. The framework also explores the model's potential in data preprocessing, reservoir parameter evaluation, and physics-constrained 3D simulation.

01 Methods

This study selects conventional well-logging data from a representative block—such as natural gamma, resistivity, acoustic transit time, density, and neutron porosity—as the research dataset. Centered on the workflow of the "data preprocessing and feature extraction → reservoir parameter modeling → 3D resistivity response analysis," an intelligent well-logging processing framework based on a large language model is designed.

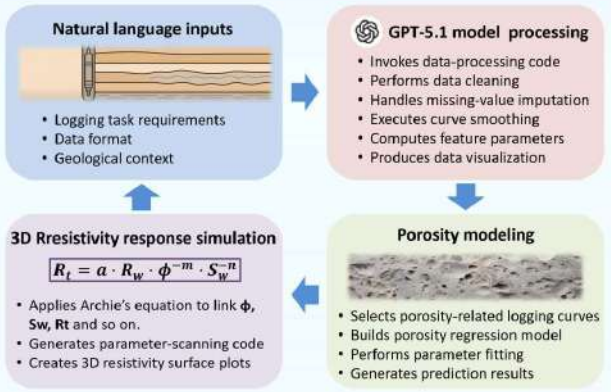

Figure 5. GPT-5.1-Driven Automatic Workflow for Well-Logging Data Processing and Interpretation

02 Results

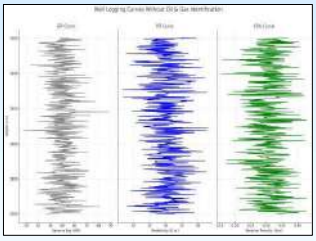

Figure 2. Well-logging curve plot

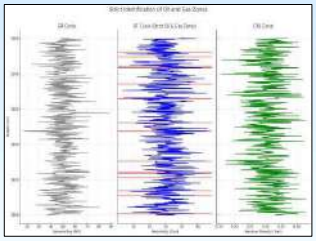

Figure 3. Feature extraction plot

In terms of data processing and interpretation, as shown in Figures 2 and 3, ChatGPT-5.1 can invoke advanced algorithms to perform online data preprocessing, addressing issues such as anomalies and missing values. After reading the dataset, it can accurately extract feature values by setting parameter ranges and generate curve plots, thereby assisting in professional tasks such as reservoir classification.

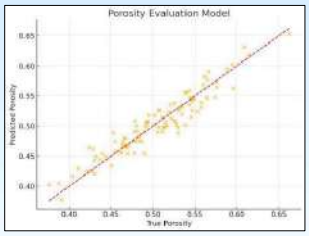

Figure 4. Porosity evaluation model based on well-logging data

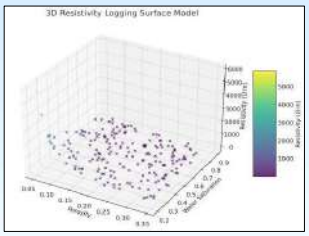

Figure 5. 3D simulation of the resistivity logging surface

In terms of model construction and evaluation, as shown in Figure 4, ChatGPT-5.1 can generate model datasets, build linear regression models, perform predictions, and produce corresponding plots. As illustrated in Figure 5, ChatGPT-5.1 is based on Archie's equation, can establish the relationship among porosity, water saturation, and resistivity and complete the visualization. The color variations represent differences in resistivity values, intuitively revealing how resistivity changes with porosity and water saturation.

03 Conclusion

This present study shows that GPT-5.1 is feasible for well-logging data processing and interpretation. The model can perform preprocessing, feature extraction, and modeling by natural-language instructions, improving efficiency and reducing manual effort. With physical constraints such as Archie's equation, the results maintain good geological and physical interpretability. However, expert review is still required, and challenges remain when applying the model to complex geological conditions and diverse reservoir types.

04 Prospects

Future research will enhance the professional intelligence and practical applicability of large language models in well logging by integrating multi-source data with industry knowledge to form a "large model + expert system" framework. Efforts will also further advance the workflow platformization and field deployment while evaluating model stability and generalization across different blocks and reservoir types to ensure reliable intelligent well-logging interpretation.

姓名：陈家坤　　单位：中国科学院地质与地球物理研究所　　邮箱：chenjiakun24@mails.ucas.ac.cn

中国科学院大学
University of Chinese Academy of Sciences

前沿交叉科学学院
School of Advanced Interdisciplinary Sciences

Ru催化环氧树脂中C-O键断裂的机理研究

李明丽，李巧枝*，高兴发*

中国科学院大学前沿交叉科学学院, 北京，101408

国家纳米科学中心, 中国科学院大学, 北京, 100190

引言 Introduction

The high chemical crosslinking in thermosetting epoxy resins poses significant challenges for degradation and recycling. Currently, a novel approach has been developed to break the inherent connecting motif of epoxy resins - alkyl C-O bonds, enabling closed-loop recovery of unmodified amine-cured epoxy resin composites. However, the mechanism of this reaction is still unclear. In this study, we use density functional theory (DFT) to compute the mechanism of C-O bond cleavage in amine-cured epoxy resin composites, with employing isopropanol as a hydrogen donor and Triphos-Ru-TMM as a catalyst, and examine the principle of isopropanol activation catalyst, the way of C-O bond breaking, the method of hydrogen supply by isopropanol and finally obtein the reaction pathway.

01 研究方法 Methods

All calculations are performed using Density Functional Theory (DFT). Gaussian09 is utilized for geometry models, while M06-2X/6-31G(d) functional is employed for optimization and vibration frequency analysis of each structure under the conditions of T = 298.15K and p = 1 bar. The transition metal Ru adopts pseudopotential group SDD, with both functionals incorporating Grimme's D3 dispersion to accurately describe weak interatomic interactions and minimize computational errors. Intrinsic Reaction Coordinates (IRC) are employed to calculate the transition states of involved reactions and validate the accuracy of computed transition states. The single point energy of each optimized structure is calculated using a double hybrid functional def2-tzvpp basis set, considering solvation effects in the gas phase environment with toluene as the reaction solvent, ensuring more precise evaluation of electron energies for each structure. The zero-point vibrational energy and thermal scaling factor at 450K (experimental temperature) are determined based on frequency calculations, enabling calculation of Gibbs free energy for each structure.

02 研究结果 Results

a)

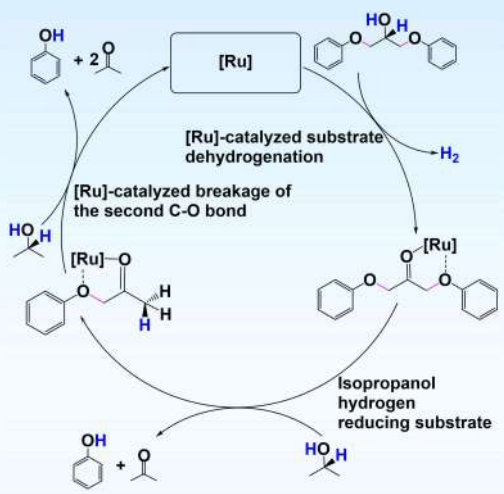

Three-step reaction pathway (1,3phenoxy-2-propanol as substrate)

1. Ru catalyze the substrate dehydrogenation, and the alcohol bond of the substrate group became to a ketone bond
2. Ru undergo a transition state to catalyze the cracking of the first C-O bond and isopropanol supply H to crack the substrate
3. Ru catalyze the breakage of the second C-O bond, and the previous steps are repeated

02 研究结果 Results

b)

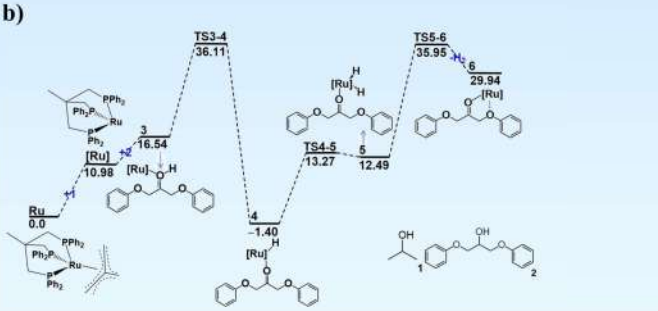

Isopropanol activate Triphos-Ru-TMM to [Ru](Triphos-Ru) with TMM is oxidized to isobutene and dissociate from Triphos-Ru-TMM.
[Ru] undergo oxidative addition and catalyze the substrate dehydrogenation

c)

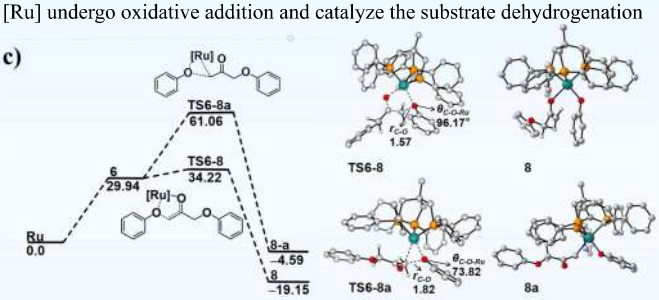

Ru catalyze the breaking of the C-O bond in five-membered transition state rather than three-membered transition state

d)

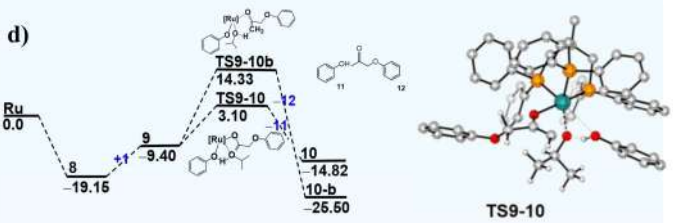

From the perspective of dynamics, releasing phenol first and then releasing phenoxyacetone is more consistent with the process of the reaction

03 研究前景 Prospects

The decisive step of overall reaction was the process of secondary dehydrogenation to reduce the substrate to acetophenone or isopropanone, so lowering the energy barrier of this step becomes the key to the study of the reaction, it will effectively increase the overall reaction rate.
The research on this mechanism will provide reasonable theoretical support for Ru-catalyzed cracking of epoxy resin and other related experiments. Additionally, it will probably stimulate more extensive and in-depth theoretical and experimental research on this reaction, in order to propose a more optimized way for the degradation of epoxy resin, and finally accelerate the process of plastic recycling.

姓名：李明丽　　单位：中国科学院大学前沿交叉科学学院　　邮箱：lim12022@nanoctr.cn

中国科学院大学
University of Chinese Academy of Sciences

前沿交叉科学学院
School of Advanced Interdisciplinary Sciences

Textured $Sr_2Nb_2O_7$ ceramics: microstructure design, high temperature ferroelectric and piezoelectric performance

Fenghong Shao [a,b], Chen Chen [a], Xiang He [a], Lu Wang [a,b], Muzaffar Ahmad Boda [a], Zhiguo Yi [a,b,*]

[a] State Key Laboratory of High Performance Ceramics and Superfine Microstructure, Shanghai Institute of Ceramics, Chinese Academy of Sciences, Shanghai 200050, China

[b] Center of Materials Science and Optoelectronics Engineering, University of Chinese Academy of Sciences, Beijing 100049, China

引言 Introduction

$Sr_2Nb_2O_7$ (SNO) ceramics are promising high-temperature piezoelectric materials due to their high Curie temperature (T_C), good thermal stability, and high electrical resistivity. However, SNO presents low piezoelectric activity (d_{33} < 1 pC/N). Here, we successfully obtain textured SNO ceramics with an orientation factor of 0.86 by microstructure regulation. The piezoelectric coefficient d_{33} of the textured SNO ceramics is increased to 3.2 pC/N, with a high T_C of 1342 ˚C, while the low-textured SNO ceramics exhibit no effective d_{33}. Meanwhile, the piezoelectric coefficient d_{33} of textured SNO ceramics maintains consistency even at 1300˚C, showing excellent thermal stability.

01 研究方法 Methods

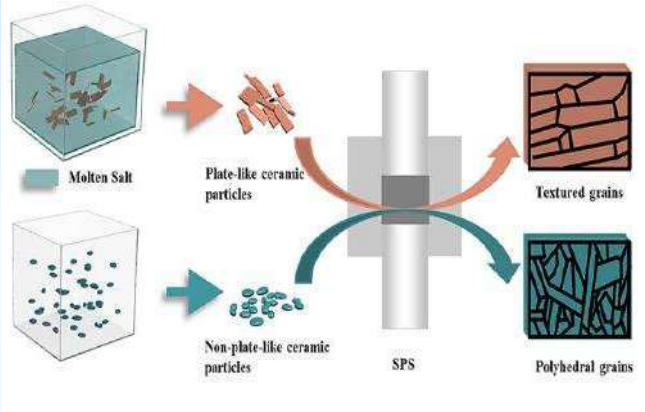

Schematic of the idea to prepare SNO ceramics with isotropic and textured microstructures, respectively.

02 研究结果 Results

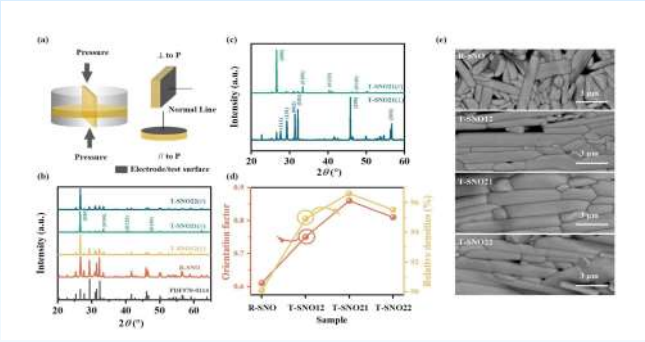

(A) Schematic diagram of two cut specimens with the normal line parallel and perpendicular to the spark plasma sintering (SPS) pressing. (B) XRD patterns of the SNO ceramic surfaces with the normal line parallel to the SPS pressing direction. (C) Comparison of XRD patterns of T-SNO21 with the normal line perpendicular and parallel to the SPS pressing direction. (D) The orientation factor and relative densities (%) of SNO ceramics. (E) SEM images of SNO ceramics.

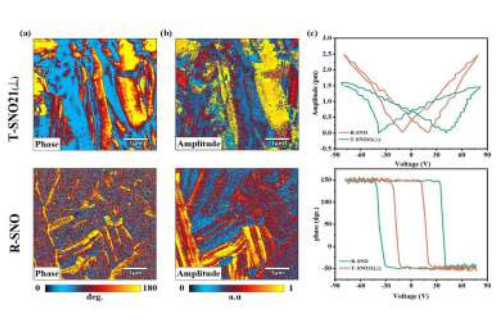

(A) Phase images, (B) amplitude images, and (C) phase switching hysteresis loops and amplitude butterfly loops of R-SNO, T-SNO21(⊥).

03 研究结论 Conclusion

In conclusion, our research has successfully synthesized perovskite-layered SNO ceramics with different microstructures, achieved through precise control over the morphology of precursor powders coupled with the application of SPS techniques. The ferroelectric domain of T-SNO21(⊥) is easier to switch. Therefore, a significant achievement of this work is the development of SNO ceramics that not only exhibit high d_{33} of 3.2 pC/N but also retain a T_C of 1342˚C. Moreover, the T-SNO21(⊥) also exhibits excellent thermal stability and high electrical resistivity. At the high temperature of 800 ˚C, the textured ceramics still maintains excellent electrical properties of large piezoelectricity (d_{33} = 3.2 pC/N) and high resistivity (ρ = 1.33×10^6 Ω·cm).The study has also provided valuable insights into the correlation between the microstructure and electrical properties of these ceramics. These contributions are expected to pave the way for further advancements in the field, specifically in the microstructure design and property optimization of layer-structured materials.

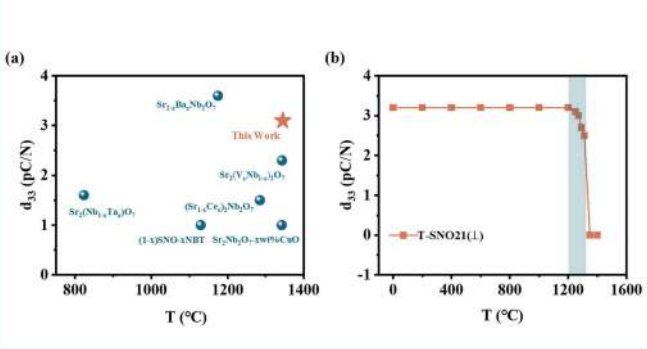

04 研究前景 Prospects

In the last few years, there has been a significant surge in the requirement for sensors capable of high-temperature vibration or sound detection, particularly in sectors such as automotive, aviation, energy production, and drilling for oil. Consequently, there is a pressing need to create piezoelectric materials that can operate across broad temperature ranges and possess enhanced thermal stability for applications at high temperatures.

姓名：邵风红　　单位：中科院上海硅酸盐研究所　　邮箱：shaofenghong22@mails.ucas.ac.cn

中国科学院大学
University of Chinese Academy of Sciences

前沿交叉科学学院
School of Advanced Interdisciplinary Sciences

多尺度理论方法在金属有机骨架气体吸附与分离研究中的评估

Chang Jiaofan, Tan ting*
1 School of Advanced Interdisciplinary Sciences, University of Chinese Academy of Sciences, Beijing 100049, China.
2 Laboratory of Theoretical and Computational Nanoscience, National Center for Nanoscience and Technology of China, Beijing 100190, China.

引言 Introduction

Gas adsorption in MOF-505 is a useful benchmark for evaluating computational accuracy. Capturing both local Cu(II) electronic effects and long-range framework interactions remains challenging. We compare periodic DFT, cluster models, QM/MM, and DFET to clarify their respective strengths and limitations for MOF-505 adsorption.

01 研究结果与讨论 Results and Discussion

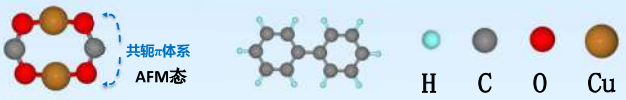

MOF-505基本结构

I. Periodic DFT method

The adsorption site of MOF:

- open Cu(II) site
- basket pocket site
- linker site

Two DFT functionals were used to calculate three adsorption sites

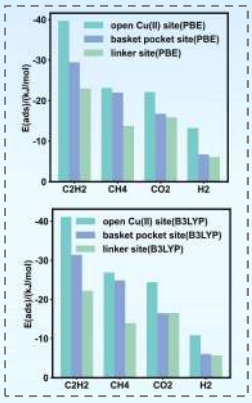

The open Cu(II) site is the optimal adsorption site in MOF-505

Comparison of the adsorption energies of four gases in MOF-505

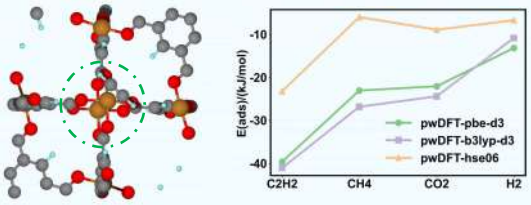

The adsorption energy trends of CH4 and CO2 calculated by different DFT functionals vary, making it impossible to determine their accuracy

II. Cluster method

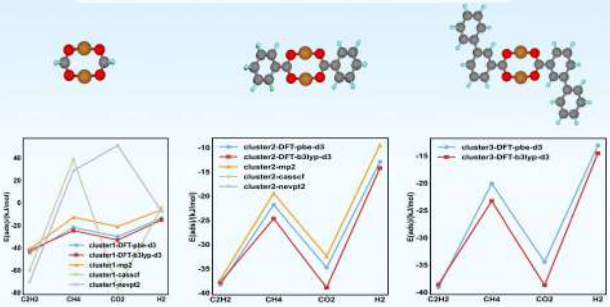

Cluster methods offer flexibility and efficiency but neglect environmental effects; small clusters give unreliable energies, while large clusters are costly with limited accuracy gain.

III. QM/MM method

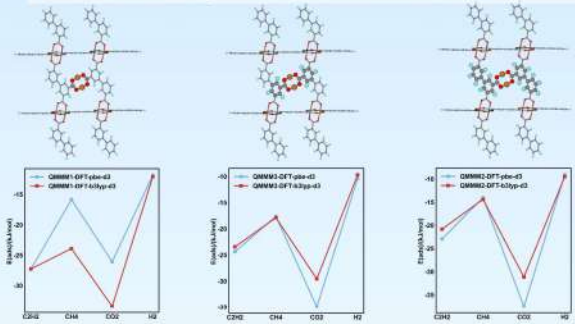

In QM/MM, the active region is treated quantum mechanically and the environment by molecular mechanics, but boundary handling and MM force fields must be accurate to avoid significant errors.

IV. DFET method

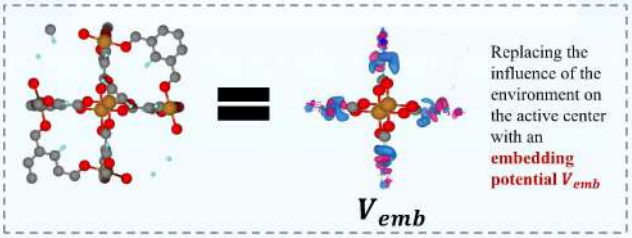

Replacing the influence of the environment on the active center with an **embedding potential V_{emb}**

Verify the rationality of the embedding potential

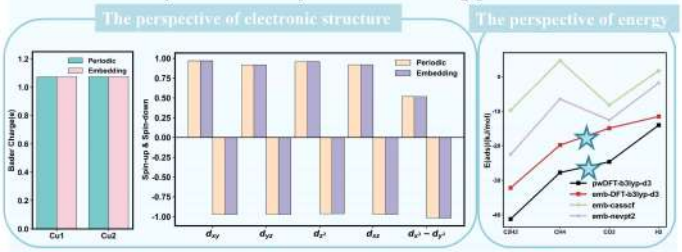

DFET accurately treats the active center with environmental effects in geometry and electronic structure, reproduces periodic DFT at B3LYP, and provides reliable selectivity at NEVPT2.

02 研究结论与前景 Conclusion and Prospects

MOF-505 is a benchmark system for testing gas adsorption methods. Periodic DFT is functional-dependent, clusters miss environmental effects, and QM/MM is boundary-sensitive. DFET offers the best balance, accurately reproducing periodic behavior and yielding reliable adsorption energies and selectivity.

姓名：畅皎帆　　单位：前沿交叉科学学院&国家纳米科学中心　　邮箱：changjf2022@nanoctr.cn

中国科学院大学
University of Chinese Academy of Sciences

前沿交叉科学学院
School of Advanced Interdisciplinary Sciences

数据驱动设计Cu_2O纳米花催化剂用于高效电催化CO_2制乙醇

张瀚文，高扬*，王斌*
国家纳米科学中心，中国科学院大学

引言 Introduction

在“碳中和”目标引领下，CO_2电催化转化为高价值化学品是能源领域的关键课题，乙醇因兼具高能量密度与广泛的工业、民生应用场景，成为该领域极具前景的目标产物。然而，传统铜基催化剂存在天然“乙烯路径”依赖，乙醇选择性长期处于低位，难以满足实际应用需求；同时，传统材料研发依赖经验主导的“试错法”，不仅研发周期长、效率低下，更无法高效遍历复杂的材料设计空间，难以揭示反应背后的构效关系。为破解双重瓶颈，本研究开创性提出一种数据驱动的理性设计新范式，通过构建“历史数据挖掘-机器学习预测-精准实验验证”的完整闭环，旨在跨越传统试错阶段，精准、高效地创制高选择性乙醇催化剂，为CO_2电催化制乙醇技术突破提供全新解决方案。

01 研究方法 Methods

为超越传统试错法的局限，本研究实施了一套严谨的数据驱动的理性设计流程。该流程始于数据库的建设：系统性地整合了已发表的科学文献与实验数据，构建了一个关于铜基CO_2还原催化剂的专用数据库，为其后的机器学习分析奠定了坚实的数据基础。

在此基础上，我们进行了系统的机器学习模型筛选，对比了XGBoost、GBDT、MLP、KNN和SVR等多种算法。结果表明，GBDT模型在我们的数据集上预测性能最优，被选定为核心分析工具。

通过对最优GBDT模型进行可解释性分析，我们成功识别出两个决定乙醇选择性的关键物理描述符——适中的*CO中间体吸附能与高的表面氧空位浓度。这两个描述符为我们提供了明确的设计蓝图：前者是启动碳-碳耦合的必要条件，而后者则是引导反应路径偏向保留C-O键、从而生成乙醇而非乙烯的关键。

基于此蓝图，我们进入了从虚拟预测到实验制备的阶段。通过精准调控湿化学合成参数，我们成功制备出了目标催化剂——具有特定三维分级结构的Cu_2O纳米花。该结构被精确设计用于同时实现上述两个关键描述符，旨在创造具有理想电子态的活性位点与丰富的缺陷结构。

最终，我们通过系统的结构表征与电化学性能测试，完成了从“数据→模型筛选→机理洞见→材料制备→性能验证”的完整研究闭环。这一流程不仅验证了我们催化剂的高性能，更充分证明了经过优化的数据驱动范式在材料设计中的强大能力。

02 研究结果 Results

本研究通过严密的证据链，充分证实了数据驱动设计范式的高效性与可靠性。模型筛选阶段，我们系统对比XGBoost、MLP、KNN等多种机器学习算法，发现GBDT模型在催化剂性能预测中表现最优,被确立为核心分析工具。通过对该模型的可解释性解析，成功识别出决定乙醇选择性的两大关键物理描述符：适中的*CO中间体吸附能与高表面氧空位浓度，为催化剂设计提供了精准靶向蓝图。

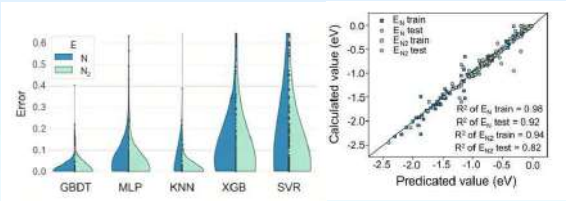

依据上述理论指导，我们通过精准的湿化学法，成功制备出目标Cu_2O纳米花催化剂。通过SEM表征证实，我们成功获得了具有三维分级结构和高比表面积的理想形貌，其为创造丰富的活性位点与缺陷提供了完美的结构基础。

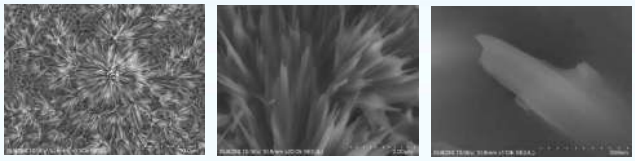

电化学性能测试结果与机器学习预测高度吻合。我们的催化剂在-1.2V(vs. RHE)的电位下，对乙醇的法拉第效率达到了50.3%。这一性能不仅显著优于传统方法制备的对比样品，更在同类研究中处于领先水平，充分证明了理性设计的巨大威力。

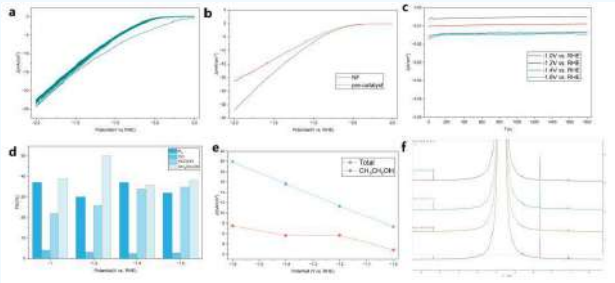

03 研究结论 Conclusion

本研究通过构建“数据→模型筛选→机理洞见→材料制备→性能验证”的完整研究闭环，成功实现了材料与方法的双重创新，为催化材料的理性设计提供了坚实范例。

在材料层面，我们成功开发出一种具有独特三维分级结构的Cu_2O纳米花催化剂。实验结果表明，该催化剂在CO_2电还原制乙醇反应中表现出卓越性能，在-1.2V(vs. RHE)电位下实现了50.3%的法拉第效率。这一性能的根源在于，其结构精准实现了机器学习所预测的两个关键描述符：适中的*CO吸附能与高的表面氧空位浓度，从而有效引导反应路径转向乙醇生成，突破了传统铜基催化剂的产物选择性限制。

在范式层面，本研究完整验证了数据驱动理性设计路径的有效性与优越性。通过系统性的机器学习模型对比与可解释性分析，我们不仅优选出GBDT模型作为精准预测工具，更成功将其识别的物理描述符转化为具体的材料设计蓝图，并最终通过实验合成获得高性能催化剂。这标志着材料研发从依赖经验的“试错”模式，向基于数据与智能的“精准设计”新模式迈出了关键一步。

综上所述，本工作不仅为CO_2资源化利用提供了一种高性能催化剂，更重要的是，它通过一个成功案例展示了人工智能与材料科学深度融合的巨大潜力，为加速未来功能材料的发现与应用奠定了方法论基础。

04 研究前景 Prospects

本工作所建立的数据驱动范式展现了广阔的拓展前景：这一智能框架可发展为通用平台，系统性加速电催化合成氨、水裂解制氢等关键能源材料的研发；通过与自动化合成、高通量测试技术深度融合，将推动材料研发向“全自动实验室”的范式变革，极大提升研发效率；最终，这一技术路径将为碳中和目标的实现持续提供先进的材料解决方案，开创能源材料研发的新纪元。

姓名：张瀚文　　单位：国家纳米科学中心　　邮箱：zhanghw2023@nanoctr.cn

中国科学院大学
University of Chinese Academy of Sciences

前沿交叉科学学院
School of Advanced Interdisciplinary Sciences

面向大规模网格的单射注意力神经算子

钟鸣[1,2]，闫振亚[1,2,*]

1，中国科学院大学前沿交叉科学学院，北京

2，中国科学院数学与系统科学研究院数学机械化重点实验室，北京

引言 Introduction

神经算子的发展虽开创了无限维函数空间映射学习的新范式，但现有基于Transformer的架构仍受限于可扩展性与精度的固有矛盾。为此，我们提出单射注意力神经算子，在保持线性复杂度的同时兼具Softmax注意力的全局表达能力。理论层面，我们严格证明了IANO在Sobolev空间中对任意连续非线性算子的通用逼近性。

01 研究方法 Methods

神经算子的单射注意力机制：我们将单射注意力机制引入神经算子框架，从而生成更平滑且保持强表达力的注意力分布，有效平衡了线性注意力与Softmax注意力的两极特性。该融合策略不仅提升了数值稳定性，更显著增强了对偏微分方程中多尺度物理结构的表征能力。

02 研究结果 Results

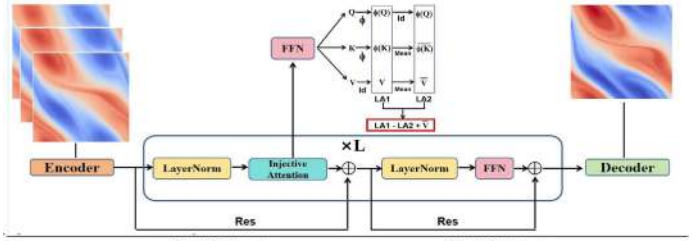

Model	Solid Mechanics		Fluid Mechanics			
	Elasticity ($\times 10^{-2}$)	Plasticity ($\times 10^{-2}$)	Airfoil ($\times 10^{-2}$)	Pipe ($\times 10^{-2}$)	Darcy ($\times 10^{-2}$)	NS ($\times 10^{-1}$)
Classic models						
FNO [18]	/	/	/	/	1.08	1.56
DeepONet [19]	9.65	1.35	3.85	0.97	5.88	2.97
U-FNO [53]	2.39	0.39	2.69	0.56	1.83	2.23
Geo-FNO [22]	2.29	0.74	1.38	0.67	1.08	1.56
U-NO [54]	2.58	0.34	0.78	1.00	1.13	1.71
F-FNO [52]	2.63	0.47	0.78	0.70	0.77	2.32
LSM [58]	2.18	0.25	0.59	0.50	0.65	1.54
Transformer-based models						
Galerkin* [24]	0.84	0.17	0.64	0.44	1.97	1.04
HT-Net [40]	/	3.33	0.65	0.59	0.79	1.85
OFormer [25]	1.83	0.17	1.83	1.68	1.24	1.71
GNOT [27]	0.86	3.36	0.76	0.47	1.05	1.38
FactFormer [26]	/	3.12	0.71	0.60	1.09	1.21
ONO [28]	1.18	0.48	0.61	0.52	0.76	1.19
Transolver* [44]	0.56	0.12	0.51	0.42	0.52	**0.94**
IANO (ours)	**0.45**	**0.07**	**0.42**	**0.39**	**0.43**	0.96

Theorem 2 (Universal Approximation of IANO). Consider a bounded domain $\Omega \subset \mathbb{R}^{d_x}$ with a Lipschitz continuous boundary. Let $r_1, r_2 \geq 0$ be integers and $q_1, q_2 \in [1, \infty)$ be real numbers. Assume

$$\mathcal{G}^\dagger : W^{r_1,q_1}(\Omega;\mathbb{R}^{d_1}) \to W^{r_2,q_2}(\Omega;\mathbb{R}^{d_2})$$

is a continuous operator acting between the corresponding Sobolev spaces. Let $\mathcal{C} \subset W^{r_1,q_1}(\Omega;\mathbb{R}^{d_1})$ be a compact set, with each function in $\mathcal{C}$ uniformly bounded in the L^∞ norm. That is, there exists a constant $M > 0$ such that

$$\|f\|_{L^\infty(\Omega)} \leq M, \quad \forall f \in \mathcal{C}.$$

Then, for any prescribed accuracy $\epsilon > 0$, there exists a parameterized IANO

$$\mathcal{G}_\theta : W^{r_1,q_1}(\Omega;\mathbb{R}^{d_1}) \to W^{r_2,q_2}(\Omega;\mathbb{R}^{d_2})$$

satisfying

$$\sup_{f \in \mathcal{C}} \|\mathcal{G}^\dagger(f) - \mathcal{G}_\theta(f)\|_{W^{r_2,q_2}} \leq \epsilon.$$

In essence, this theorem guarantees that IANO can approximate any continuous operator mapping from the Sobolev space $W^{r_1,q_1}(\Omega;\mathbb{R}^{d_1})$ to $W^{r_2,q_2}(\Omega;\mathbb{R}^{d_2})$ to arbitrary precision, provided the inputs belong to a compact and uniformly bounded subset.

03 研究结论 Conclusion

在本研究中，我们提出了单射注意力神经算子（IANO），这一新颖架构旨在突破以往基于Transformer的神经算子所面临的可扩展性与精度之间的根本性权衡。通过将注意力机制重构为单射范式，IANO在保持线性计算复杂度$O(Nd^2)$的同时，实现了与二次成本softmax注意力相媲美的高精度和全局表达能力。同时，我们严格证明了IANO在Sobolev空间的算子逼近性质。

在六个标准偏微分方程基准测试中，IANO在五项任务上达到了最先进性能，显著超越了Transolver这一强基线模型。此外，IANO的高效架构设计展现出对ShapeNet Car和AirfRANS等大规模网格数据集的无缝扩展能力，在保持卓越计算效率的同时，始终展现出优异的精度与鲁棒性。

04 研究前景 Prospects

关键发展方向包括：建立更严谨的算子学习理论框架，构建深度融合物理原理的混合模型，以及开发大规模多物理场基准数据集以推动新一代通用科学人工智能的演进。

姓名：钟鸣　　单位：中国科学院大学前沿交叉科学学院　　邮箱：zhongming22@mails.ucas.ac.cn

中国科学院大学
University of Chinese Academy of Sciences

前沿交叉科学学院
School of Advanced Interdisciplinary Sciences

A Low-Cost and Flexible Eye-Tracking Platform for Visual Training in Non-Human Primates

Zhuole G, Yinan Y, Ying F
National Center for Nanoscience and Technology, University of Chinese Academy of Sciences

引言 Introduction

Vision plays a dominant role in information acquisition in primates, making efficient visual behavior training platforms essential for visual neuroscience research. In this study, we developed a low-cost eye-tracking and training system composed of a commercial gaze-tracking device and open-source software. The platform supports visual stimulus presentation, behavioral control, and data recording on a single workstation. The system provides real-time gaze tracking with an angular resolution of approximately 0.1°, and the tracked gaze point is visually synchronous with the monkey's actual eye movements, demonstrating high spatial and temporal accuracy. Using this platform, we designed four visual stimulation training paradigms. After an average of approximately three weeks of training, the monkeys achieved success rates exceeding 90% across all tasks. These results indicate that the platform enables low-cost, highly controllable visual training with robust behavioral performance, providing an economical, flexible, and scalable solution for visual neuroscience experiments.

Keywords: visual paradigms; visual training; non-human primates; eye tracking

01 研究方法 Methods

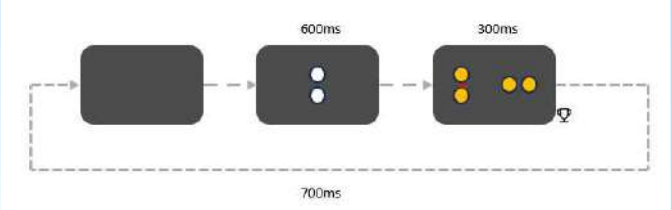

Two-alternative forced-choice (2AFC) orientation categorization task
This task aims to train monkeys to categorize lines with orientations approximating horizontal or vertical directions.

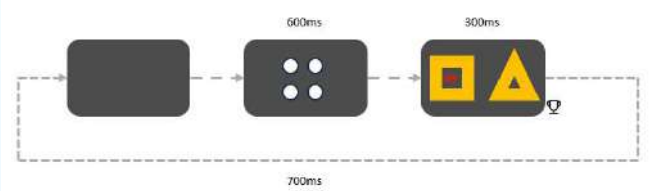

Two-alternative shape discrimination task
In this task, monkeys view shapes formed by discrete, irregularly arranged dots and choose the line drawing most similar to the dot-defined shape.

02 研究结果 Results

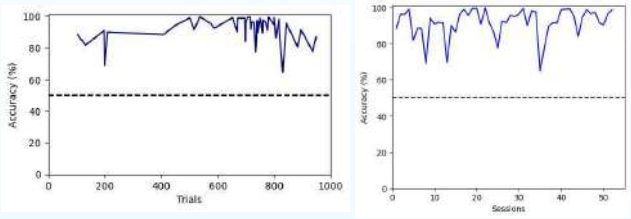

Trial success rate and session success rate

03 研究结论 Conclusion

When each training session included **600–800 trials**, task success rates were the highest. Under consistent task conditions, success rates increased gradually with the number of training sessions. After changing task conditions, monkeys typically required only **approximately two training sessions** to return to stable success rates above **90%**.

04 研究前景 Prospects

This platform offers a low-cost, high-precision tool for primate visual behavior training and can be extended to more complex visual tasks.Its open and flexible architecture enables integration with electrophysiology and cortical stimulation for studying visual coding and perception.

姓名：高卓乐　　单位：国家纳米科学中心　　邮箱：gaozl2023@nanoctr.cn

中国科学院大学
University of Chinese Academy of Sciences

前沿交叉科学学院
School of Advanced Interdisciplinary Sciences

基于知识增强的大模型辅助过时软件测试用例修复

刘珺，燕季薇，张健
中国科学院大学前沿交叉科学学院，中国科学院软件研究所，北京，100190

引言 Introduction

软件更新常导致旧测试代码失效，导致软件无法编译或安全性无法保障。虽然大语言模型具备修复测试代码潜力，但在缺乏代码背景信息（上下文）时容易出现“幻觉”，导致修复失败。本研究聚焦于通过结合静态分析和神经重排技术，自动构建**“面向测试修复的上下文”(TROCtxs)**，从而引导大模型“看懂”代码逻辑，实现对过时测试的高效、准确修复。

01 研究方法 Methods

我们提出了基于大模型的过时测试用例修复方法 ***SynTeR***[1]，该方法可以自动修复软件演化中方法级签名变更导致的过时测试用例。

❶ **知识收集：**基于静态分析收集变更相关代码上下文，如类定义、方法引用等。

❷ **知识筛选：**使用神经重排模型对收集的上下文信息按照相关性进行重排过滤。

❸ **知识增强：**将筛选后的完整上下文提供给大模型完成过时测试用例修复。

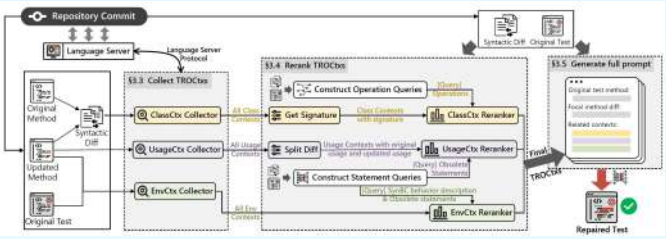

02 研究结果 Results

我们基于已有工作构建了包含136个来自真实Java项目样本的基准数据集。实验主要包括**修复有效性**以及**上下文有效性**的评估。

修复有效性

SynTeR 在基准数据集的文本一致性和语义一致性评估指标上均**全面超越基线方法**。

Approach	SPR(%)	Textual Match		
		CodeBLEU	DiffBLEU	Accuracy(%)
CEPROT	47.8%	73.5	26.3	4.4%
NAIVELLM	**100%**	81.9	44.0	28.7%
SYNTER	**100%**	**83.3**	**46.7**	**32.4%**

Approach	CPR(%)	Intent Match	
		$Repairability_{gt}$(%)	$Repairability_{ori}$(%)
CEPROT	33.3%	19.9% (*27*)	25.7% (*35*)
NAIVELLM	88.5%	69.1% (*94*)	82.4% (*112*)
SYNTER	**96.2%**	**75.0% (*102*)**	**90.4% (*123*)**

上下文有效性

SynTeR 构建的上下文 (TROCtxs)帮助大模型的**幻觉问题大幅减少了 57.1%**。

Approach	Common Hall.	Outdated Hall.	Total
NAIVELLM	6	8	14
SYNTER	**0 (-100.0%)**	**6 (-25.0%)**	**6 (-57.1%)**

03 研究结论 Conclusion

知识收集

SynTeR 创新性地结合**静态分析**与**神经重排**技术，有效解决了在全代码仓库范围内精准锁定“面向修复上下文”的难题。

知识增强

SynTeR 基于上下文的知识增强范式，能有效引导大模型攻克**语法变更**带来的测试修复挑战，实现高准确率的自动化修复。

04 研究前景 Prospects

- **测试用例修复任务扩展：**未来工作可以从方法级的语法变更修复扩展至更复杂的类级别语义变更修复场景。
- **其它软件工程任务扩展：**本方法的有效性也证明了静态分析技术对于大模型赋能软件工程（LLM4SE）的研究具有重要作用。

[1] Jun Liu, Jiwei Yan, Yuanyuan Xie, Jun Yan and Jian Zhang: Fix the Tests: Augmenting LLMs to Repair Test Cases with Static Collector and Neural Reranker. ISSRE 2024 (CCF-B，已发表)

姓名：刘珺　　单位：前沿交叉科学学院、软件研究所　　邮箱：liuj2022@ios.ac.cn

中国科学院大学
University of Chinese Academy of Sciences

前沿交叉科学学院
School of Advanced Interdisciplinary Sciences

基于多序列磁共振成像的多分支注意力网络用于肝纤维化分期

王思淇，曾谦，韩东，刘文韬*
国家纳米科学中心，中国科学院大学，北京，中国，100190

引言 Introduction

肝纤维化是导致肝硬化和肝细胞癌的主要风险因素。准确分期对治疗计划和预后评估至关重要。尽管肝活检是目前的临床金标准，但其高成本和相关并发症限制了其在常规监测和筛查中的效用。因此，亟需可靠的影像学非侵入性分级方法。磁共振成像(Magnetic Resonance Imaging，MRI) 可以提供丰富的多相信息，以全面可视化不同对比度阶段的纤维化相关组织变化。

01 研究动机

1. 多序列MRI信息的有限利用

多序列 MRI 承载了不同的病理生理信息（如肝细胞功能、血流灌注、纤维化结构改变等），然而现有模型往往将这些序列视作独立输入，或仅以简单的通道级堆叠进行特征融合，未能挖掘序列间的互补关系及序列特异性特征，从而导致信息利用不足和表征能力受限。

2. 融合阶段信息冗余

传统的多序列融合策略多采用简单拼接或全局加权方式，易引入大量冗余特征，并弱化与肝纤维化高度相关的病灶特征。在这种“无差别融合”策略下，模型难以有效聚焦临床关键区域，限制了分期判读的准确性。

02 研究方法

多分支注意力网络旨在利用多序列 MRI 进行精确的肝纤维化分期。该框架由三个主要组成部分组成。(1) 多分支预训练编码器提取初级特征；(2) 自适应分支融合模块学习分支的动态模态权重，减少冗余干扰；(3) 捕获每个分支内序列内时间依赖性的轻量级注意力瓶颈。

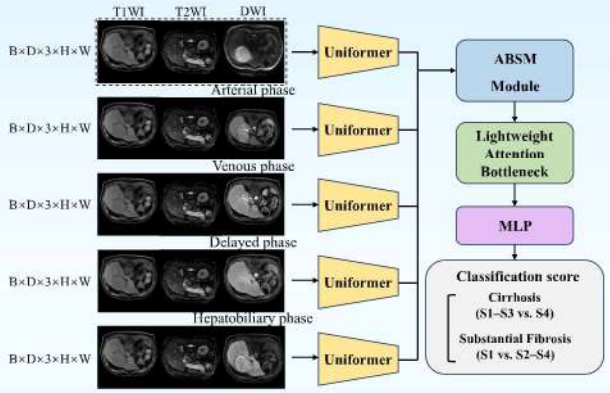

图1 多分支注意力网络（Multi-branch attention network，MBAN）的整体架构

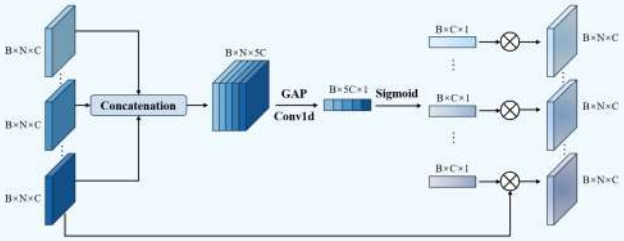

图2 自适应分支融合模块（Adaptive branch-wise fusion module，ABSM）的示意图

03 研究结果

训练集			验证集			测试集		
供应商	中心	病例数	供应商	中心	病例数	供应商	中心	病例数
A	A	130	A	A	20	A	A	40
B	B1	170	B	B1	20	B	B1	40
B	B2	60	B	B2	20	B	B2	40
-	-	-	-	-	-	C(新)	C(新)	70

表1 训练/验证/测试集的结构划分

方法	肝硬化: S1–S3 vs. S4		实质纤维化: S1 vs. S2–S4	
	AUC	ACC	AUC	ACC
四分类交叉熵损失	0.6112	56.67%	0.6281	71.67%
从0训练的Uniformer	0.5682	53.33%	0.5985	70.00%
不应用ABSM	0.6184	60.00%	**0.7215**	68.33%
MBAN	**0.6699**	**60.00%**	0.7141	**73.33%**

表2 所提方法及变体在使用五折交叉验证的验证集上的量化性能

MBAN	内部测试集 (来自中心A、B1、B2)		外部测试集 (来自中心C)	
	肝硬化: S1–S3 vs. S4	实质纤维化: S1 vs. S2–S4	肝硬化: S1–S3 vs. S4	实质纤维化: S1 vs. S2–S4
AUC	0.7831	0.8450	0.6605	0.3723
ACC	72.00%	80.83%	41.43%	82.86%

表3 所提方法在使用五折交叉验证的内部/外部测试集上的量化性能

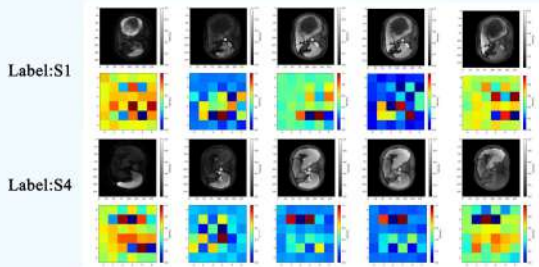

图3 五个编码器分支的注意力图，以输入体积的中间切片为例

04 总结

所提出的MBAN 框架结合了多分支编码器、自适应分支融合模块和轻量级注意力瓶颈，以有效捕获序列内和序列间依赖关系，同时抑制冗余信息。模型在非创伤性肝纤维化评估方面表现出强劲性能，为临床决策提供可靠支持。

姓名：王思淇　　单位：国家纳米科学中心　　邮箱：wangsq2021@nanoctr.cn

中国科学院大学
University of Chinese Academy of Sciences

前沿交叉科学学院
School of Advanced Interdisciplinary Sciences

Conditional diffusion model for arbitrary-size synthetic aperture radar image despeckling with multi-scale and dual attention mechanism

张东旭、李庆*

中国科学院微电子研究所，中国科学院大学，北京

引言 Introduction

Synthetic aperture radar (SAR) inherently encounters speckle noise as a characteristic challenge. Current methods are often limited by complex speckle-noise patterns and the size of SAR images. To further improve despeckling quality and adapt arbitrary-size SAR images, we propose a novel method based on aconditional diffusion model coupled with a multi-scale and dual attention mechanism.

01 研究方法 Methods

1. This paper proposes a conditional diffusion model with multi-scale and dual attention mechanism for arbitrary-size SAR image despeckling, which obtains a balance between speckle noise removal and structure preservation.
2. Multi-scale and dual attention mechanism is constructed to extract multi-scale and global information within SAR image and establish long-range dependencies between position and channel features, ensuring a broader perspective and more accurate distinction between structure textures and speckle noise.
3. Using smooth mean noise estimation across overlapping patches to guide the sampling process, the proposed method is capable of handling arbitrary-size SAR image.

02 研究结果 Results

Visual comparison of simulated and real SAR image

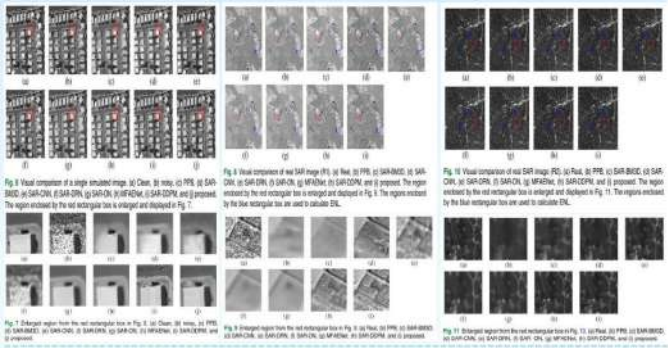

PSNR and SSIM comparison of simulated SAR image

Table 1 Comparison of PSNR (dB) and SSIM values on simulated SAR images.

Method	PSNR (dB)	SSIM
PPB	16.2878	0.5089
SAR-BM3D	22.2065	0.6171
SAR-CNN	17.2881	0.5223
SAR-DRN	18.2769	0.6028
SAR-ON	21.1378	0.6349
MFAENet	22.8024	0.6849
SAR-DDPM	22.8024	0.6874
Proposed	**23.5969**	**0.7343**

Note: bold values indicate the best objective index.

Ablation study

Table 3 Ablation study of the parameter r.

r	32	64	128	256
PSNR	21.3123	23.1912	22.5231	22.5922

Table 2 Comparison of despecking effects of different modules.

Module	Different combinations			
Multi-scale module	—	+	—	+
Dual attention module	—	—	+	+
PSNR	22.9154	23.0273	23.1369	23.5969

Objective valuation index comparison of real SAR image

Table 6 Objective valuation index comparison of real SAR image R1.

Method	ENL			EPD-ROA	
	Region 1	Region 2	MoR	HD	VD
Original	16	8	1	1	1
PPB	**925**	363	0.9459	0.9114	0.9066
SAR-BM3D	341	**722**	0.8839	0.9234	0.9170
SAR-CNN	135	84	0.8397	0.9191	0.9139
SAR-DRN	93	87	0.9710	0.9176	0.9164
SAR-ON	643	568	0.9810	0.9145	0.9155
MFAENet	724	668	0.9932	0.9123	0.9134
SAR-DDPM	114	89	0.9696	0.9195	0.9154
Proposed	125	98	**0.9921**	**0.9301**	**0.9280**

Note: bold values indicate the best objective index.

Table 7 Objective valuation index comparison of real SAR image R2.

Method	ENL			EPD-ROA	
	Region 1	Region 2	MoR	HD	VD
Original	28	14	1	1	1
PPB	**423**	**399**	0.9567	0.9440	0.9497
SAR-BM3D	240	294	0.8815	0.9234	0.9170
SAR-CNN	185	199	0.8337	0.9191	0.9139
SAR-DRN	87	90	0.9752	0.9176	0.9164
SAR-ON	243	265	0.9810	0.9145	0.9155
MFAENet	324	338	0.9832	0.9121	0.9144
SAR-DDPM	109	113	0.9898	0.9195	0.9154
Proposed	115	124	**0.9913**	**0.9603**	**0.9613**

Note: bold values indicate the best objective index.

03 研究结论 Conclusion

We propose a novel despeckling method for arbitrary-size SAR images based on a conditional diffusion model coupled with multi-scale and dual attention mechanisms. The proposed method harnesses the strong modeling capability of the diffusion model to restore the original clear scene accurately. Utilizing multi-scale and dual attention mechanisms, the proposed method has a border perspective and a more accurate distinction between structure textures and speckle noise.

Experiment results conducted on simulated and real images demonstrate that the proposed method obtains a better balance between effective despeckling and the preservation of structure details. To address the practical issue that SAR image size is often arbitrary, smooth noise esti mation across overlapping patches is used to guide the sampling process. Through this, the proposed method can process fixed-size patches in each iteration, but yield a complete result without requiring post-sampling patch fusion. Experiment results conducted on arbitrary-size images demonstrate the practicality of the proposed method.

04 研究前景 Prospects

1. Enhances the accuracy of tasks such as target recognition, environmental monitoring, and disaster situation assessment.
2. It features strong practicality and provides technical support for the in-depth application of SAR images in scenarios such as urban and rural planning and agricultural and forestry resource

姓名：张东旭　　单位：中国科学院大学前沿交叉科学学院　　邮箱：zhangdongxu221@mails.ucas.ac.cn

中国科学院大学
University of Chinese Academy of Sciences

前沿交叉科学学院
School of Advanced Interdisciplinary Sciences

多模态光谱信息赋能 3D 分子表征预训练

王亮[1,2] 柳绍祯[1] 荣钰[3] 赵德丽[3] 刘强[1,2] 吴书[1,2] 王亮[1,2]

1 中国科学院自动化研究所 2 中国科学院大学人工智能学院 3 达摩院

ICLR

MolSpectra: Pre-training 3D Molecular Representation with Multi-modal Energy Spectra

01 摘要 Abstract

建立分子的 3D 结构与其能量状态之间的关系被证明是学习 3D 分子表征的有效方法。然而，现有工作局限于将分子能量状态描述为经典力学中的连续势能函数，忽视了分子能量在量子力学视角下呈现的离散能级结构信息。对此，中科院自动化所团队提出了 MolSpectra 方法，利用多模态能谱增强 3D 分子表征预训练，融入能级结构知识，提升分子性质预测和分子动力学建模能力。

02 研究背景 Background

1. Denoising as learning a force field.

去噪（Denoising）已成为 3D 分子表征学习中一种重要的预训练目标。这种方法具有物理可解释性，因为它已被证明等价于学习分子力场：

$$\mathcal{L}_{\text{Denoising}}(\mathcal{M}) = \mathbb{E}_{p(\boldsymbol{x}|\boldsymbol{x}_0)p(\boldsymbol{x}_0)}\|\text{GNN}_\theta(\boldsymbol{x}) - (\boldsymbol{x} - \boldsymbol{x}_0)\|^2 \simeq \mathbb{E}_{p(\boldsymbol{x})}\|\text{GNN}_\theta(\boldsymbol{x}) - (-\nabla_{\boldsymbol{x}} E(\boldsymbol{x}))\|^2,$$

从本质上讲，这表明在 3D 几何结构与能量态之间建立关系，是学习 3D 分子表征的一条有效途径。

2. 以往的研究仅通过去噪（denoising）来**模拟经典力学下的势能函数**，而**忽略了量子力学视角下的能级结构**。而这些能级结构可以通过分子光谱来测量。

3. 不同类型的分子光谱揭示了不同的能级结构。例如，红外（IR）光谱揭示的是振动能级，而紫外-可见（UV-Vis）光谱揭示的是电子能级。

03 主要贡献 Contribution

1. 我们提出了 MolSpectra，首次将分子光谱引入分子表征学习中。
2. 我们提出了 SpecFormer，一种具有高表达能力的多光谱编码器，并结合了用于光谱表征学习的掩码片段重建目标（masked patches reconstruction objective）和光谱-结构跨模态对比学习目标（contrastive objective）。

04 研究方法 & 实验 Methods & Results

1. MolSpectra 的设计思路，同时利用分子 3D 结构和分子光谱进行预训练。

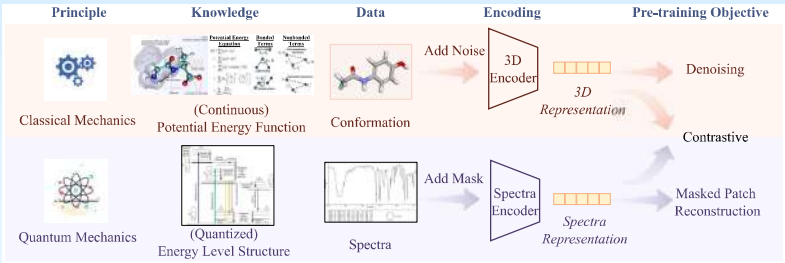

2. MolSpectra 的预训练框架与模型架构。

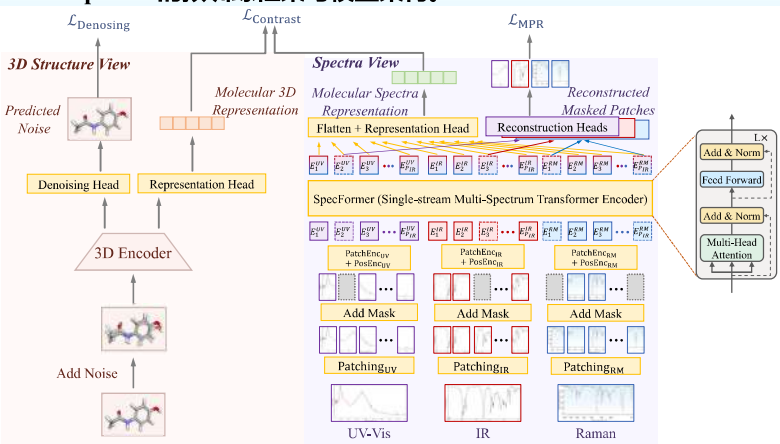

MolSpectra 包含三个子目标：去噪目标（denoising objective）和掩码片段重建目标（masked patches reconstruction objective）分别引导 3D 结构模态和光谱模态的表征学习；而对比目标（contrastive objective）则用于对齐两种模态的表征。

3. 光谱内（左）与光谱间（右）依赖。

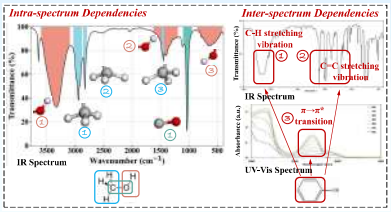

分子性质预测

I. Performance (MAE↓) on benchmark datasets.

	μ (D)	homo (meV)	lumo (meV)	gap (meV)	U_0 (meV)	U (meV)	H (meV)	G (meV)
EGNN	0.029	29.0	25.0	48.0	11.00	12.00	12.00	12.00
PaiNN	0.012	27.6	20.4	45.7	5.85	5.83	5.98	7.35
SphereNet	0.025	22.8	18.9	31.1	6.26	6.36	6.33	7.78
TorchMD-Net	0.011	20.3	17.5	36.1	6.15	6.38	6.16	7.62
Transformer-M	0.037	17.5	16.2	27.4	9.37	9.41	9.39	9.63
SE(3)-DDM	0.015	23.5	19.5	40.2	6.92	6.99	7.09	7.65
3D-EMGP	0.020	21.3	18.2	37.1	8.60	8.60	8.70	9.30
Coord	0.016	17.7	14.7	31.8	6.57	6.11	6.45	6.91
MolSpectra	**0.011**	**15.5**	**13.1**	**26.8**	**5.67**	**5.45**	**5.87**	**6.18**

模型代码： https://github.com/AzureLeon1/MolSpectra

作者邮箱： liang.wang@cripac.ia.ac.cn

姓名：王亮 单位：中国科学院自动化研究所 邮箱：liang.wang@cripac.ia.ac.cn

中国科学院大学
University of Chinese Academy of Sciences

前沿交叉科学学院
School of Advanced Interdisciplinary Sciences

基于视觉-惯性-声学融合的水下机器人自主定位方法

黄雨培，李朋，马绍轩，闫帅铮，谭民，喻俊志，吴正兴*
中国科学院自动化研究所，北京，100190

引言 Introduction

针对现有视觉或视觉-惯性同步定位与建图系统在水下环境中性能显著下降的问题，本工作提出了一种紧耦合视觉-惯性-声学传感器融合方法，引入声学速度传感器多普勒测速仪（Doppler Velocity Log, DVL）以提供额外的运动信息，实现了多模态传感器信息的充分有效融合，显著提升了水下机器人的定位精度

01 研究方法 Methods

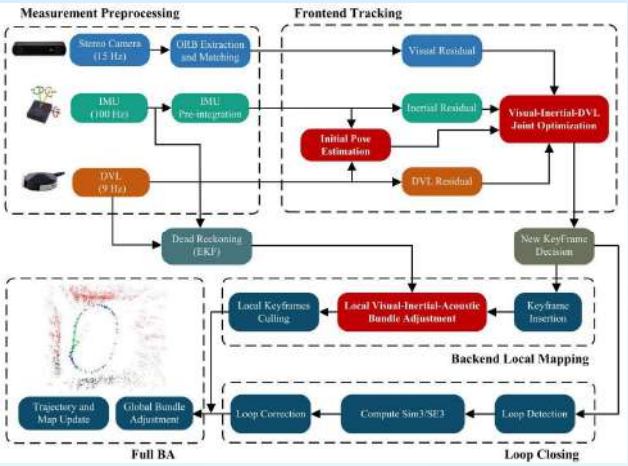

视觉-惯性-声学融合定位方法框架

02 研究结果 Results

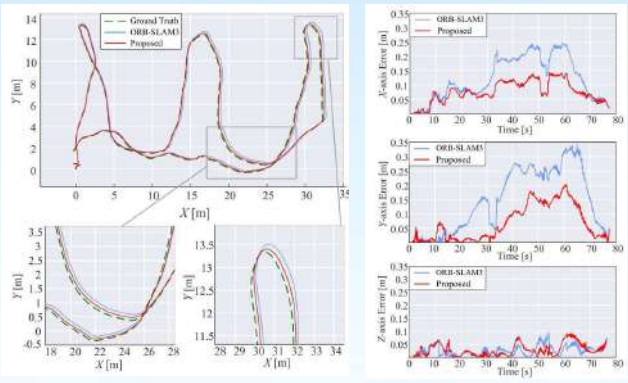

仿真环境的定位轨迹与误差曲线

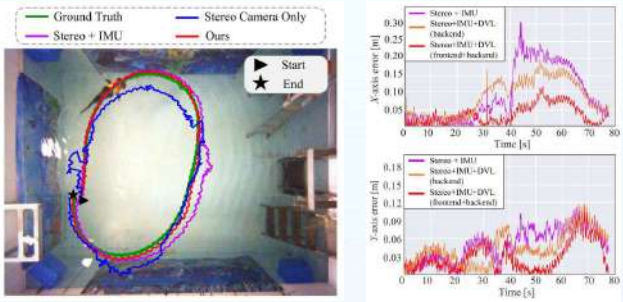

真实水下环境的定位轨迹与误差曲线

03 研究结论 Conclusion

- 在后端局部建图过程中执行视觉-惯性-声学联合优化可以获得更准确的轨迹，使得真实世界的水下数据集序列的ATE误差指标平均下降约20%
- 在前端跟踪和后端局部建图过程中均执行多模态信息融合，所提方法估计的轨迹将ATE误差指标平均降低30%以上

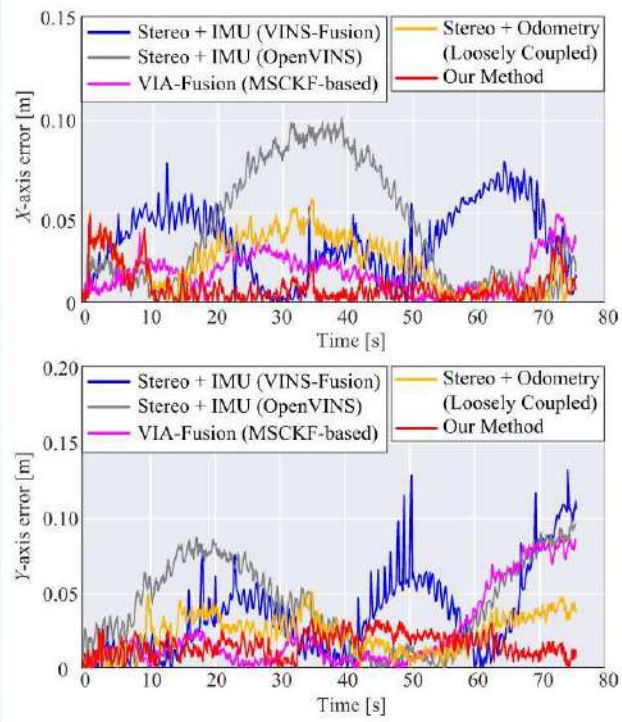

04 研究前景 Prospects

- 基于相机-声呐成像系统的水下机器人融合定位
- 基于多传感器融合与三维高斯表示的水下场景稠密重建
- 利用语义信息与模仿学习的机器人智能导航

姓名：黄雨培　　单位：中科院自动化所　　邮箱：huangyupei2021@ia.ac.cn

中国科学院大学
University of Chinese Academy of Sciences

前沿交叉科学学院
School of Advanced Interdisciplinary Sciences

FAST激光靶标自主维护机器人系统

陶锐，景奉水*，侯骏，邢时雨，付一宸，范俊峰*，谭民
中国科学院自动化研究所，中国科学院大学，北京，100190

引言 Introduction

五百米口径球面射电望远镜（FAST）是目前全球单口径最大、综合灵敏度最高的射电望远镜，其建成标志着我国在大科学装置领域达到世界领先水平，对前沿天文学研究具有重大意义。在FAST日常运维中，主动反射面上约2225个激光靶标需定期维护与校准，目前仍依赖人工高空作业，存在效率低下、安全风险高等突出问题，亟需实现自动化替代

FAST及其靶标

01 任务描述 Task Description

- ✓ 靶标的维护任务本质是**在狭小空间内对非标准化的靶标螺栓进行拆装**的过程
- ✓ 须构建**能够在反射面上移动**的机器人系统，该机器人系统应能够**适应靶标的装配环境、实现高精度的感知**以及**鲁棒的操作**

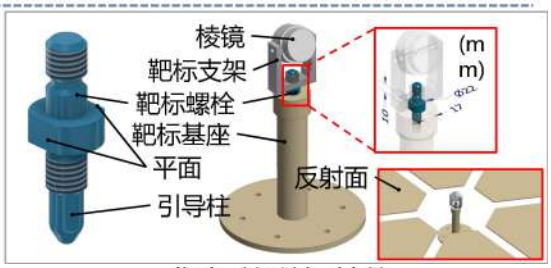

靶标的详细结构

02 研究方法 Methods

- ✓ 设计了轻量化、异构双臂移动维护机器人系统
- ✓ 为克服靶标更换过程中的关键挑战，提出了三项关键技术：
  - 设计了一种能够实现侧向旋拧和反力矩抵消的机器人**旋拧末端执行器**
  - 提出了一种基于特征点提取和随机匹配的**位姿测量框架**，用于具有高反光、弱纹理特点的靶标的位姿测量
  - 针对靶标拆装过程，提出基于空间约束的大倾角环境下的鲁棒**螺纹装配策略**

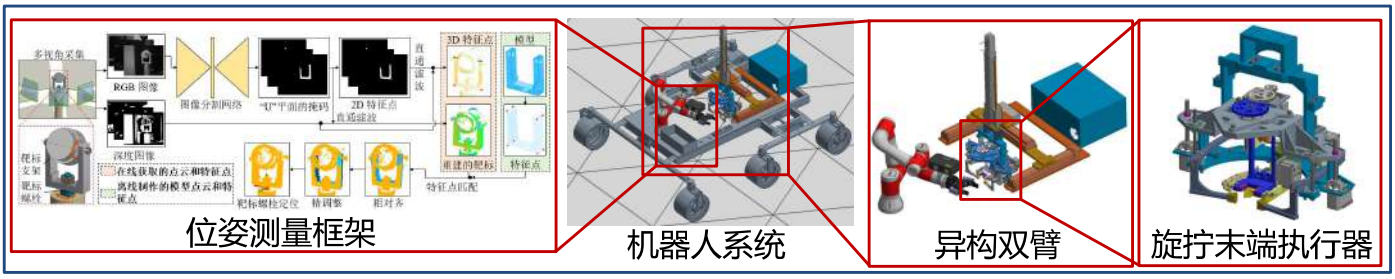
位姿测量框架
机器人系统
异构双臂
旋拧末端执行器

03 研究结果 Results

- ✓ 通过丰富的实验测试各方法的性能，并在实际FAST场景下测试了机器人系统的有效性

模拟倾斜反射面环境测试

实际FAST场景应用

作者联系方式

Tao Rui, Jing Fengshui*, Hou Jun, Xing Shiyu, Fu Yichen, Fan Junfeng, Tan Min. APTMRS: Autonomous Prism Target Maintenance Robotic System for FAST. **IEEE Transactions on Automation Science and Engineering**, 2024, 22: 4022-4038.

姓名：陶锐　　单位：中国科学院自动化研究所　　邮箱：taorui2020@ia.ac.cn

中国科学院大学
University of Chinese Academy of Sciences
前沿交叉科学学院
School of Advanced Interdisciplinary Sciences

CityGaussian: 基于高斯辐射场的高质量大规模场景高效重建

刘洋，关赫，罗传琛, 毛钟楷, 彭君然*, & 张兆翔*
模式识别实验室，中科院自动化研究所，中国科学院大学

Introduction

Though existing 3D reconstruction techniques have achieved great success with single object or small scenes. But under complex large-scale scenes, they usually face serious challenges from computation and storage overhead, training instability, and low surface accuracy problems. Our **CityGaussian-V2** establishes an **efficient parallel** training paradigm with **controllable** memory overhead, while achieving **SOTA** in rendering and geometric quality.

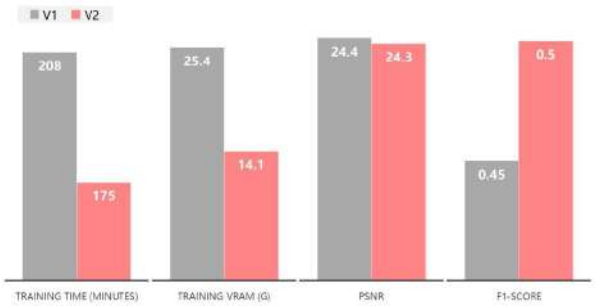

Method

Stars 1k Forks 77

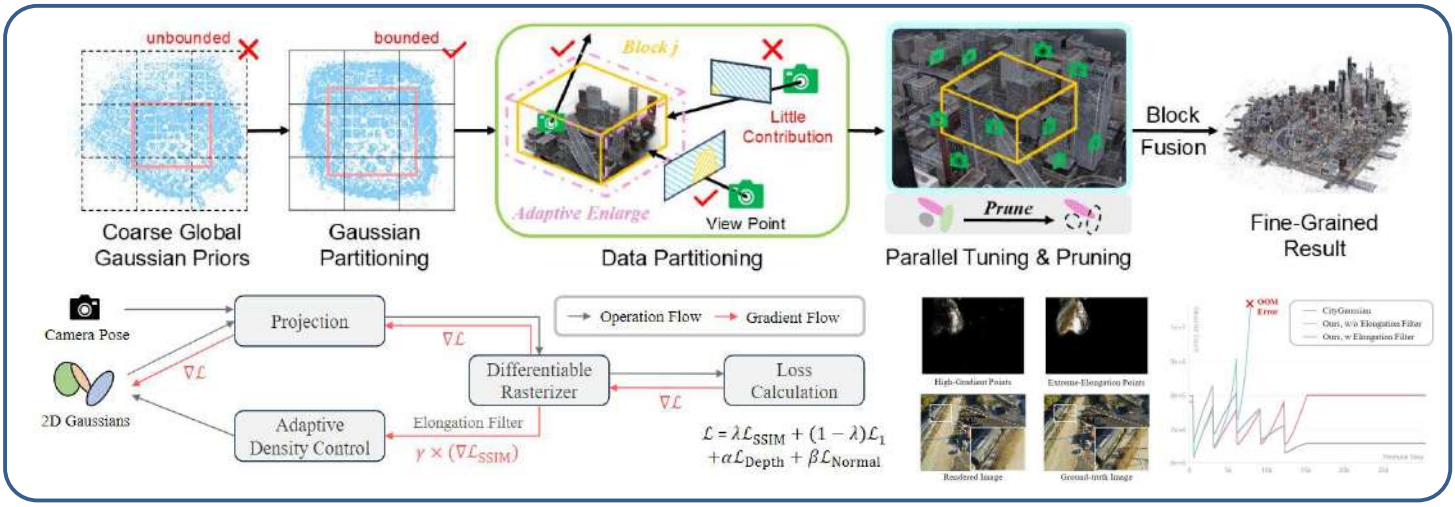

Results

Methods	GauU-Scene				MatrixCity-Aerial				MatrixCity-Street			
	PSNR↑	P↑	R↑	F1↑	PSNR↑	P↑	R↑	F1↑	PSNR↑	P↑	R↑	F1↑
NeuS	14.46	FAIL	FAIL	FAIL	16.76	FAIL	FAIL	FAIL	12.86	FAIL	FAIL	FAIL
Neuralangelo	NaN	NaN	NaN	NaN	19.22	0.080	0.083	0.081	15.48	FAIL	FAIL	FAIL
SuGaR	23.47	0.570	0.292	0.377	22.41	0.182	0.157	0.169	19.82	0.053	0.111	0.071
GOF	22.33	0.370	0.390	0.374	17.42	FAIL	FAIL	FAIL	20.32	0.219	0.473	0.300
2DGS	23.93	0.553	0.446	0.491	21.35	0.207	0.390	0.270	21.50	0.334	0.659	0.443
CityGS	24.75	0.522	0.405	0.453	27.46	0.362	0.637	0.462	22.98	0.283	0.689	0.401
Ours	24.51	0.576	0.450	0.501	27.23	0.441	0.752	0.556	22.24	0.376	0.759	0.503

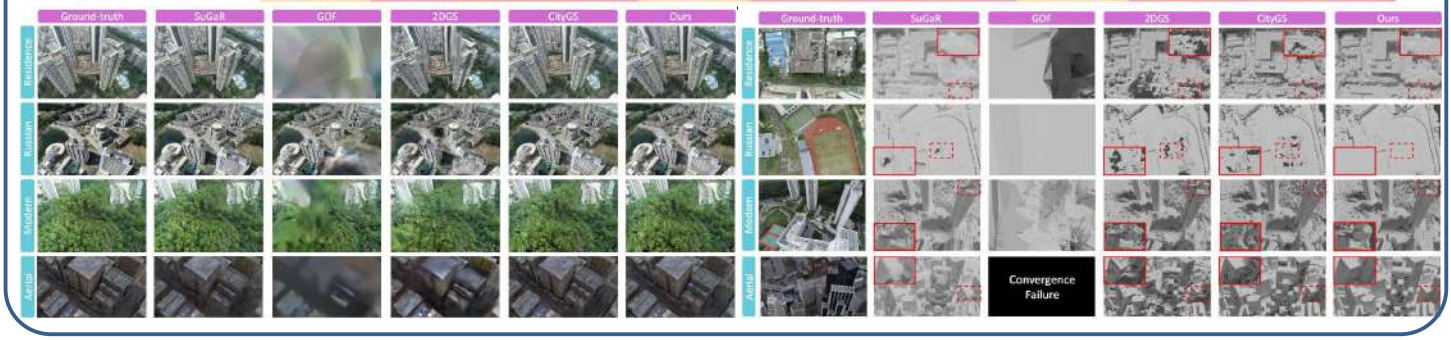

中国科学院大学
University of Chinese Academy of Sciences

前沿交叉科学学院
School of Advanced Interdisciplinary Sciences

High-Performance Lead-Free Double Perovskites for Low-Dose X-ray Detection and Communication

王丽霞，魏文娟*，孟祥悦*

前沿交叉科学学院，中国科学院大学，北京

引言 Introduction

在强电磁干扰和屏蔽环境中，传统无线通信技术面临显著挑战，影响设备监控和应急响应。X射线通信（XCOM）因其优异的穿透性和定向性，成为解决这些问题的潜在方案。然而，X射线信号在传播过程中容易衰减，尤其在厚屏蔽材料和长距离传输下，现有探测器在低剂量条件下的响应性较差，限制了低功耗X射线通信的应用。

01 研究方法 Methods

本研究采用无铅双金属钙钛矿材料（I-PA）$_4AgBiI_8$，通过碘替代A位BA^+阳离子的$-CH_3$基团来提升其极化性。材料的晶体结构和光学带隙通过X射线衍射（XRD）和紫外-可见吸收光谱（UV-Vis）进行确认。介电常数和激子结合能的测量结果表明，材料具有增强的电荷分离能力；同时，电荷迁移-寿命积（μτ）用于进一步评估其电荷收集性能。在X射线探测实验中，器件表现出灵敏度为1.79×10^4 $\mu C\cdot Gyair^{-1}\cdot cm^{-2}$，检测下限为0.012 nGyair s^{-1}，展现了优异的探测性能。最后，低剂量X射线通信实验中，成功通过18.8 mm铝屏蔽材料传输了摩尔斯电码和像素图案信号，证明了该材料在强屏蔽环境中的通信潜力。

02 研究结果 Results

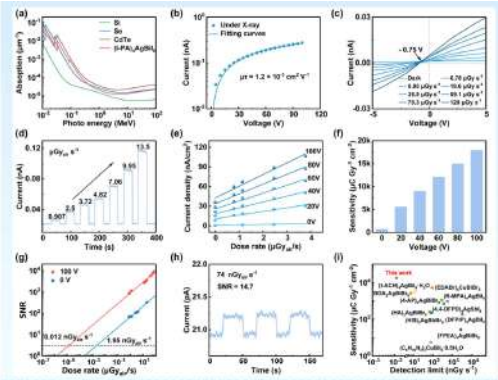

器件灵敏度达到 1.79×10^4 $\mu C\cdot Gyair^{-1}\cdot cm^{-2}$，最低检测限为 0.012 nGyair s^{-1}，证明其在低剂量X射线探测中的优异性能。

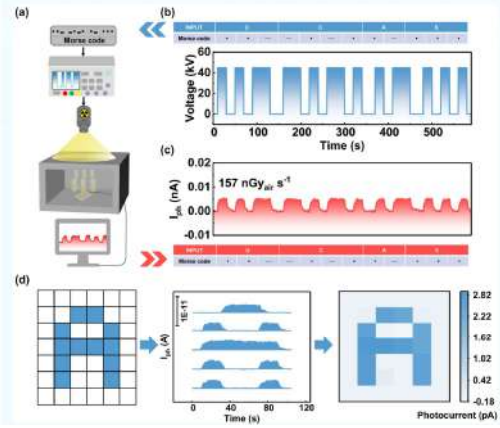

研究成功实现了低剂量（4.54 μGy/s）X射线通信，使用18.8 mm铝屏蔽材料，在强屏蔽环境下传输了摩尔斯电码和像素图案信号。

03 研究结论 Conclusion

本研究通过引入A位卤素替代策略，成功设计并合成了无铅双金属钙钛矿材料（I-PA）$_4AgBiI_8$，并优化了其在低剂量X射线探测与通信中的应用性能。研究结果表明，材料的创新设计显著提升了多个方面的性能：

1.卤素替代对材料结构与光电性能的影响：引入碘元素后，A位的极化率显著增强，进一步加强了分子间的伦敦色散力，从而打破了原有的非共价相互作用平衡，导致晶格发生自发的结构畸变，以适应新的相互作用模式。结构畸变提升了材料的介电常数，有效降低了激子结合能，增强了电荷分离能力。

2.双金属钙钛矿材料在X射线探测中的器件性能：μτ值提高至1.2×10^{-3} $cm^2\cdot V^{-1}$，显著提升了电荷收集能力，器件的灵敏度达到了1.7868×10^4，检测限低至0.012 nGyair s^{-1}，远优于现有的混合双钙钛矿材料，证明了其在低剂量X射线探测中的卓越性能。

3.低剂量X射线通信及其在紧急通信中的应用：研究成功实现了低剂量（4.54 μGy/s）X射线通信，利用18.8 mm铝屏蔽材料，在强屏蔽环境下成功传输了摩尔斯电码和像素图案信号。这表明，（I-PA）$_4AgBiI_8$材料在密闭或屏蔽环境下的低剂量X射线通信中具有重要的应用潜力。

综上所述，（I-PA）$_4AgBiI_8$材料通过A位卤素替代和结构优化，展示了在低剂量X射线探测与通信方面的显著优势，提供了极端环境中信息交换与探测的创新平台。

04 研究前景 Prospects

（I-PA）$_4AgBiI_8$无铅双金属钙钛矿材料凭借高灵敏度和低检测限，在低剂量X射线探测和通信中展现出巨大潜力，特别在医疗成像、核安全监测和信息通信等领域。其高灵敏度提升精度，低检测限确保在低辐射和高干扰环境下的有效性，未来有望推动高精度探测技术的发展。

姓名：王丽霞　　单位：中国科学院大学前沿交叉科学学院　　邮箱：wanglixia23@mails.ucas.ac.cn

中国科学院大学
University of Chinese Academy of Sciences
前沿交叉科学学院
School of Advanced Interdisciplinary Sciences

高精度快速EUV掩模三维效应模型

谭锦源，李梓棋，董立松*，韦亚一*
前沿交叉科学学院，中国科学院大学，中国，北京，101408
中国科学院微电子研究所，中国，北京，100029

引言 Introduction

极紫外（EUV）光刻是应用于制造7nm及其以下节点超大规模集成电路的主流光刻技术。EUV光刻具有倾斜照明、吸收层厚等特点导致系统产生了复杂的掩模三维（Mask Three Dimension, M3D）效应（如阴影效应）。这一效应会显著影响EUV光刻的精度，因此在 EUV 光刻仿真中必须 M3D 效应的影响。传统基于 Kirchhoff近似方法无法满足 EUV 光刻仿真的对高精度的要求，严格电磁场（EMF）方法如时域有限差分法（FDTD）、波导法（Waveguide）等，其仿真精度高，但其计算效率无法满足全掩模仿真优化要求。

01 研究方法 Methods

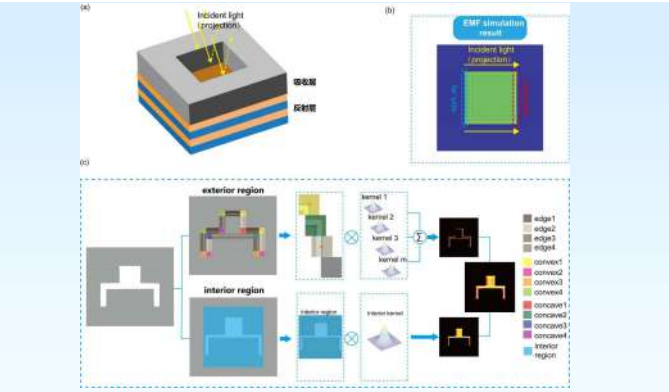

图1.（a）EUV掩模解构及其照明方式。（b） 严格电磁场仿真的近场结果。（c）所提出的掩模DNF计算方法 ，根据掩模边界特征不同将掩模分解成不同的区域。

见图1（a），由于EUV掩模有6°倾斜照明的特点，因此边界上阴影效应具有不对称性。如图1（b）中所示，该图展示了一个方型掩模的严格电磁场近场解，可以看出，该掩模far side与near side光场出现明显不对称现象。假设EUV 掩模在局部区域是空不变系统，见图1（c）中，某一特征区域的掩模衍射近场（Diffraction Near Field, DNF）可以由该区域掩模图形与对应的提前训练的核函数进行卷积调制计算。

02 研究结果 Results

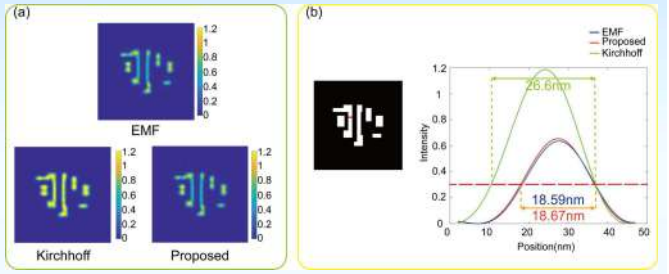

图2.（a）由于不同方法计算得到的掩模空间像结果。（b） 选取该测试掩模红色截线，选取0.3为光刻胶阈值，得到不同方法关键尺寸。

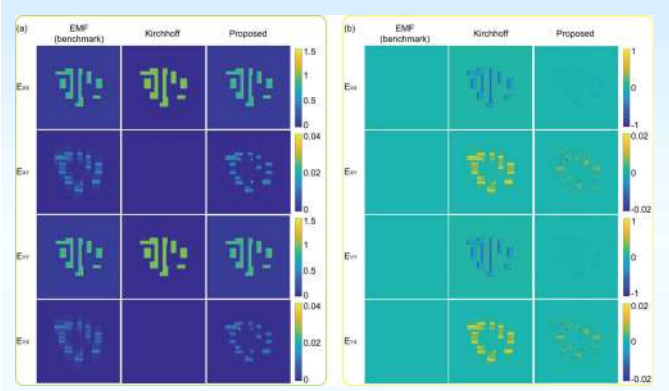

图3.（a）由于不同方法计算得到的掩模近场结果。（b） 以EMF方法为基准， Kirchhoff方法和所提出模型的误差分布。

03 研究结论 Conclusion

该模型在计算速度上相较于严格电磁场仿真提速约45倍，在计算精度上，通过以上结果可以得出如下结论：

- 从空间像结果来看，与严格电磁场仿真的关键尺寸（Critical Dimension, CD）相比，该模型CD的只差0.08nm，而Kirchhoff方法的CD差却高达8nm。
- 从近场计算结果来看，相较于严格电磁场仿真，该方法的RMS低于2%（以E_{XX}为例），而Kirchhoff方法误差高达12.7%。

04 研究前景 Prospects

计算光刻技术在光刻机硬件条件不变的情况下直接决定了光刻分辨率，而准确高效M3D模型的建立是计算光刻技术应用于EUV光刻的前提。该模型为计算光刻中M3D模型的快速精确建模提供了一个极具潜力的解决方案，为全掩模计算光刻技术的产业化应用提供了坚实基础。

姓名：谭锦源　　单位：中国科学院大学前沿交叉科学学院　　邮箱：tanjinyuan24@ime.ac.cn

中国科学院大学
University of Chinese Academy of Sciences
前沿交叉科学学院
School of Advanced Interdisciplinary Sciences

使用垂直双栅 IGZO 薄膜晶体管的高密度三维动态随机存取存储器集成

廖福锡*，朱正勇*，李子涵*
微电子研究所，中国科学院大学，北京，100029

引言 Introduction

随着 AI 与大数据发展，对高容量、低延迟的片上存储需求急剧上升。传统 1T1C DRAM 受电容缩放限制，难以实现 BEOL 三维集成。IGZO TFT 具备低温制备与低漏电优势，使基于其的 2T0C DRAM 成为潜在方案，但现有结构仍存在面积大与读出不可靠的问题。本研究提出自对准单步（SASS）工艺的垂直双栅 IGZO 2T0C 单元，实现 4F² 高密度、可靠读写及>350–500 s 的保持时间，并展示多比特存储能力。

01 研究方法 Methods

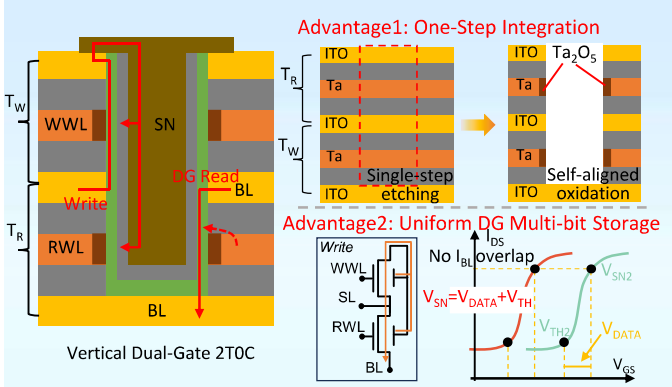

•提出一种垂直双栅极（DG）2T0C DRAM单元。
•采用创新的SASS工艺，单步自对准集成读/写晶体管，消除光刻对准误差。
•实现4F²高密度和高可靠性BEOL DRAM，解决传统单元的读取不可靠问题。

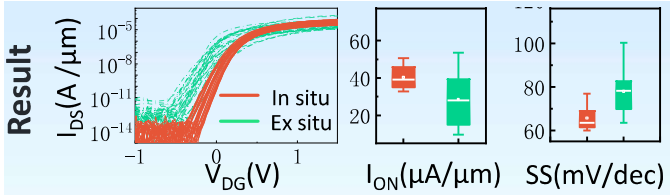

•采用创新的“原位O3自氧化”工艺，显著提升了垂直双栅极IGZO晶体管的性能和一致性。

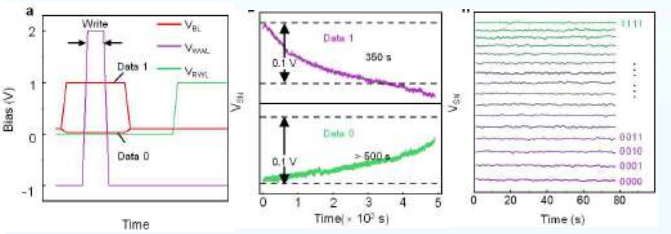

•所制备的4F²双栅极2T0C单元实现了50ns快速写入、超350s长数据保持以及4-bit多比特存储功能。

02 研究结果 Results

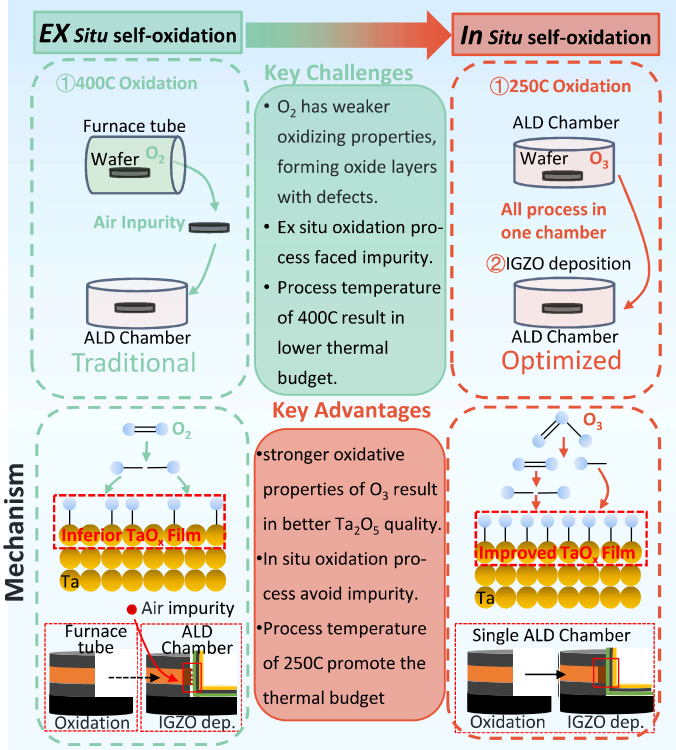

03 研究结论 Conclusion

- 采用创新的自对准单步（SASS）工艺，一次性集成垂直堆叠晶体管，解决了光刻对准难题并简化了流程
- 开发了250°C低温“原位O3自氧化”工艺，在同一ALD腔室中制备高k栅介质，有效避免了界面污染
- 该工艺使晶体管获得了优异且高度一致的电学性能（SS=63mV/dec，I_{ON}=50.3 μA/μm）和高热稳定性
- 最终的4F² DRAM单元实现了50ns快速写入、超470s长数据保持以及4-bit（16态）多比特存储功能

04 研究前景 Prospects

本研究的垂直DG 2T0C DRAM及SASS工艺，凭借250°C低温优势，完美兼容BEOL集成，可堆叠于AI芯片上方，解决“内存墙”。其4F²超小单元与4-bit多比特存储能力奠定了高密度基础。未来，该垂直结构的可堆叠性将支持多层3D集成，实现密度指数级增长，为AI和高性能计算提供超高带宽、低延迟的片上存储方案。

姓名：李子涵　　单位：微电子所　　邮箱：lizihan23@mails.ucas.ac.cn

中国科学院大学
University of Chinese Academy of Sciences

前沿交叉科学学院
School of Advanced Interdisciplinary Sciences

面向半导体超声的声-电混合异构发射芯片设计与超声医学成像调控应用研究

团队成员：林雨澄，靳通，闫晨方，陈宏扬，乔一，邵嘉琳，陈梦娇，史孜豪，赵子杰，高航

单位：中国科学院前沿交叉科学学院 && 中国科学院微电子研究所

邮箱：linyucheng23@mails.ucas.ac.cn / gaohang@ime.ac.cn

中国科学院大学2025年研究生学术论坛前沿交叉科学分论坛

引言 Introduction

医学超声成像作为现代诊疗核心手段，其非侵入式特性在疾病诊断与神经调控领域具有不可替代性。超声介导的经颅神经刺激（TUS）凭借毫米级空间分辨率与颅骨穿透能力，成为脑机接口的前沿技术。然而，现有可穿戴超声贴片受限于高驱动电压、低集成度等瓶颈，难以实现长时程精准调控。

本研究聚焦压电式微机械超声换能器（PMUT）与CMOS工艺的异构集成，突破声-电协同设计、分辨率-能效约束及算法-硬件映射三大技术难题。旨在1）开发高集成度、低功耗的可穿戴超声传感系统；2）实现多频精准调控，提升神经刺激精度和成像深度；3）算法-硬件协同，动态负载自适应调优与阵列声串扰解决； 4）临床转化应用，超声的零辐射非侵入性加速神经调控转化落地。

01 研究方法 Methods

A.协同声-电全链条架构：多阶高压脉冲发射电路

- 构建器件-电场-声场多物理场耦合模型：PMUT等效模型
- 研究PMUT+CMOS带宽拓展特性：多阶脉冲，频率幅度可调面向动态负载的自适应能效调优方法，满足不同穿透深度的超声成像需求。
- 完成通道级的成像/触发的初步验证

B.小阵列集成自适应研究：小型PMUT+CMOS发射电路阵列

- CMOS驱动模式 vs. 多频PMUT阵列转换效率
- 探索阵列中不同器件之间声串扰与声场空间分辨率
- 完成小阵列的成像/触发的验证

C.小大阵列集成应用研究：多通道脑激发神经刺激调控应用

- 器件与CMOS集成域下多频响应的波束成形算法
- 在声学域实现可编程的结构化声场
- 完成大阵列的成像/触发的系列实验验证

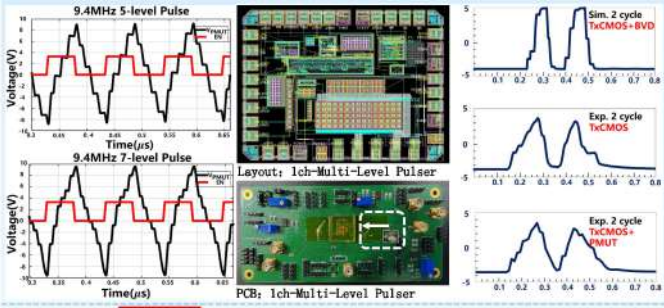

Literature	This work	[20]	[21]	[22]	[23]	[24]	[14]
Year	2025	2024	2023	2020	2014	2021	2020
Transducer(PMUT)	1D Array	1D Array	1D Array	2D Array	2D Array	2D Array	1 Element
Pulse Frequency	3~5MHz	3MHz	1MHz~10MHz	3MHz	217kHz	5MHz	3MHz
Polarity	Bipolar	Unipolar	Unipolar	Unipolar	Unipolar	Unipolar	Unipolar
Technology	0.18μm BCD	HV CMOS	0.18μm BCD-SOI	HV CMOS	HV CMOS	Standard CMOS	HV CMOS
Pulse level	2～5	2	3	2	2	2	2
Amplitude	10Vpp	32Vpp	60Vpp	32Vpp	32Vpp	13.2Vpp	32Vpp
Imaging validation	Human 15mm-depth brachial artery imaging & blood pressure monitoring	Experimental wire phantom imaging	NA	Experimental grating phantom imaging	Experimental wire phantom imaging	Experimental wire phantom imaging	Experimental pulse-echo test
Pulse cycle number	2	4	NA	4	30	3	4
note:	HV CMOS is not BCD. The voltage between Gate and Source can be high.						

- 大带宽的PMUT+CMOS测试系统，在15mm深度处清晰地展示了动脉壁追踪，揭示了一条直径为5mm的血管，在五个心动周期中上、下壁运动的最小分辨率为19μm。

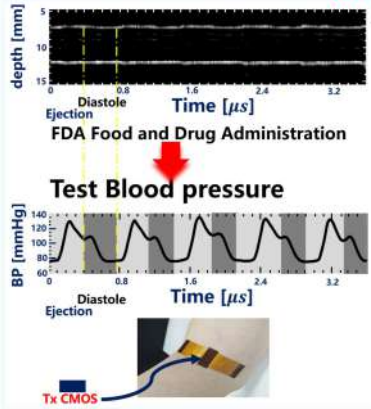

- **研究结论 Conclusion**
  - 发射芯片+PMUT器件脉冲回波测试，高带宽70%。
    1) 提升成像分辨率
    2) 兼顾穿透深度分辨率
    3) 优化信噪比（SNR）
    4) 增强时间分辨率
  - 使用多阶梯脉冲波相比于方波的优势。
    1) 频谱分布，钟形分布
    2) 时域脉冲宽度短
    3) 电磁干扰杂散频率少
    4) 电压渐变，冲击小
    5) 频带匹配谐振频率

02 研究结果 Results

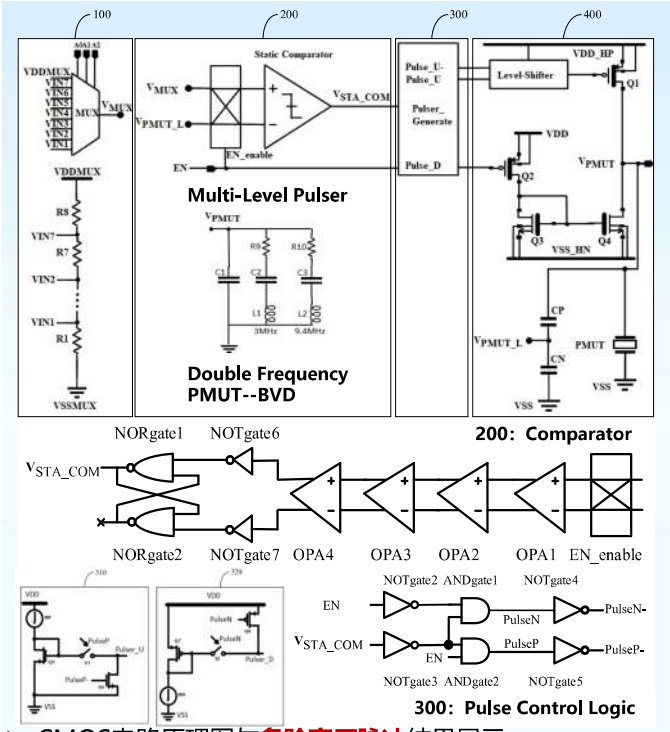

- CMOS电路原理图与多阶高压脉冲结果展示。
  - 仿真结果图与芯片实测图。
  - 在PMUT负载下保持稳定，证实了发射电路的稳健性。

03 研究前景 Prospects

- **可穿戴长程监测：**PMUT与CMOS异构集成突破高驱动电压瓶颈，推动低功耗微型化阵列贴片，实现实时长程神经调控与功能成像，满足床旁监测需求。
- **多频精准调控：**PMUT多频特性结合波束成型算法，生成结构化声场，提升神经刺激空间精准度与成像深度，赋能脑机接口与神经康复。
- **算法-硬件协同：**声-电异构芯片设计优化动态负载能效，多阶脉冲电路降低旁瓣干扰，解决阵列系统声串扰与功耗矛盾，提升分辨率与能量效率。
- **临床转化应用：**零辐射非侵入特性推动长期神经功能评估，通过多层级实验验证，加速超声神经调控向脑疾病诊疗及数字健康产品的转化落地。

中国科学院大学
University of Chinese Academy of Sciences

前沿交叉科学学院
School of Advanced Interdisciplinary Sciences

Efficient and Stable Organic Solar Cells Achieved by Synergistic Optimization of Extended End-Capped Groups and Fluorinated Quinoxaline Central Cores in Nonfullerene Acceptors

Chi Zhang, Yanan Shi, Jing Tao, Jianqi Zhang, Hao Zhang, Dingding Qiu, Caixuan Wang, Chenyang Tian, Zhixiang Wei,* and Kun Lu*
National Center for Nanoscience and Technology, Beijing, China, 100190

引言 Introduction

Molecular stacking behavior exerts a significant influence on the blend film morphology of organic solar cells (OSCs), further affecting device performance and stability. Modulation of the molecular structure, such as central unit and end-group, can profoundly impact this process. Herein, four quinoxaline (Qx)-fused-core-based non-fullerene acceptors (NFAs), Qx-N4F and Qx-*o/m/p*-N4F are synthesized combining π-extended end-groups and optimized central units. The isomeric fluorinated central units lead to changes in the local dipole moments and electrostatic potential distribution, which influences the molecular stacking pattern and photoelectronic properties of NFAs. Consequently, binary and ternary devices based on PM6:Qx-*p*-N4F achieve superior power conversion efficiencies (PCE) of up to 18.75% and 19.48%, respectively. Grazing-incidence wide-angle X-ray scattering (GIWAXS) characterization reveals Qx-*p*-N4F's stronger crystallinity, aggregation, and donor–acceptor interactions, which can separately enhance short-circuit current density (J_{SC}) and fill factor (FF) through higher phase purity and tighter molecular stacking based on maintaining more donor–acceptor interfaces. Furthermore, PM6:Qx-*p*-N4F-based devices demonstrate exceptional thermal stability, retaining 93.2% of the initial PCE value after 3000 h of heating due to the best morphological stability with the most stable stacking structure. These results underscore the significance of synergistic optimization of NFAs through conjugation expansion and halogenation substitution for obtaining efficient and stable OSCs.

01 研究方法 Methods

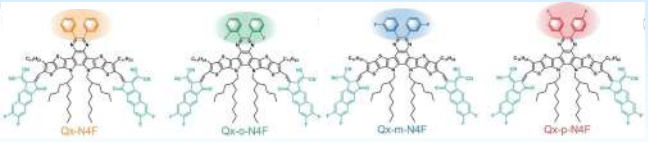

We designed and synthesized four novel quinoxaline-based NFAs, Qx-N4F, Qx-*o*-N4F, Qx-*m*-N4F, and Qx-*p*-N4F, bearing various isomeric (*ortho*-, *meta*-, and *para*-) fluorinated central units and fluorinated naphthalene-based end groups. We used UV–vis absorption spectra for their optical properties, cyclic voltammetry measurements for the experimental energy levels, density functional theory calculations for the molecular structure properties, and conventional device structure device fabrication for exploring the mechanisms behind the device performance differences.

02 研究结果 Results

Density functional theory calculations (B3LYP/6-31G(d,p)) were performed to understand the molecular structure properties of these NFAs. The correlations between the energy levels by DFT calculations for the four acceptors are similar to the CV test results. From the optimized geometries, the dihedral angles between the fluorinated phenyl ring and the Qx core are 42.71°, 50.30°, 42.46°, and 42.19° for Qx-N4F, Qx-*o*-N4F, Qx-*m*-N4F, and Qx-*p*-N4F, respectively. The smaller dihedral angles for *meta*-, *para*-substituted, and unsubstituted acceptors suggest enhanced molecular planarity and therefore may lead to stronger interaction between the molecules. For Qx-N4F, Qx-*o*-N4F, and Qx-*m*-N4F, the vector of the local dipole moment of the central donor unit is along the direction from the Qx core to the fluorinated phenyl ring, implying that the 2-(3-oxo-2,3-dihydro-1*H*-cyclopenta[*b*]naphthalen-1-ylidene)malononitrile (NINCN) end group is more likely to interact with the fluorinated phenyl rings. Qx-*m*-N4F's central donor unit has the smallest local dipole moment, meaning that the interaction between the NINCN end group and the fluorinated phenyl ring is negligible. Hence, the NINCN group of the *meta*-substituted acceptor prefers to interact with the electron-donating thiophene (TT) unit. Intriguingly, a local dipole moment in the opposite direction has been observed in Qx-*p*-N4F, indicating a higher likelihood of interaction between the NINCN terminal group and the central Qx moiety. Both the maximum (37.55 kcal mol^{-1}) and minimum (−34.18 kcal mol^{-1}) values of the electrostatic potential of Qx-*p*-N4F are higher than those of the remaining three molecules with similar structures, suggesting its higher overall electrostatic potential, which shows that it produces stronger molecular interaction when blended with polymer donors (e.g., PM6) bearing more negative ESP distribution.

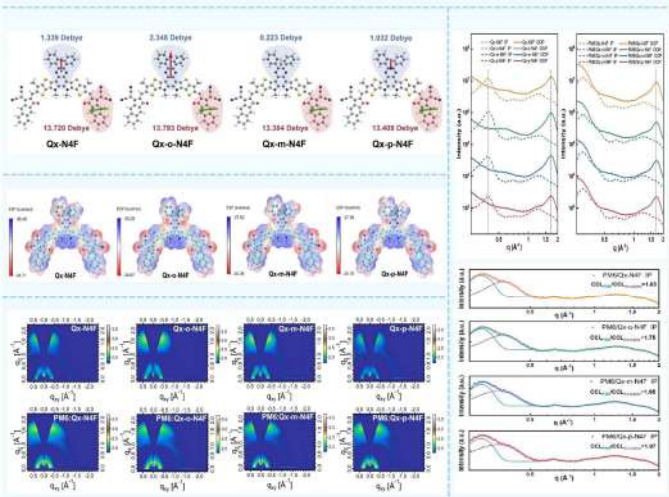

03 研究结论 Conclusion

In summary, a series of quinoxaline-based NFAs have been logically designed and synthesized by employing halogenation modification and conjugation expansion strategies at the central unit and end groups to investigate the impact of different halogenation substitution positions and π-conjugation on the physicochemical properties, molecular stacking behaviors, and even device performance of OSCs. The *para*-substituted acceptors exhibit advantageous molecular stacking than the unsubstituted, *ortho*-, and *meta*-substituted acceptors, owing to a local dipole moment in the opposite direction and higher electrostatic potential. And *para*-substituted acceptors also form a more suitable phase separation due to more efficient regulation of molecular interactions in blend films, as corroborated by AFM and GIWAXS. As a result, Qx-*p*-N4F exhibited optimal molecular interaction, and blend film morphology, therefore achieving the highest PCE of 17.81%, significantly superior to that of Qx-N4F, Qx-*o*-N4F, and Qx-*m*-N4F (15.03%, 15.65%, and 16.58%, respectively). This value could be further improved to 18.75% and 19.48%, respectively, after fine optimization of interfacial engineering and the introduction of a third component in the active layer. And it is one of the leading values for single-junction OSCs. In addition, Qx-*p*-N4F-based binary devices showed favorable thermal stability, maintaining 93.2% of their initial efficiency after 2981 h of heating at 85 degrees Celsius. This system also achieves a device extrapolation lifetime of 12 450 h for long-term use.

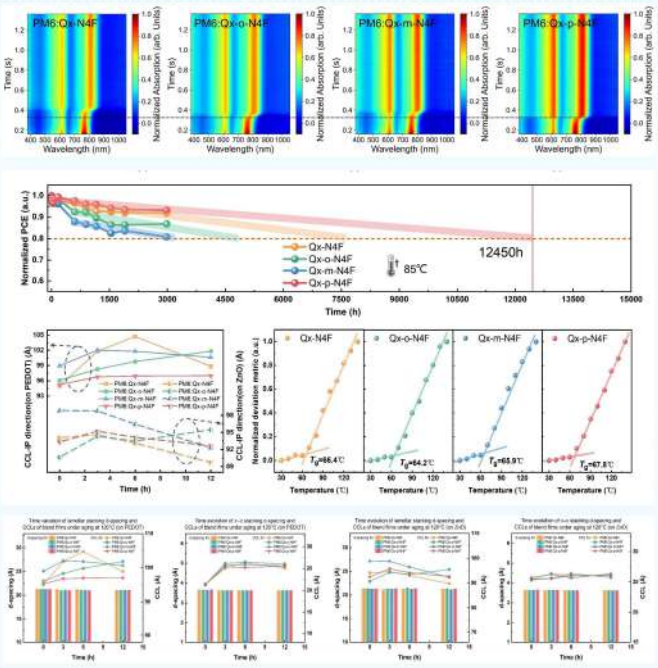

04 研究前景 Prospects

Our work revealed the synergetic effect of systematic halogenation and conjugation expansion in NFAs and emphasized the method of regulating D/A stacking behavior, building a bridge among molecular structure, molecular interaction, and blended film morphology for efficient and stable OSCs.

姓名：张驰　　单位：国家纳米科学中心　　邮箱：zhangc2022@nanoctr.cn

中国科学院大学
University of Chinese Academy of Sciences

前沿交叉科学学院
School of Advanced Interdisciplinary Sciences

基于掩模热-力耦合效应的高精度套刻误差补偿方法

芮定海, 张利斌, 雷宗谕, 沈浩, 侯新伟, 韦亚一*, 粟雅娟
微电子研究所, 中国科学院大学, 北京, 100029

引言 Introduction

随着先进集成电路制造向更小工艺节点推进，层间套刻误差已成为限制图形对准精度及工艺一致性的关键因素。特别是在近场光刻和纳米压印光刻等新型的非投影式光刻体系中，由于缺乏可调节的投影光学系统，传统光刻技术所依赖镜头畸变校正或低阶模型拟合的补偿方式难以满足高分辨图形对准需求。本研究面向近场光刻体系，提出一种基于掩模像素级热调控与周边机械应力联合作用的套刻误差补偿方法。

01 研究方法 Methods

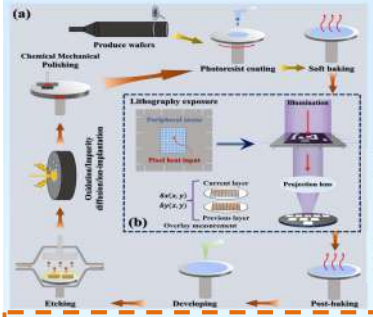

本研究围绕光刻中的场内套刻补偿问题，构建了一种基于掩模热-力耦合调控的系统化方法：①在26 mm*33 mm曝光区域中布设**像素级局部热剂量单元**，用于精确调节掩模局部温度分布；②在掩模边缘配置**分布式机械应力加载点**，以控制由边界受力引起的应变场。

- 在ANSYS与COMSOL**多物理场**平台中建立掩模热-力耦合模型。
- 在弹性理论框架下推导二者的线性叠加关系并仿真验证该关系，确保后续模型可通过线性求解方式获得最优执行参数。
- 引入**五阶高阶多项式模型**对误差场进行分解，从而在数学空间中表示线性、非线性、旋转及更复杂的高阶畸变。
- 通过**统计显著性分析**筛选主要影响项，以在保证精度的前提下，降低模型维度并提升求解稳定性。
- 将掩模执行机构模型与高阶套刻分解K参数耦合，构建补偿模型$k_j = f_j(p_1, p_2, \cdots, p_{m+n})$并可反向求解使场内套刻最小化的最优热-力执行量$p_i$。

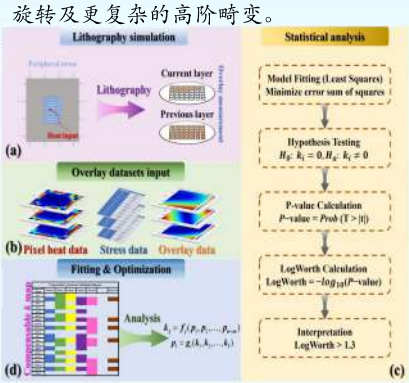

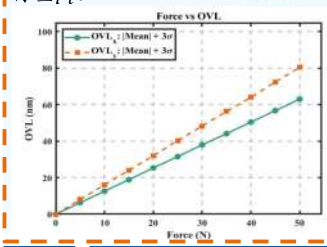

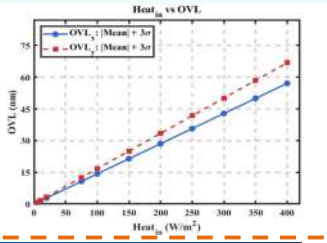

02 研究结果 Results

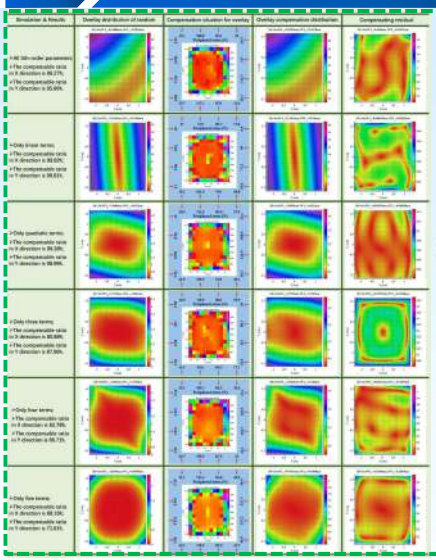

◆ 基于五阶多项式的高阶套刻误差补偿模型能够在多类随机误差分布下实现稳定且高效的修正。该套刻补偿模型可有效地将套刻误差 |mean|+3σ **降低到1nm以下**，符合先进光刻节点的要求。

◆ 线性与二阶误差可基本完全补偿，逐点的套刻误差残差低于0.1nm；三阶与四阶误差的**补偿率超过80%**，残差约0.5nm；五阶误差亦可实现约68%的修正，**残差不足0.4nm**。

◆ 高阶补偿模型对线性与二阶误差均可实现超过97%的修正。对三至五阶误差，四阶补偿效果最佳，残留约6.1%。

◆ 对膨胀效应的**K19,K20,K38,K41,K42**以及收缩效应的部分高阶项仍存在超过20%的残差，表明该模型在特定高阶畸变参数上存在补偿性能边界。

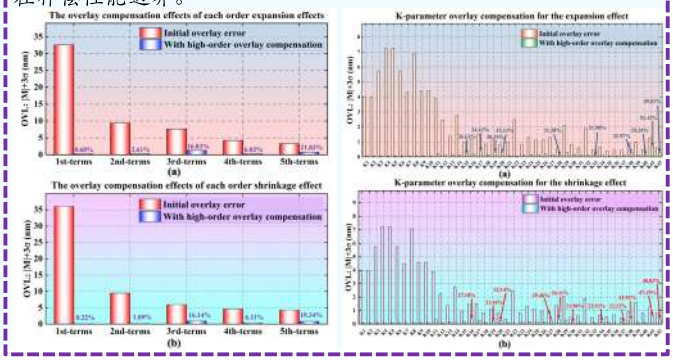

03 研究结论 Conclusion

综上所述，基于五阶多项式的高阶套刻误差修正模型能够在多类误差条件下实现稳定、有效的补偿。有限元验证套刻补偿模型的准确性：**偏差小于0.9%，可补偿至1.5nm，偏差在±0.04nm**。模型在五阶误差中保持可观性能，且在实际工艺中展现出良好适应性与鲁棒性。

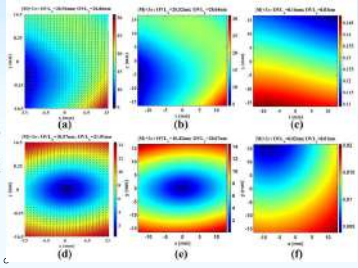

04 研究前景 Prospects

面向3nm以下节点对亚纳米级套刻精度要求，掩模补偿技术将在NIL等新型光刻体系中发挥关键作用，并成为EUV中需考虑的重要协同控制手段。引入**AI驱动的实时补偿框架、跨尺度套刻建模与多物理场耦合调控**，以支撑更先进制程的制造需求。

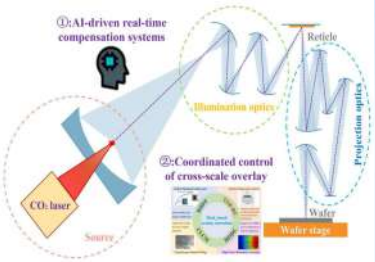

姓名：芮定海　　单位：中国科学院微电子研究所　　邮箱：ruidinghai@ime.ac.cn

中国科学院大学
University of Chinese Academy of Sciences

前沿交叉科学学院
School of Advanced Interdisciplinary Sciences

基于表面势的紧凑模型建立框架：驱动IGZO-DRAM的DTCO

李旭帆，姜文峰，顾宸，赵越，耿玙，杨冠华，汪令飞*，李泠*
中国科学院微电子研究所，中国科学院大学，北京，100029

引言 Introduction

Monolithic 3D (M3D) DRAM has garnered significant attention in response to the increasing industry demand for enhanced DRAM capacity with the rapid advancement of artificial intelligence. Amorphous In-Ga-Zn-O (a-IGZO) has emerged as a promising candidate for 3D DRAM integration due to its excellent uniformity, extremely low leakage current, and inherent compatibility with back-end-of-line (BEOL) processing. However, charge transport mechanisms in a-IGZO are inherently complex owing to its material disorder. Therefore, the development of reliable compact models is crucial to address the challenges of precise performance characterization of transistors (AC or DC) associated with device scaling, structural variations in IGZO-based DRAM.

01 器件制造 Technology

Monolithic 3D (M3D) DRAM has garnered significant attention in response to the increasing industry demand for enhanced DRAM capacity with the rapid advancement of artificial intelligence. Amorphous In-Ga-Zn-O (a-IGZO) has emerged as a promising candidate for 3D DRAM integration due to its excellent uniformity, extremely low leakage current, and inherent compatibility with back-end-of-line (BEOL) processing. However, charge transport mechanisms in a-IGZO are inherently complex owing to its material disorder. Therefore, the development of reliable compact models is crucial to address the challenges of precise performance characterization of transistors (AC or DC) associated with device scaling, structural variations in IGZO-based DRAM.

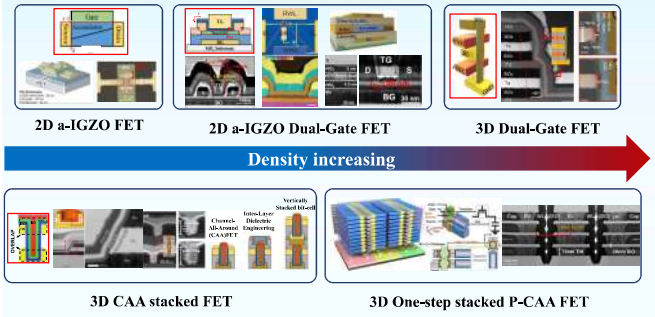

Fig. 1. Continuous density increases in IGZO-DRAM along the two primary pathways: dual-gate and channel-all-around (CAA).

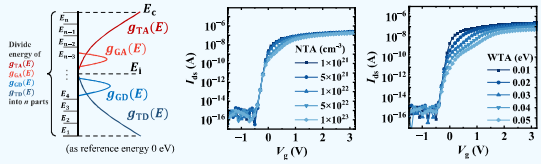

Fig. 2 Transfer curves of IGZO-FET, varying DoS on the electrical characteristics, containing mainly tail acceptor-like trap states and Gaussian acceptor-like trap states

02 协同优化 DTCO

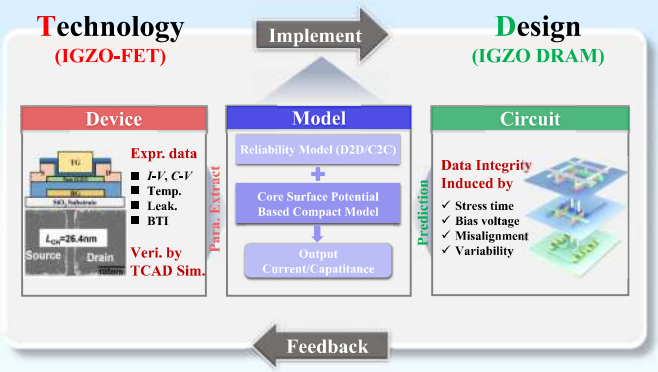

Fig. 3. The DTCO flow utilizing the surface potential-based compact model as a bridge between design and devices

03 紧凑模型 Compact Model

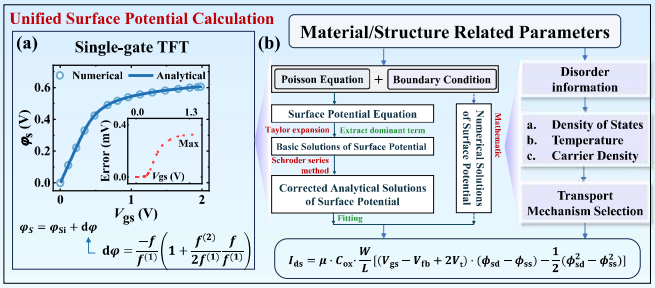

Fig. 4. Good agreement between analytical and numerical results for surface potential with error in the inset. (b) A flow diagram of surface potential-based compact model for unified surface potential calculation.

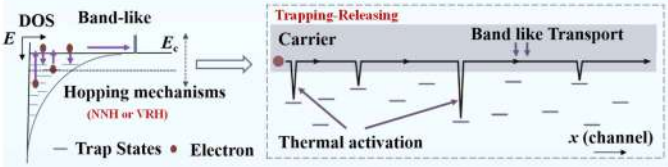

Typical Mobilities*		Symbol	Features
Multiple Trapping-Releasing		μ_{MTR}	Transition from disordered to band-like transport
Percolation theory		μ_{PERC}	Transport distance and energy dependence
Trap-limited transport		μ_{TLC}	Thermally released into the conduction band
Hopping	Variable-range	μ_{VRH}	Hopping to variable-range sites
	Nearest-neighbor	μ_{NNH}	Hopping to nearest neighbor sites
Finite-size Corrected		μ_{FSC}	Dimension-dependence/with scaling factor

*different transport mobilities exhibit typical density and temperature dependence

Fig. 5. Typical transport mobilities utilized in compact model.

04 电路仿真预测 SPICE

Considering the statistical effect on the sub-threshold region of DRAM cells, the statistical distribution of retention time can be obtained. Moreover, the variation will be aggregated in a larger timescale. Thus, for future circuit design, a reliability-aware DTCO enabled by compact model is quite significant. By incorporating the BTI or other stress-induced degradation, the lifetime prediction can be also achieved.

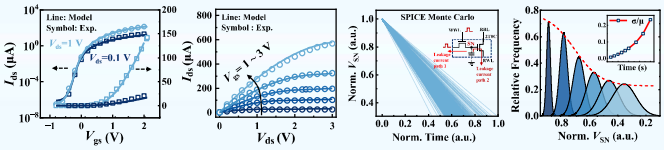

Fig. 6. Circuit simulation of 2T0C eDRAM to predict the retention time with Monte Carlo method and extract bit distribution and the Gaussian fitting of bit distribution.

姓名：李旭帆　　单位：中国科学院微电子研究所　　邮箱：lixfuan@ime.ac.cn

中国科学院大学
University of Chinese Academy of Sciences

前沿交叉科学学院
School of Advanced Interdisciplinary Sciences

Direct Implementation of High-Fidelity Three-Qubit Gates for Superconducting Processor with Tunable Couplers

Hao-tian Liu[1,2], Bing-Jie Chen[1,2], Kai Xu[1,2,3*], Heng Fan[1,2,3†], et al

[1] Institute of Physics, Chinese Academy of Sciences, Beijing 100190, China
[2] School of Physical Sciences, University of Chinese Academy of Sciences, Beijing, 100049, China
[3] Beijing Academy of Quantum Information Sciences, 100193 Beijing, China
kaixu@iphy.ac.cn, hfan@iphy.ac.cn

Physical Review Letters 135, 050602 (2025)

引言 Introduction

Three-qubit gates can be constructed using combinations of single-qubit and two-qubit gates, making their independent realization unnecessary. However, direct implementation of three-qubit gates reduces the depth of quantum circuits, streamlines quantum programming, and facilitates efficient circuit optimization, thereby enhancing overall performance in quantum computation.

01 研究方法 Methods

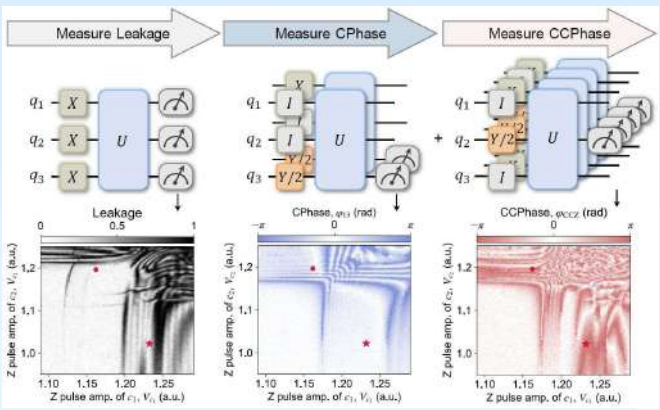

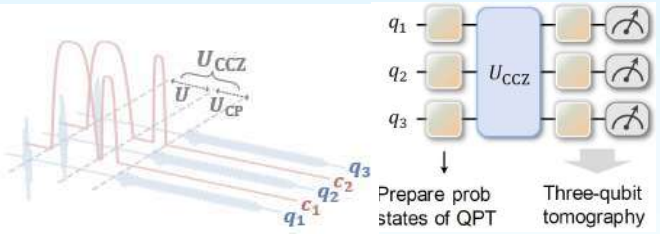

Measure Leakage: We prepare |111⟩ by applying X gates to the three qubits and measure the population of |111⟩ after U.

Measure CCPhase: We initialize three qubits in six special states, and then measure all conditional phases, i.e., $\varphi_{12} = \varphi_{|1+0\rangle} - \varphi_{|0+0\rangle}$, $\varphi_{23} = \varphi_{|0+1\rangle} - \varphi_{|0+0\rangle}$, $\varphi_{13} = \varphi_{|1\,0+\rangle} - \varphi_{|0\,0+\rangle}$, $\varphi_{123} = \varphi_{|1+1\rangle} - \varphi_{|0+0\rangle}$, the CCPhase of CCZ is given by $\varphi_{CCZ} = \varphi_{123} - \varphi_{13} - \varphi_{12} - \varphi_{23}$.

Compensate phases: φ_{12} and φ_{23} can be compensated by applying corresponding CPhase gates, and we apply virtual Z gates to compensate for the accumulations of single-qubit dynamic.

Measure Fidelity: We apply the quantum process tomography (QPT) to get χ-matrix fidelity.

02 研究结果 Results

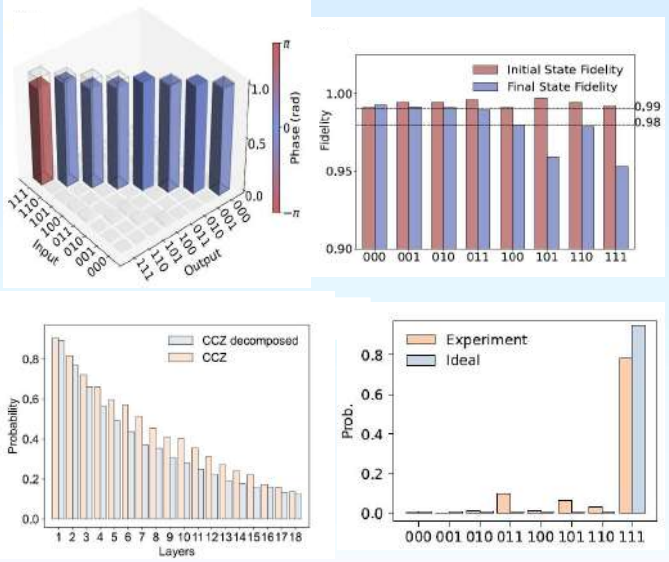

03 研究结论 Conclusion

- **Direct implementation of high-fidelity three-qubit gates.** This method is scalable and requires minimal connectivity between qubits and couplers, offering significant advantages in terms of gate length and leakage compared to the decomposed CCZ gate schemes.
- **Successful application to three-qubit Grover search algorithm.** Our experimental results closely align with theoretical predictions, i.e., the probability amplitude of the target state is significantly higher than that of other states after two Grover iterations.

04 研究前景 Prospects

Our work is expected to substantially contribute to the advancement of complex quantum algorithms and the realization of scalable quantum systems by providing a reliable and high-fidelity multi-qubit gate operation.

姓名：刘皓天　　单位：中国科学院物理研究所　　邮箱：liuht@iphy.ac.cn

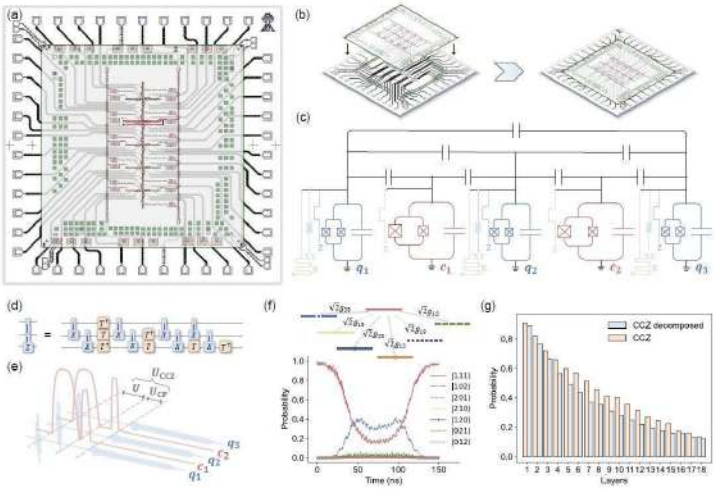

FIG. 1. (a) The flip-chip quantum processor with 21 superconducting qubits arranged in a 1D chain with multiple legs. Every two qubits are equipped with a coupler in between. (b) Schematic of flip-chip technique. (c) Circuit diagram of the implemented superconducting circuits framed by the red dotted line in (a), consisting of three qubits (q_1, q_2, q_3) and two couplers (c_1, c_2). The qubits have the independent XY and Z controls and readout resonators, while the couplers have only Z controls. (d) Quantum circuit of the CCZ gate decomposed into a series of single-qubit gates and CX (CNOT) gates. (e) Pulse sequence of the direct CCZ gate for superconducting qubits with tunable couplers. (f) Energy level diagram and time-dependent population transfer in the three-excitation manifold. (g) Comparison of multi-layer leakage between the direct CCZ gate and its decomposed implementation.

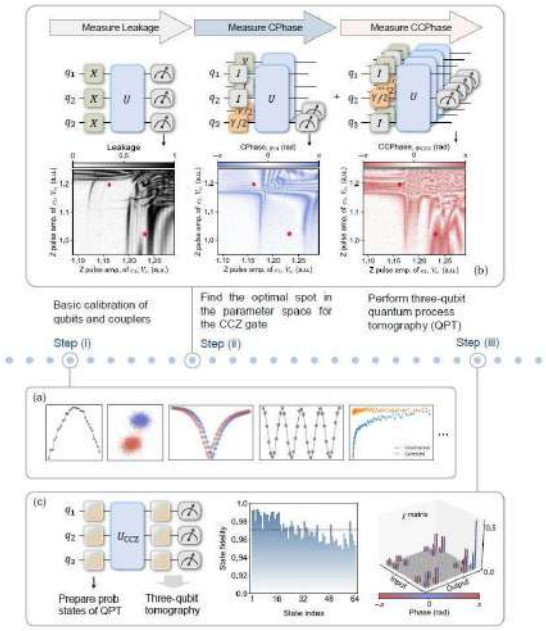

FIG. 2. Experimental measurements and calibrations for CCZ gate. (a) Basic calibration of qubits and couplers. (b) Calibration of the Z pulse amplitudes of couplers for the CCZ gate. The optimal operating points, where $\varphi_{CCZ} = \pm\pi$ while both leakage and φ_{13} approach zero, are marked by a dot and a star. Given that the working point marked by the star has a smaller $|\varphi_{13}|$, we select it as the preferred operating point. The circuits to measure leakage, CPhase, and CCPhase are illustrated at the middle. (c) Experimental data of quantum process tomography (QPT) of the CCZ gate. From left to right are the QPT circuit, the fidelities of 64 prob states, and χ-matrix. The average final state fidelity is 97.06% and the process fidelity is 93.54%.

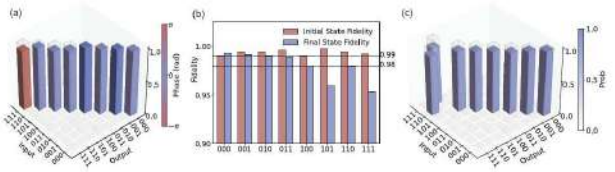

FIG. 3. Experimental results for the CCZ and Toffoli gates. (a) The truth table of CCZ gate. Theoretical probabilities are represented by transparent cylinders, while experimental probabilities and conditional phases are depicted by the height and color of solid cylinders, respectively. The average fidelity of the truth table is 96.52%. (b) The state fidelity of CCZ gate. The average final state fidelity is 97.94%. (c) The truth table of Toffoli gate. Theoretical probabilities appear as hollow cylinders, with experimental probabilities indicated by colorbar.

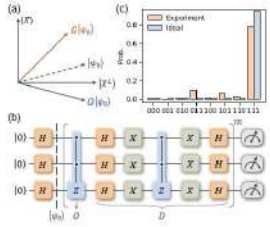

FIG. 4. Demonstration of three-qubit Grover search algorithm. (a) Schematic diagram of Grover algorithm principle. (b) Quantum circuit of three-qubit Grover search algorithm. (c) Probability data after two Grover operations.

中国科学院大学
University of Chinese Academy of Sciences

前沿交叉科学学院
School of Advanced Interdisciplinary Sciences

On-surface sulfur-to-metal single-atom editing of surface-bound thiourea into adatom-bound carbene SAMs

Xiao Han (韩笑) [a], Arne Nalop [b], Alex-Cristian Tomut [c], Nikos L Doltsinis [c], Frank Glorius [b], Jindong Ren (任金东) [a*]

[a] National Center for Nanoscience and Technology, Beijing 100190, P.R. China.

[b] University of Münster, Organisch-Chemisches Institut, 48149 Münster, Germany.

[c] University of Münster, Institut für Festkörpertheorie and Center for Multiscale Theory and Computation, 48149 Münster, Germany.

Corresponding authors: nikos.doltsinis@uni-muenster.de glorius@uni-muenster.de renjd@nanoctr.cn

引言 Introduction

N-Heterocyclic carbene (NHC) self-assembled monolayers (SAMs) are emerging as robust and versatile surface ligands, yet their direct on-surface construction with atomic precision remains elusive. Here, we report a reagent-free, thermally driven on-surface strategy for single-atom editing, providing an alternative to convert heteroatom-anchored SAM into functional NHC layer. N-Heterocyclic thiourea (NHT) undergoes a S-to-metal adatom exchange, yielding adatom-bound NHC on coinage metal surfaces. Using low-temperature scanning tunneling microscopy (LT-STM), X-ray photoelectron spectroscopy (XPS), and density functional theory (DFT), we identify two distinct classes of SAMs: (i) NHT-SAM, in which sulfur coordinates to the metal surface and (ii) NHC-SAM, characterized by M–C σ-bonds between the carbene center and a surface adatom. Upright NHT undergoes a clean SAM-to-SAM conversion, achieving covalent single-atom editing within an intact monolayer. DFT calculations show this transformation is energetically favorable and highly tunable by substrates and N-substituents, establishing a general framework for atom-precise molecular editing at surfaces.

01 研究方法 Methods

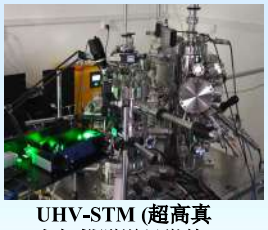

UHV-STM (超高真空扫描隧道显微镜)

SR-XPS (同步辐射X射线光电子能谱)

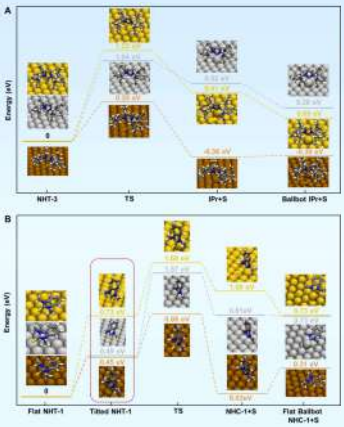

DFT (密度泛函理论计算)

02 研究结果 Results

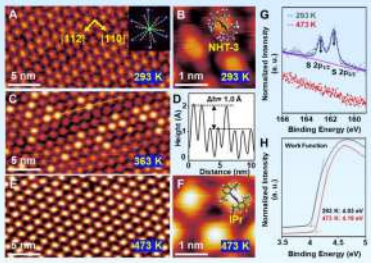

Fig 1. (A) Large-scale STM image showing the self-assembled monolayer of NHT-3 molecules on Au(111) at 293 K. **(B)** High-resolution STM image highlighting a single NHT-3 molecule. **(C)** STM topography after annealing the sample to 363 K revealing two types of monomeric features with distinct apparent heights, corresponding to pristine NHT-3 and its transformation product, IPr. **(D)** Line profile along the yellow trace in (C). **(E)** Large-scale view displays uniform contrast for all monomers after annealing to 473 K. **(F)** Zoom-in STM image of (E), confirming that all surface species are upright IPr molecules, indicative of complete conversion. **(G)** S 2p XPS spectra of NHT-3 covered Au(111) surfaces before (293 K) and after annealing at 473 K. **(H)** Work function measurements derived from XPS before (A) and after (E) annealing, showing a 0.16 eV increase upon transformation. This process exemplifies bottom-up SAM-to-SAM conversion via C=S bond scission and adatom coordination—an atomically precise, covalent-level single-atom edit.

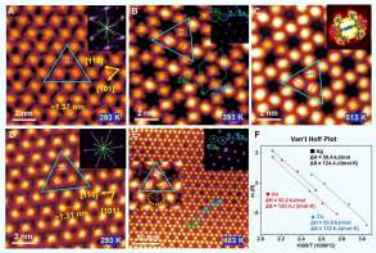

Fig 2. (A) STM image of the self-assembled NHT-3 monolayer on Ag(111), forming a close-packed structure composed of equilateral trimer units with uniform monomer orientations. *Inset*: FFT image showing a well-ordered hexagonal packing; yellow dashed lines indicate the orientation of the Ag(111) lattice. **(B)** After annealing to 393 K, mixed NHT–IPr domains appear, forming a distorted Kagome-type pattern. Inset: FFT image of the Kagome arrangement. **(C)** STM image of the fully converted IPr monolayer at 513 K, where all NHT-3 molecules are converted to IPr on Ag(111). *Inset*: Simulated STM image of a single NHT-3 molecule on Ag(111), with the molecular long axis represented by a dashed line. **(D)** STM image of NHT-3 molecules on Cu(111), forming trimer-based assemblies analogous to those on Ag(111). *Inset*: FFT image confirming the ordered molecular arrangement. **(E)** STM image following thermal annealing on Cu(111), showing the formation of IPr molecules along with residual sulfur clusters, a signature of C=S bond cleavage. *Inset*: Zoom-in view highlighting the morphology of the IPr species and sulfur clusters. **(F)** Van't Hoff plot showing different entropy and enthalpy on the tested substrates.

03 研究结论 Conclusion

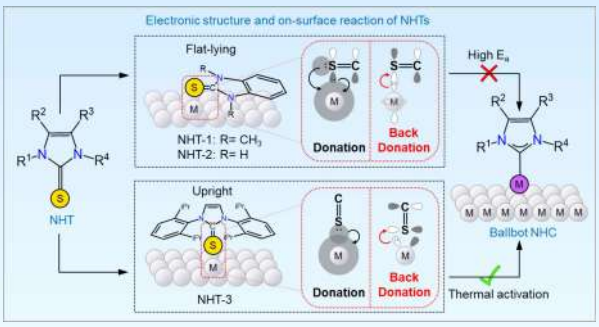

Fig 3. Schematic comparison of interfacial bonding between flat-lying (NHT-1/2) and upright (NHT-3) adsorption configurations on metal surface.

In summary, we have established a new paradigm for atomic-level precision in surface chemistry by demonstrating single-atom editing within a SAM. Through this platform, we elucidate the controlled adsorption geometry, self-assembled molecular patterning, orbital-level metal–ligand charge exchange, and thermally induced reactivity of NHT ligands at well-defined metal interfaces. Our combined STM, XPS, and DFT studies reveal that the surface configuration—flat-lying or upright—is primarily governed by the steric and electronic nature of the nitrogen substituents. This geometry not only dictates the assembly and bonding motifs but also plays a central role in enabling distinct on-surface chemical transformations. Flat-lying NHTs form stable networks stabilized by S–metal σ-donation and C=S π-back-donation, while upright NHT undergoes thermally driven C=S bond cleavage to form covalently anchored NHC, with the transformation barrier modulated by both the molecular structure and the metal substrate. Beyond a simple molecular transformation, this work highlights how spatially confined, single-atom-level editing can reorganize one ordered monolayer into another. Our DFT reaction pathway calculations unveil that the scission of the C=S bond, as well as the subsequent ballbot formation, proceeds with the lowest activation barrier in the case of NHT-3, in stark contrast to the kinetically and thermodynamically disfavored reactions for NHT-1 and NHT-2. This selective single-atom editing within a preassembled monolayer not only preserves the mesoscale periodicity of the SAM but also introduces chemically distinct anchor motifs at specific molecular sites. In contrast to traditional routes to adatom-bound NHCs that rely on CO_2-protected precursors and limit the incorporation of electron-withdrawing substituents, our NHT-based approach leverages thermally activated on-surface conversion, providing a versatile route to functional NHC architectures while avoiding harsh reagents or complex ion-exchange processes. By enabling substrate-dependent, atomically precise reconfiguration of molecular monolayers, this work provides opportunities for surface-confined catalysis, adaptive interface design, and programmable nanoscale fabrication.

References

1. Pan Y, Ren J, et al., *Chem Soc Rev.*, **2025**, *54*, 4626–4650.
2. Ren J, Glorius F, et al., *JACS.*, **2024**, *146*, 7288-7294.
3. Ren J, Glorius F, et al., *JACS.*, **2024**, *146*, 32558-32566.
4. Ren J, Glorius F, et al., *Nat. Chem.*, **2023**, *15*, 1737-1744.

04 研究前景 Prospects

- Elucidation of the controlled adsorption geometry, self-assembled molecular patterning, orbital-level metal–ligand charge exchange, and thermally induced reactivity of NHT ligands at well-defined metal interfaces.
- NHT-based approach leverages thermally activated on-surface conversion, providing a versatile route to functional NHC architectures while avoiding harsh reagents or complex ion-exchange processes.

姓名：韩笑　　单位：国家纳米科学中心　　邮箱：hanx2023@nanoctr.cn

中国科学院大学
University of Chinese Academy of Sciences

前沿交叉科学学院
School of Advanced Interdisciplinary Sciences

Effective Regulation of Li_2MnO_3-like Single-Component in High-nickel Li-rich Layered Oxides by Trace Sb Doping for Remarkable Performance Improvement

Dongdong Mao[1,2], Zhengwei Fan[1,2], Weiguo Chu[1,2]**
1National Center for Nanoscience and Technology, Beijing 100190, China
2University of Chinese Academy of Sciences, Beijing 100049, China

引言 Introduction

High-energy density and cycling stability are essential for high-performance LIB cathodes. Here, Sb is introduced as a dopant for single-component regulation (SCR) to modify HNLOs via a facile expanded-graphite template–sacrificed method. Owing to the much lower incorporation energy of Sb in the Li_2MnO_3-like C2/m phase than in the $LiNiO_2$-like R-3m phase—verified by structural characterizations and theoretical calculations—trace Sb selectively stabilizes the Li_2MnO_3-like framework. This targeted modification suppresses irreversible oxygen release by lowering unhybridized O-2p states and enhances electronic conductivity by narrowing the band gap. Consequently, SCR-engineered HNLOs deliver excellent rate performance and long-term durability, retaining 85.5% capacity with only a 0.87 mV per-cycle voltage drop after 300 cycles at 1C. The SCR behavior and underlying mechanisms were further elucidated using advanced operando techniques.

01 研究方法 Methods

Material preparation: Expanded graphite (EG, 50 mesh; Qing Dao Teng Sheng Da Tan Su JiXie, China) templated synthesis of $Li_{1.2}Ni_{0.32}Mn_{0.48}O_2$ (LNMO) and Sb-doped $Li_{1.2}Ni_{0.32}Mn_{0.47}Sb_{0.01}O_2$ (Sb-LNMO). Stoichiometric Li, Ni, Mn nitrates, with/without antimony acetate, were dissolved in deionized water, impregnated into EG, dried, calcined at 450 ° C for 120 min, then 900 ° C for 720 min in air (5 ° C min^{-1}).

Structural characterization: Morphology/microstructure by SEM (NanoSEM430, USA) and TEM-EDS (Tecnai F20, Thermo Fisher). Crystal structure and cycling evolution by XRD (Rigaku D/MAX-2500; Cu Kα, 200 mA, 45 kV). Elemental contents by ICP-AES (IRIS Intrepid II). Raman (Renishaw inVia-Reflex, 785 nm) and XPS (ESCALab 250Xi) probed bonding and valence. DFT calculations: VASP (GGA-PBE, PAW) with Monkhorst–Pack k-meshes, 450 eV cutoff, full relaxation; energy convergence 1×10^{-5} eV $f.u.^{-1}$; residual forces <0.02 eV $Å^{-1}$.

Electrochemistry: CR2025 coin cells with cathodes of 80 wt% active materials, 10 wt% acetylene black, 10 wt% PVDF cast on Al, vacuum-dried 80 ° C 12 h, punched. Cells (Ar glovebox): Li metal counter, Celgard 2340 separator, 1 M $LiPF_6$ in EC:EMC:DMC (1:1:1) + 5 vol% VC. Tests on a NEWARE system (Neware, China) at 2.0–4.6 V (RT); CV and EIS (100 kHz–1 mHz, CHI660D).

02 研究结果 Results

Figure 1 proves single-component regulation (SCR): Rietveld refinements and DFT show Sb preferentially enters the Li_2MnO_3-like *C2/m* phase (lower formation energy), expanding its lattice and increasing its fraction (≈48.7%→57.7%) while leaving *R-3m* nearly unchanged. TEM/EDS reveals uniform Sb without surface coating; the larger interlayer spacing (≈4.76 Å) lengthens Li–O and shortens Mn–O in *C2/m*, facilitating Li^+ transport and stabilizing lattice oxygen.

Figure 2 links structure to performance: Sb-LNMO shows lower polarization, higher initial capacity (236 vs 214 mAh g^{-1}, 0.1 C) and superior rate capability (212/192/151/128 vs 174/158/117/91 mAh g^{-1} at 0.5/1/5/10 C). It sustains 85.5% capacity retention with only 0.87 mV $cycle^{-1}$ voltage decay after 300 cycles (1 C). Electronic conductivity roughly doubles (~1.09×10^{-4} vs 5.49×10^{-5} S cm^{-1}), Rct decreases, GITT shows faster Li^+ diffusion, and in-situ XRD reveals smaller *c*-axis excursions—evidence of mitigated strain. Innovation: phase-selective Sb doping isolates the dominant *C2/m* physics, jointly enhancing oxygen stability and charge transport to stabilize voltage and energy density.

In Figure 3, operando Raman displays stronger, persistent peroxo O–O bands at ~4.5 V and a steadier DMC signal, indicating more reversible anionic O-redox and suppressed O_2 release; DSC of charged electrodes shifts the main exotherm from 236.4 ° C to 289.0 ° C with reduced heat, confirming improved oxygen stability.

Figure 1 proves single-component regulation (SCR): Rietveld refinements and DFT show Sb preferentially enters the Li_2MnO_3-like *C2/m* phase (lower formation energy), expanding its lattice and increasing its fraction (≈48.7%→57.7%) while leaving *R-3m* nearly unchanged. TEM/EDS reveals uniform Sb without surface coating; the larger interlayer spacing (≈4.76 Å) lengthens Li–O and shortens Mn–O in *C2/m*, facilitating Li^+ transport and stabilizing lattice oxygen.

03 研究结论 Conclusion

Targeting the Li_2MnO_3-like *C2/m* sublattice with Sb enables single-component regulation of high-Ni Li-rich cathodes. DFT predicts lower Sb incorporation energy in *C2/m*, and experiments confirm selective occupation. This lowers the O-2p band, narrows the bandgap, suppresses oxygen release, and accelerates Li^+ transport. The result is higher capacity and rate, 85.5% retention, and only 0.87 mV per-cycle voltage fade after 300 cycles at 1 C.

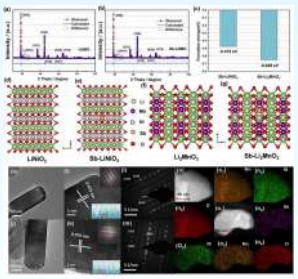

Figure 1

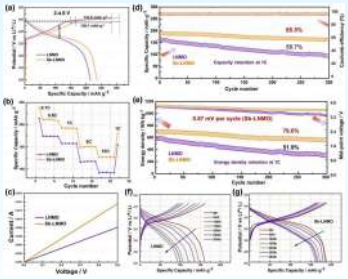

Figure 2

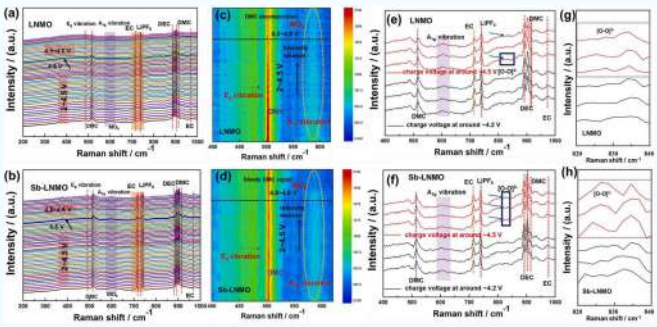

Figure 3

04 研究前景 Prospects

Beyond performance, SCR offers a clean design rule: use phase-selective dopants to stabilize anionic redox and restrain TM migration, instead of co-doping both phases. The concept is transferable to other Li-rich chemistries and dopants. Future work will tune dopant level/distribution, pair SCR with surface or gradient architectures, validate at high loading and upper cut-off, and scale synthesis toward practical full-cell tests.

姓名：范钲威　　单位：国家纳米科学中心　　邮箱：fanzw2020@nanoctr.cn

中国科学院大学
University of Chinese Academy of Sciences

前沿交叉科学学院
School of Advanced Interdisciplinary Sciences

基于拉索控制合成手性碳纳米环中的二次谐波效应

于琦
国家纳米科学中心，中国科学院大学，北京，海淀，100080

引言 Introduction

Chiral conjugated nanorings with D_n symmetry exhibit remarkable circularly polarized luminescence (CPL) properties due to their unique columnar helical conjugated systems. However, their synthesis faces challenges such as the vast number of atropisomers and the cumbersome procedures required for separation, purification, and chiral resolution, which severely hinder the development of this field. This study proposes a chiral lasso-guided synthesis strategy: by introducing alkyl chain tethers with planar chirality into the fused-ring building blocks of the nanorings, the energy differences among the various atropisomers are significantly enhanced. This promotes the formation of the thermodynamically most stable D_n-symmetric isomer during synthesis, substantially improving selectivity. Using this approach, the chiral nanoring D_3-(*P*)-NR5 and its enantiomer were efficiently prepared. All molecules demonstrated excellent and stable CPL performance, with the highest luminescence dissymmetry factor reaching 0.016. Furthermore, single crystals of the chiral nanorings exhibited second-harmonic generation circular dichroism (SHG-CD), showing distinct differential responses to left- and right-handed circularly polarized light.

01 研究方法 Methods

The synthetic route for the chiral nanorings is illustrated in the figure. For D_3-(*P*)-NR5, starting from the previously reported planar chiral cyclophane (S_p)-1, the fluorene-terminated amide (S_p)-2 was first synthesized via an amidation reaction. This was followed by a Pd-catalyzed intramolecular C–H activation/coupling cyclization to afford the nine-membered fused-ring lactam (S_p)-3. Subsequent bromination with NBS and reaction with hexa-n-butyldistannane yielded the terminal tributyltin-substituted intermediate (S_p)-5. Equimolar amounts of (S_p)-5 were then reacted with Pt(COD)Cl_2 to form platinum-macrocyclic complex intermediates. Finally, the chiral nanoring D3-(P)-NR5 was obtained via a PPh_3-promoted reductive elimination reaction, yielding 40% (starting from (S_p)-5). Furthermore, employing the planar chiral cyclophane (R_p)-1 as the starting material, the enantiomer of chiral nanoring D_3-(*P*)-NR5, namely D_3-(*M*)-NR5, was successfully synthesized.

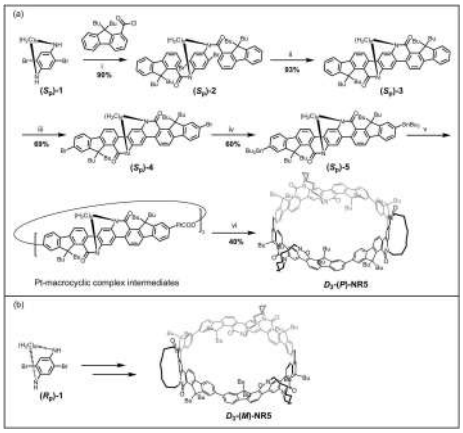

02 研究结果 Results

Single-crystal structures:

The single-crystal structures of D_3-(*P*)-NR5 and D_3-(*M*)-NR5 are shown in the figure. Crystallographic data confirm that all chiral nanorings adopt a single configuration without the presence of other atropisomers, and their cyclic backbones consistently exhibit characteristics of D_3 symmetry. Interestingly, although the chiral nanorings D_3-(*P*)-NR5 and D_3-(*M*)-NR5 are expected to display mirror-symmetric crystal structures, slight differences in their crystal and packing structures are observed due to variations in crystal growth conditions.

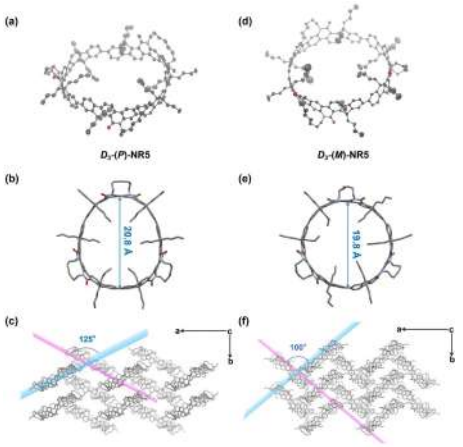

Optical Properties:

The chiral nanorings exhibit mirror-imaged CD and CPL spectra with strong CPL signals. Consistent with the CD signals near the band edge, all *P*-type nanorings display negative Cotton effects, while all *M*-type nanorings show positive Cotton effects. The chiral nanorings possess large luminescence dissymmetry factors (glum), with D_3-(*P*)-NR5 and D_3-(*M*)-NR5 achieving a high $|g_{lum}|$ value of 0.016. This places them among the rare pure organic molecules exhibiting such large intrinsic circularly polarized luminescence asymmetry factors.

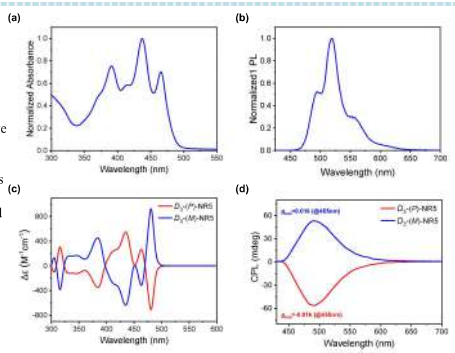

03 研究结果 Results

SHG-CD Properties:

Rod-like crystals of D_3-(*P*)-NR5 were deposited onto a fused silica substrate by slow evaporation of its crystal suspension. When excited with a 1064 nm femtosecond pulsed laser beam perpendicular to the substrate, a sharp peak at 530 nm was detected in reflection mode, indicating the second-harmonic generation (SHG) activity of the D_3-(*P*)-NR5 crystals. Furthermore, the second-harmonic intensity at 530 nm exhibited a distinct power dependence, further confirming the occurrence of a two-photon process (Figure a, b). To determine the relationship between the SHG intensity and crystal orientation, polarization-dependent SHG measurements were performed on the D_3-(*P*)-NR5crystal. By varying the polarization direction of the excitation light, two mutually perpendicular figure-eight-shaped SHG patterns were observed, confirming the breaking of twofold rotational symmetry (Figure c).

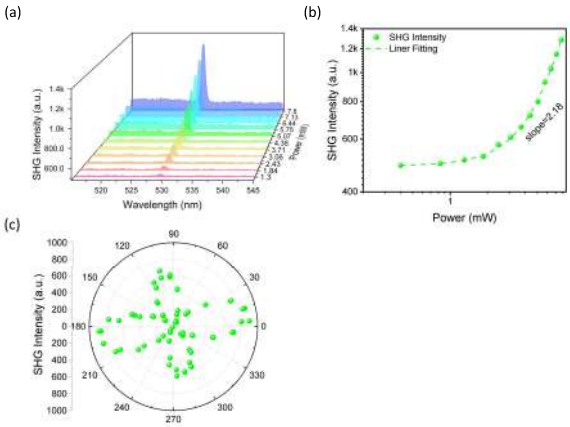

Similarly, SHG-CD properties were investigated by depositing D_3-(*P*)-NR5 and D_3-(*M*)-NR5 crystals onto fused silica substrates via slow evaporation of their respective crystal suspensions. Under excitation with a 1064 nm femtosecond pulsed laser, the second-harmonic generation intensity from the D_3-(*P*)-NR5 and D_3-(*M*)-NR5 crystals varied with the rotation of the λ/4 waveplate (Figure e, f). Notably, the D_3-(*P*)-NR5 crystal exhibited a stronger SHG signal under left-handed circularly polarized (CP) light excitation, whereas the D_3-(*M*)-NR5 crystal showed a stronger signal under right-handed CP light excitation, thus confirming the SHG-CD effect in the chiral nanoring single crystals. The calculated $g_{SHG\text{-}CD}$ values for D_3-(*P*)-NR5 and D_3-(*M*)-NR5 crystals were 0.52 and −0.5, respectively, ranking among the highest reported for organic crystals.

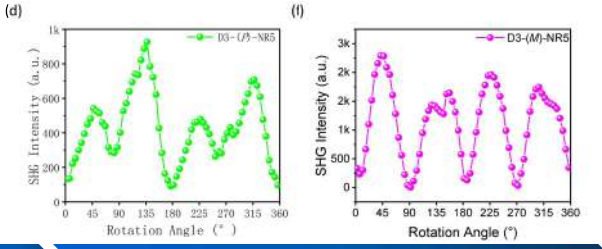

03 研究结论 Conclusion

Based on the developed chiral lasso-guided strategy, we have achieved highly selective synthesis of chiral conjugated nanorings with D_3 symmetry. All synthesized chiral nanoring molecules exhibit excellent circularly polarized luminescence (CPL) properties, with a maximum luminescence dissymmetry factor (g_{lum}) of 0.016 and a high fluorescence quantum yield of up to 70%, demonstrating their significant potential as CPL-emitting materials. Furthermore, single crystals of these chiral nanorings possess second-harmonic generation circular dichroism (SHG-CD) activity, exhibiting a $g_{SHG\text{-}CD}$ value of up to 0.52, which ranks among the highest values reported for organic crystals.

姓名：于琦　　单位：国家纳米科学中心　　邮箱：yuq2023@nanoctr.cn

中国科学院大学
University of Chinese Academy of Sciences

前沿交叉科学学院
School of Advanced Interdisciplinary Sciences

自组装超顺磁纳米粒子单层膜中的无序超均匀性

贾复麟，巩建晓*
国家纳米科学中心，中国科学院大学，北京，100190

引言 Introduction

纳米粒子的自组装技术能够制备具有多组分、多功能的材料，这些材料在众多潜在应用领域中可能包含特定类型的无序结构。无序超均匀体系是一种特殊物质状态，其在长波长范围内具有类似完美晶体的零密度涨落特性，同时却不具备长程有序性。尽管对具有显著特征的无序超均匀体系的理论研究已持续二十年，但在纳米尺度实现大规模实验制备仍鲜有报道。本研究提出了一种可靠高效的制备方法：通过在液-气界面自组装超顺磁性纳米粒子来制备无序超均匀单层膜。一方面，外磁场诱导产生的强长程偶极-偶极排斥作用使体系难以压缩，从而促进超均匀态的形成；另一方面，二元纳米粒子混合物打破了长程有序性，实现了统计各向同性。我们还研究了具有最佳数量分数比的大面积无序超均匀单层膜的力学性能。总体而言，无序超均匀薄膜虽然质地较软，但其断裂强度均高于对应的非超均匀体系。

01 研究方法 Methods

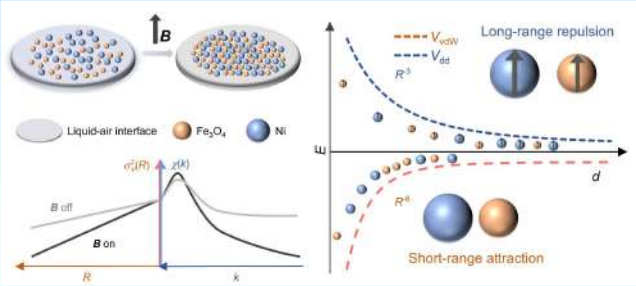

$$\sigma_V^2(\boldsymbol{R}) \sim \begin{cases} R^{d-1}, & \alpha > 1 \\ R^{d-1}\ln R, & \alpha = 1 \\ R^{d-\alpha}, & 0 < \alpha < 1 \end{cases} \quad (R \to \infty) \qquad \lim_{\|\boldsymbol{k}\|\to 0} \chi(\boldsymbol{k}) = 0, \quad H \equiv \frac{\chi(k_{min})}{\chi(k_{peak})}$$

二元超顺磁纳米颗粒在长程磁偶极相互作用下实现无序超均匀组装

02 研究结果 Results

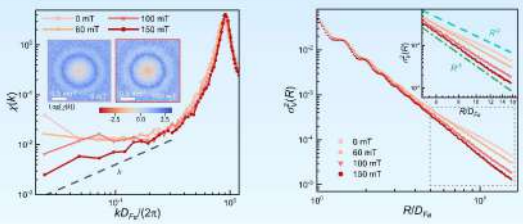

随着磁场强度的增大，体系的超均匀性增强

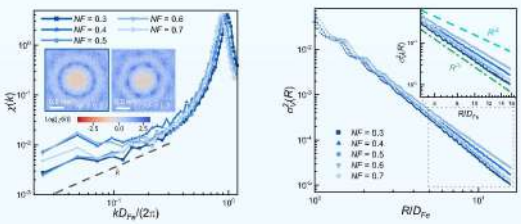

NF= 0.5是体系无序超均匀的最优值

03 研究结论 Conclusion

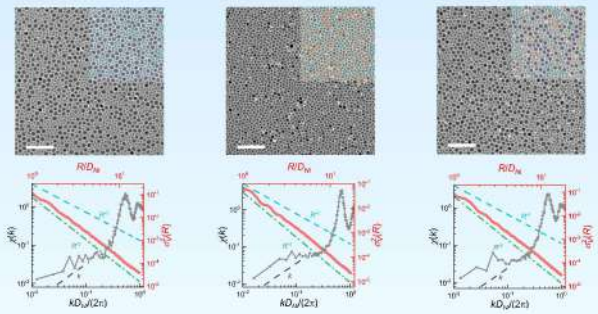

外加磁场驱动无序超均匀结构形成的策略行之有效

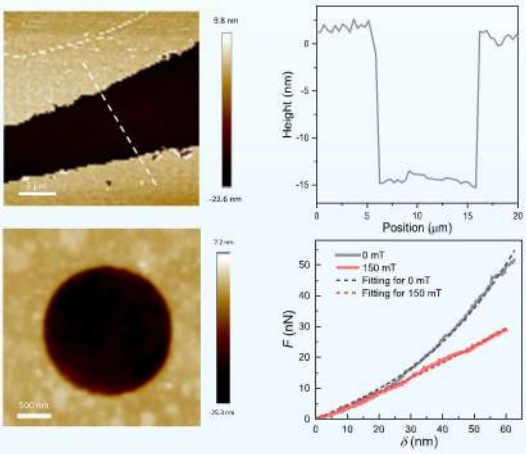

力曲线拟合结果表面超均匀薄膜模量更低，断裂强度更高

04 研究前景 Prospects

通过调节磁场强度和粒子相对浓度，可以实现二维组装体超均匀性的最优化

对于不同的组装单元组合，体系均表现出超均匀性，这说明我们的策略具有普适性

长波涨落被抑制，局部应力集中的区域减少，力学性能提升

姓名：贾复麟　　单位：国家纳米科学中心　　邮箱：jiafl2021@nanoctr.cn

中国科学院大学
University of Chinese Academy of Sciences

前沿交叉科学学院
School of Advanced Interdisciplinary Sciences

基于苯并二呋喃的低成本酯基聚合物用于有机太阳能电池

丛培卿，唐爱玲，邓丹，魏志祥
（国家纳米科学中心，中国科学院纳米系统与多级次制造重点实验室，100190，北京）

引言 Introduction

有机太阳能电池（OSC）因其质轻柔性，可大面积印刷等独特优势而备受关注。近年来，随着以Y系列为代表的非富勒烯受体（NFA）的飞速发展，目前高效单结有机太阳能电池的光电转换效率（PCE）已经超过20%。但由于昂贵的活性层材料，导致距离真正意义上的商业化还有着一定差距。基于此，我们将苯并二呋喃（BDF)与酯基修饰的噻吩[3,2-b]并噻吩（TTC）共聚，开发了一种新型的低成本羧酸聚合物TTC-F-BDF，与先前基于苯并二噻吩（BDT）的聚合物TTC-F对比，可以有效优化分子聚集、调控分子堆积，从而优化共混膜形貌，增强电荷传输和收集过程，最终得到接近17%的PCE。

01 研究内容 Results

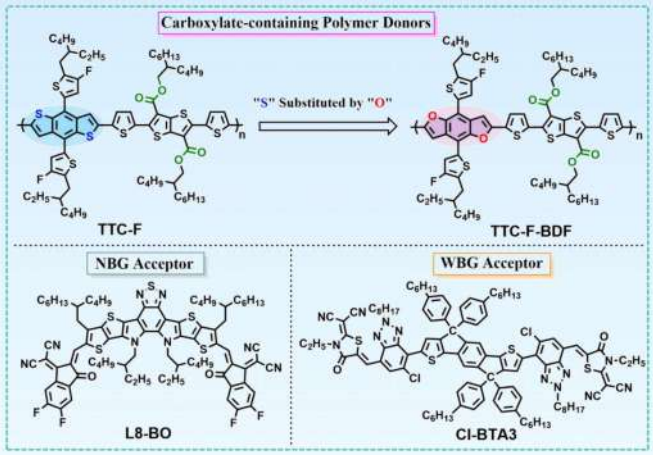

图1 聚合物给体和宽窄带隙小分子受体的化学式结构

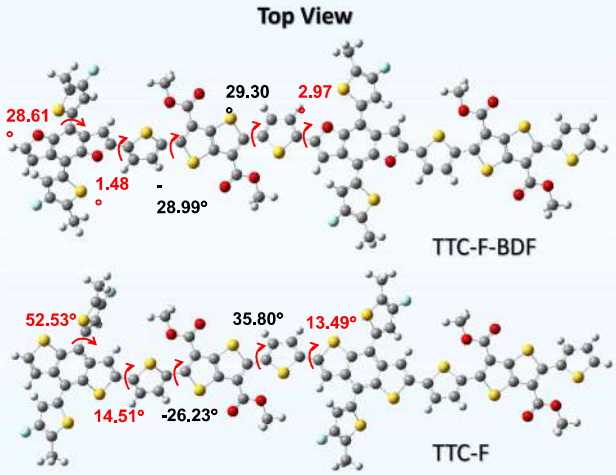

图2 TTC-F-BDF和TTC-F聚合物给体的DFT计算

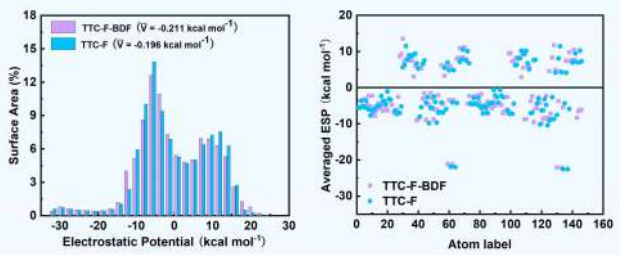

图3 计算的TTC-F-BDF和TTC-F的静电势面积分布直方图及平均ESP值

➢ 光伏性能及载流子动力学

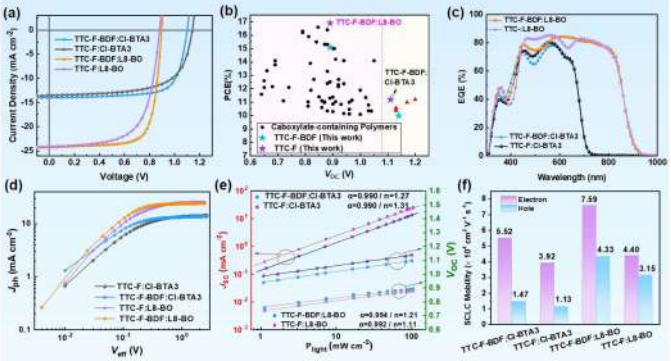

- 基于TTC-F-BDF的器件表现出比TTC-F更高的性能和光电响应
- TTC-F-BDF的体系具有更为显著的分子复合特性以及更高而平衡的迁移率

➢ 能量损失分析

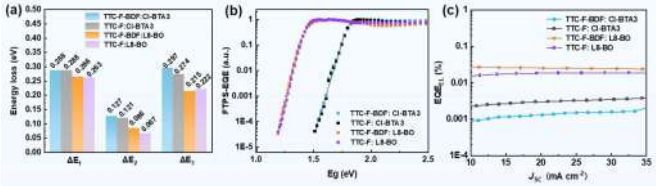

- TTC-F-BDF:L8-BO的器件表现出最高电致发光效率和最低的非辐射复合损失

➢ 形貌分析

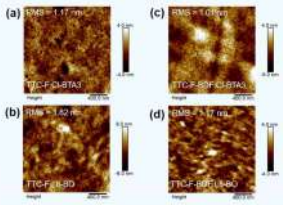

- 四种体系的AFM高度图

02 研究结论 Conclusion

将低成本的BDF单元与2T-TTC单元共聚，开发出了一种宽带隙给体聚合物TTC-F-BDF。与基于BDT单元的TTC-F相比，BDF对于主链上D单元的取代使TTC-F-BDF聚合物更强的聚集性，更紧密的π-π堆积，更有序的分子间堆积。因此，基于TTC-F-BDF的有机太阳能电池器件具有更为优化的成膜形态，从而改善了FF。TTC-F-BDF:L8-BO二元器件获得了16.9%的最高效率，证明了BDF单元的引入对聚合物聚集、体异质结形态和光伏性能的显著影响。

姓名：丛培卿　　单位：国家纳米科学中心　　邮箱：congpq2022nanoctr.cn

中国科学院大学
University of Chinese Academy of Sciences

前沿交叉科学学院
School of Advanced Interdisciplinary Sciences

A Novel Chiral L-Lys Carbon Dot as an "On-Off-On" Fluorescent Sensor for the Detection of Mercury (II) and Glutathione with Efficient Determination

Hao Liang, Min Li, Zunli Mo

(Key Laboratory of Eco-Functional Polymer Materials of the Ministry of Education, College of Chemistry and Chemical Engineering, Northwest Normal University, Gansu, Lanzhou, 730070)

Introduction

Mercury ions (Hg^{2+}), as one of the toxic heavy metal ions widely present in daily life, pose a serious threat to ecological safety and human health. Therefore, effective monitoring of Hg^{2+} is essential for safeguarding public environmental well-being. Glutathione is extensively distributed in both animal and plant organisms, participating in various cellular biochemical activities. It is closely associated with liver damage, cardiac issues, cancer, and other metabolic disorders. So, designing a highly selective and sensitive method for assay of glutathione also presents a worthy challenge. Carbon dots (CDs) is a new class of fluorescent carbon nanomaterials. Since being discovered in 2004, they have been used in a broad range of applications for optical sensing, drug delivery, and bioimaging because of their outstanding optical properties, great biocompatibility and low toxicity. Its unique fluorescence properties offer the possibility to construct an efficient Hg^{2+} and GSH fluorescence sensing platform.

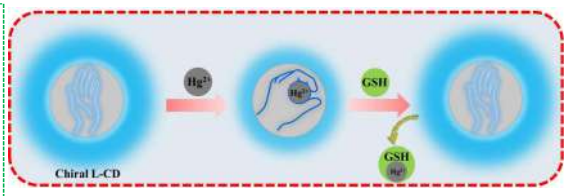

01 Methods

Based on the literature, CA was chosen as the classical carbon source and cheap and easily dispersed L-Lys as the chiral source, a one-step hydrothermal method was used for the simple preparation of chiral L-CD. As illustrated in **Scheme 1**, firstly, 0.585 g L-Lys was dissolved in 10 mL distilled water and sonicated homogenously. Then 5 mL 0.8 mol/L CA solution was added slowly with stirring and dropwise at room temperature, and the pH was adjusted to 6 by joining NaOH solution when the reactions were mixed well. Lastly, the above solution was transferred to a 50 mL Teflon-sealed stainless autoclave and reacted at 140 ℃ for 2 h. The brown solution obtained was filtered through a 0.22 μm aqueous membrane and continuously dialyzed using a 500 Da dialysis bag for 48 h with water changes every 12 h in the interim, then gotten by freeze-drying. Additional ratios of CDs were treated by the same way.

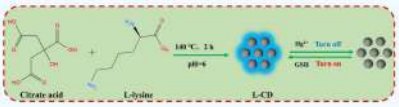

Scheme 1. Diagram illustrating the synthesis of L-CD.

02 Results

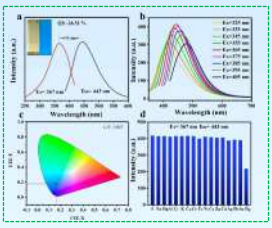

Fig. 1 Fluorescence excitation and emission spectra of L-CD (a) (The inset displays visual photographs of the sample in daylight and under UV light.). (b) Fluorescence spectra of L-CD aqueous solution with various excitation wavelength from 325 to 405 nm. (c) CIE 1931 Colorimetric Map. (d) Fluorescent intensity of L-CD aqueous solution after addition of different metal ions.

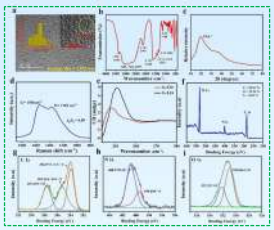

Fig. 2 (a) TEM images of L-CD (inset: HR-TEM image and size distribution histogram); (b) FT-IR spectra, (c) XRD pattern, Raman spectra (d) and CD spectra (e) of the material; (f) XPS survey of L-CD; XPS high-resolution spectra of C 1s (g), (h) N 1s and (i) O 1s.

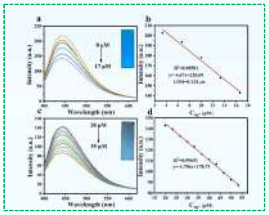

Fig. 3 Changes in fluorescence intensity of L-CD aqueous solution after addition of different volumes Hg^{2+} in the concentration scale from 0 μmol/L to 55 μmol/L (a) (c). Linear correlation between Hg^{2+} concentration and fluorescence intensity (b) (d) (The inset image presents the color of L-CD aqueous solution with and without Hg^{2+} under the UV light).

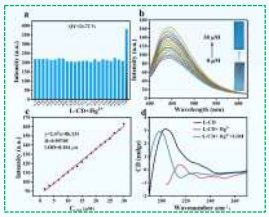

Fig. 4 (a) Fluorescence recovery of L-CD+Hg^{2+} after joining various amino acids and GSH solutions (the inset graph displays a picture of the L-CD+Hg^{2+} solution under UV light after the GSH was added). (b) Changes in fluorescence intensity of L-CD aqueous solution after addition of different volumes GSH in the concentration scale from 0 μmol/L to 30 μmol/L. (c) Linear correlation between GSH concentration and fluorescence intensity (d).

Table 1. Detection of the spiked Hg^{2+} in the Yellow River water and Tap water samples.

Samples	Added (μM)	Founded (μM)	Recovery (%)	RSD (%, n = 3)
Yellow River water	0	Not Found	Not Found	Not Found
	10	10.22	102.20	1.81
	20	21.33	106.65	2.67
Tap Water	0	Not Found	Not Found	Not Found
	10	10.38	103.80	0.91
	20	21.39	106.95	1.20

Table 2. Detection of the spiked GSH in human serum samples.

Samples	Added (μM)	Founded (μM)	Recovery (%)	RSD (%, n = 3)
Human serum	0	Not Found	Not Found	Not Found
	10	10.49	104.90	1.38
	20	21.35	106.75	1.41

03 Conclusion

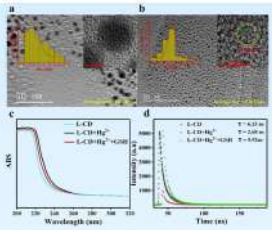

Fig. 5 TEM images of L-CD+Hg^{2+} (a) and L-CD+Hg^{2+}+GSH (b). UV-visible spectra and fluorescence decay curves of L-CD, L-CD+ Hg^{2+} and L-CD+ Hg^{2+}+GSH.

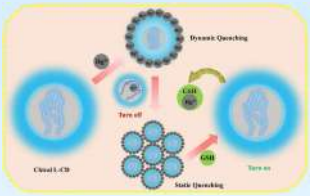

Fig. 6 Possible mechanisms of L-CD response to Hg^{2+} and GSH.

In the present study, an "on-off-on" fluorescent sensor, L-CD, was synthesized in a short time by using a low-temperature one-step hydrothermal reaction for the efficient and selective detection of Hg^{2+} and GSH. Its Ex=367 nm, Em=443 nm, and the short Stokes shift (76 nm) indicates its high energy conversion efficiency and photothermal stability. Possibly because of the small range of particle size distributions, L-CD exhibited a high absolute QY (26.51 %) and a pronounced excitation dependence. Stability tests showed that L-CD maintained almost constant fluorescence emission at higher ionic strengths (1.0 mol/L), and the luminescence intensity remained at more than 98% of the original intensity even after 24 h irradiation by UV lamp, as well as the intensity difference was less than 2 % in the low temperature region. Due to the effect of hydrogen bonding between surface functional units, the fluorescence intense of L-CD fluctuates within a narrow scope in various pH solutions. In addition, multiple characterizations indicate that L-CD exhibits a regular spherical distribution with an average particle size of 1.85 nm, with abundant hydrophilic groups such as hydroxyl, carboxyl, and amide groups, consisting of regular sp2 hybridized carbon centers and sp3 hybridized amorphous carbon surfaces. CD spectra demonstrate that its chiral character may be transferred from L-Lys to L-CD via a chiral genetic strategy, and result in weakened CD signaling and positional shifts due to the destruction of the chiral structure by hydrothermal processes. Further studies revealed that L-CD has rapid reactivity and extraordinary selectivity to Hg^{2+} and GSH, and the chiral official groups on its surface may act as luminescent moieties interacting with Hg^{2+} and GSH, leading to fluorescence turn-off and turn-on. Titration experiments found that Hg^{2+} exhibited a unique two-stage response in the 0-17 μM and 20-55 μM, with the LOD as low as 0.124 μM. GSH was able to restore the luminescence of the L-CD+Hg^{2+} system rapidly and stably in the 0-30 μM, LOD=0.104 μM, which was superior to other reports in the literature. Mechanistic analysis suggests that the fluorescent bursting mechanism of Hg^{2+} against L-CD not only involve static quench, but also may include dynamical quench. Initially Hg^{2+} undergoes energy transfer or charge collision with L-CD@Hg^{2+} in the excited state, causing it to undergo dynamic quenching. After reaching equilibrium, subsequent Hg^{2+} produces a large CD complex with L-CD, leading to a decrease in fluorescence strength. The sulfhydryl group on GSH binds specifically to Hg^{2+}, thereby restoring L-CD fluorescence. Furthermore, the real sample assay exposed that L-CD has good accuracy (RSD<5.0%) and can be used as a reliable "on-off-on" fluorescent sensor for the measurement of Hg^{2+} in complex aqueous solutions and the efficient identification of GSH in biomaterials. In conclusion, this work synthesized chiral L-CD with high QY under mild condition and verified for the first time the mechanism of the chiral structure involved in CD fluorescence recognition, which is conducive to the further development of chiral CD.

04 Prospects

- L-CD has good accuracy (RSD<5.0%) and can be used as a reliable "on-off-on" fluorescent sensor for the detection of Hg^{2+} in complex aqueous solutions and the efficient recognition of GSH in biological samples.
- This experiment synthesized chiral CDs with high quantum yield at mild conditions and first verified the mechanism of the chiral structure taking part in the fluorescence recognition of CDs, which provides an essential reference for the in-depth investigation of luminescent behaviors in CDs materials.

姓名：梁 浩　　单位：西北师范大学　　邮箱：18409567288@163.com

中国科学院大学
University of Chinese Academy of Sciences

前沿交叉科学学院
School of Advanced Interdisciplinary Sciences

氧空位动态调控在单原子纳米酶氧化酶活性提升中的应用

作者：江明杨#；吴列#；储晨晨#；张玉蓓#；华朝雷；李鑫；陈怡婕；刘关；张琼娣；喻学锋；周文华*；耿胜勇*

单位：中国科学院深圳先进技术研究院材料人工智能研究中心

引言 Introduction

单原子纳米酶（SANs）经过工程化改造，能够模拟天然酶的活性位点。凭借其出色的原子利用效率和独特的电子构型，SANs已成为一类极具前景的催化材料。然而，其催化位点的孤立性往往限制了其与载体基质的协同作用，导致在需要多位点协同参与的复杂反应中活性不佳。缺陷工程，例如在载体材料中引入氧空位（OVs）、氮空位或碳空位，为解决这一挑战提供了有效途径。该方法不仅能创造互补的活性位点，还能实现精确的电子调控，为通过位点-空位协同效应提升催化效率开辟了新途径。其中，OVs的调控因其能够精细调整载体缺陷结构，已被证明对开发高性能催化剂特别有效。因此，设计具有高密度、稳定氧空位的工程化单原子纳米酶，对于显著提高纳米酶的催化效率至关重要。

01 研究方法 Methods

本研究围绕介孔二氧化硅负载铂单原子催化剂（$mSiO_2$-PtSANs）的原子级设计与功能强化展开，提出光化学还原策略实现氧空位与Pt-O_6双催化中心的同步构建。通过空间位阻与静电作用将H_2PtCl_6前驱体封装于介孔硅孔道，利用CTAB模板的静电吸附将铂负载量提升至1.92 wt.%，同时其空间限域效应抑制了还原过程中铂原子的团聚；紫外照射触发H_2PtCl_6原位还原，精准锚定配位为Pt-O_6的单原子位点，并在Si-O-Pt界面动态生成OVs，且通过调节UV曝光时间可灵活调控OVs密度，突破了传统方法中双中心难以协同构建的限制。

实验与理论结合进一步阐明，动态生成的OVs显著提升了催化剂的类氧化酶（OXD）活性——米氏常数（Km）较无OVs体系降低34.3倍，催化效率（k_{cat}/K_m）提升62.8倍。密度泛函理论计算显示，OVs作为电子供体位点促进了O_2分子活化（吸附能降低0.38eV），加速了Pt-O_6位点向O_2的电子转移，并降低了·OH自由基的形成能垒（从1.25 eV降至0.78 eV），从而高效驱动活性氧（ROS）的产生。

基于上述特性，研究将铁死亡诱导剂RSL3载入$mSiO_2$介孔通道（载药效率65.8%），构建了$mSiO_2$-PtSANs@RSL3纳米催化体系。该系统通过化学动力学疗法（CDT）与铁死亡诱导的协同作用放大抗肿瘤效果：体外对4T1乳腺癌细胞的半数抑制浓度（IC50）低至0.82 μg/mL，体内荷瘤小鼠模型中肿瘤体积抑制率达89.7%，且无明显毒副作用。这一成果不仅建立了OVs介导单原子催化剂原子级精准设计的新范式，更为肿瘤协同治疗提供了兼具高效性与安全性的创新纳米平台。

02 研究结果 Results

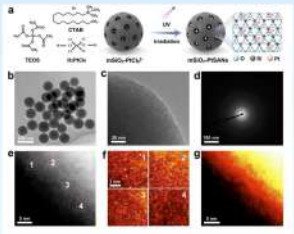

图1. $mSiO_2$-PtSANs的形貌表征。a) 合成过程示意图。b) TEM图像。c) HR-TEM图像。d) SAED图谱。e) AC HAADF-STEM图像。f) 图1e选定区域的放大彩色对比AC HAADF-STEM图像。g) 彩色对比AC HAADF-STEM图像。

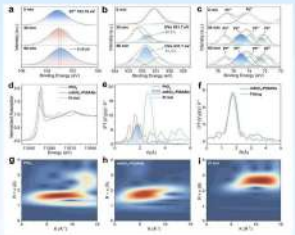

图2. $mSiO_2$-PtSANs的电子结构和化学状态分析。a-c) $mSiO_2$-PtSANs的Si 2p、O 1s和Pt 4f XPS谱图。d) 归一化XANES谱图。e) FT-EXAFS谱图。f) Pt K-edge拟合曲线。g–i) 小波变换谱图。

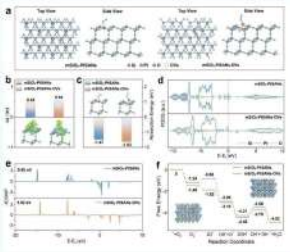

图3. DFT计算。a) $mSiO_2$-PtSANs和$mSiO_2$-PtSANs-OVs原子结构的俯视图与侧视图。b) 电子转移和c) 吸附能。d) PDOS分析。e) -ICOHP值。f) 反应路径的自由能图。

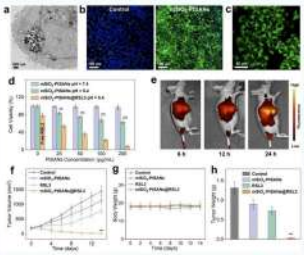

图4. 体外和体内抗肿瘤活性。 体外和体内抗肿瘤活性。a) MCF-7细胞与$mSiO_2$-PtSANs共培养12小时的生物TEM图像。b) 未经处理与经$mSiO_2$-PtSANs处理的细胞ROS（绿色）/细胞核（蓝色）荧光图像。c) $mSiO_2$-PtSANs@RSL3处理后的细胞LPO含量荧光图像。d) 不同浓度$mSiO_2$-PtSANs或$mSiO_2$-PtSANs@RSL3处理后的相对细胞活力，n=6。e) 静脉注射Cy5.5标记$mSiO_2$-PtSANs的小鼠体内荧光成像。f) 不同组别肿瘤生长曲线和g) 体重变化曲线，n=5。h) 治疗结束时肿瘤重量。

03 研究结论 Conclusion

本研究通过XPS、XANES及DFT计算系统解析了$mSiO_2$ PtSANs的结构特性与活性增强机制，并验证其肿瘤治疗效果：

XPS高分辨谱显示，60 min UV照射后Si 2p结合能偏移0.15 eV，对应Si-O键电子密度降低，源于OVs形成；O 1s谱中531.7 eV处新峰明确归属为OVs的O^{2-}物种，定量分析表明其占有率随照射时间延长至61.3%，验证了光照动态调控缺陷的可行性。同步观测到Pt^{2+}浓度与OVs形成呈正相关，源于光激活的电荷转移过程—— OVs作为电子供体促使晶格氧向Pt^{4+}中心转移电子，将其还原为Pt^{2+}，维持$mSiO_2$-PtSANs骨架内Pt^{2+} /Pt^{4+}的动态平衡，确保单原子分散稳定性。XANES吸收边能量介于Pt_0与PtO_2之间，结合FT-EXAFS主峰（1.81 Å）及WT谱与PtO_2的Pt-O信号匹配，确证Pt以原子级单分散存在且配位环境为Pt-O（图2）。

DFT计算构建OVs工程化模型进一步揭示活性增强本质：OVs引入使Pt位点与O_2间的电荷转移能从0.45 eV提升至0.54 eV，电子更易从Pt转移至O_2促进活化；O_2吸附能从-1.47 eV增强至-1.63 eV，更强的吸附利于O_2分子在Pt位点富集。投影态密度（PDOS）显示铂d带中心因OVs调制上移，费米能级态密度增加，优化了Pt-O分子轨道构型——占据态从反键轨道向成键轨道转变，晶体轨道哈密顿布居数（-ICOHP）证实O_2结合强度从0.95 eV提升至1.02 eV。关键反应路径分析中，$mSiO_2$-PtSANs-OVs上O-O键断裂能垒（0.52 eV）较原始体系（0.92 eV）降低56.5%，直接解释了实验中·OH生成速率显著提升的现象（图4）。

体外细胞实验中，TEM显示$mSiO_2$-PtSANs主要被MCF-7细胞内化并定位于胞质。酸性微环境（pH 5.4）下，DCFH-DA荧光强度较生理pH（7.4）提升2.3倍，证实OVs工程化显著增强ROS生成；BODIPY 581/591 C11检测显示，$mSiO_2$-PtSANs@RSL3处理组脂质过氧化物（LPO）水平达对照组的4.1倍，表明铁死亡通路被有效激活。细胞毒性实验中，生理pH下材料生物相容性优异（200 μg/mL细胞存活率>98%），而pH 5.4时呈现浓度依赖毒性；负载RSL3后协同效应显著，IC50从单一催化剂的1.8 μg/mL降至0.6 μg/mL。体内荷瘤小鼠模型中，纳米颗粒通过EPR效应6 h富集肿瘤，联合治疗组肿瘤体积在第14天仅为对照组的10%（抑制率90%），肿瘤重量较单药组降低76%（P<0.01）。组织病理显示，仅联合组存在广泛肿瘤坏死（核固缩、胞质崩解），小鼠体重全程稳定，验证了CDT与铁死亡协同的抗肿瘤安全性与有效性。这些发现为OVs介导的单原子催化剂原子级设计及多模式肿瘤治疗提供了关键实验与理论支撑。

04 研究前景 Prospects

本研究提出的光驱动动态空位工程策略为单原子纳米酶的设计和应用开辟了全新的方向。通过精确调控氧空位密度和单原子活性位点的构建，显著提升了纳米酶的催化性能，尤其在氧化酶样活性和肿瘤治疗中的应用表现出巨大的潜力。随着合成方法的进一步优化，光驱动技术不仅能够实现对催化剂的精准调控，还可在环境监测、疾病早期检测和精准医疗中发挥更大的作用。特别是在提高传感器灵敏度、选择性和检测速度方面，光驱动技术有望为生物医学领域带来突破，提供更高效的诊断和治疗方案。

在肿瘤治疗方面，纳米酶通过与铁死亡机制的协同作用，显著增强了抗肿瘤效果。通过光化学还原策略调控氧空位，不仅可以提升纳米酶的催化活性，还能通过优化电子结构实现精确的药物递送与靶向治疗。未来，随着单原子纳米酶技术的不断发展和氧空位调控方法的精细化，纳米酶将在癌症靶向治疗、免疫治疗以及其他生物医学应用中展现更广阔的前景。此外，纳米酶的高效能还可以推动其在环境保护和能源转化等领域的应用，特别是在污水处理、废气净化以及绿色能源生产等方面，具有潜在的商业化价值。总之，基于光驱动动态空位工程的单原子纳米酶，为相关领域的技术进步提供了新的思路和可能性。

姓名：储晨晨　　单位：中国科学院深圳先进技术研究院　　邮箱：cc.chu@siat.ac.cn

中国科学院大学
University of Chinese Academy of Sciences

前沿交叉科学学院
School of Advanced Interdisciplinary Sciences

稀土氧化物纳米平台的构建及其在焦亡介导肿瘤免疫治疗中的应用

于思琪，张雨墨，赵宇亮，李九龙*，孟幻*

中丹学院，中国科学院大学，北京，100190

引言 Introduction

稀土氧化物的免疫调节机制尚不明确。本研究制备了具有空腔结构和富氧空位的氧化镝纳米管自组装颗粒（Dy_2O_3-T），其在酸性肿瘤环境中可加速 Dy^{3+} 释放并在溶酶体内转化为磷酸镝。Dy_2O_3-T 可高效诱导 EMT6 细胞发生 GSDME 依赖性焦亡，通过溶酶体-caspase-3 途径作用，效果优于商业 Dy_2O_3。在 GSDME^{high} EMT6 小鼠中，Dy_2O_3-T 激活显著免疫反应并与抗 PD-1 协同；在 GSDME^{low} 4T1 中联合 GSDME mRNA 可恢复焦亡与免疫效应。结果证明 Dy_2O_3-T 是强效且可工程化的肿瘤免疫纳米平台。

01 研究方法 Methods

- 采用水热自组装制备空腔结构、富氧空位的氧化镝纳米颗粒，并表征其形貌与缺陷结构。
- 评估 Dy_2O_3-T 的溶酶体特异性生物转化及离子释放行为。
- 在 GSDME^{high}与 GSDME^{low}小鼠模型中验证免疫激活及与 PD-1 的联合疗效。

02 研究结果 Results

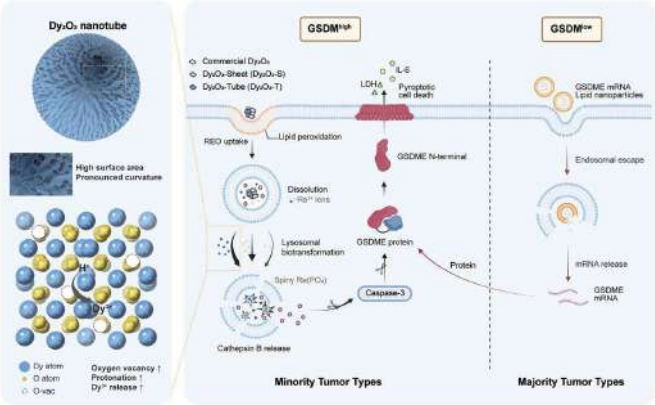

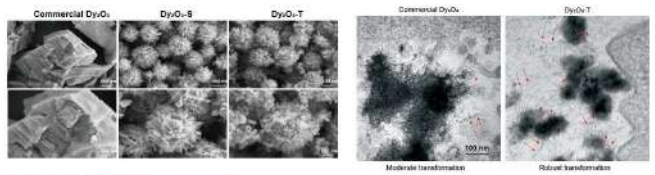

In GSDME^{high} EMT6 breast cancer

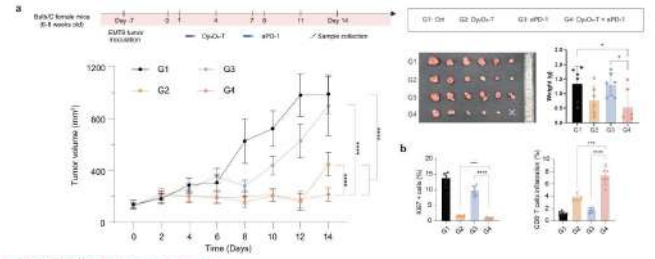

In GSDME^{low} 4T1 breast cancer

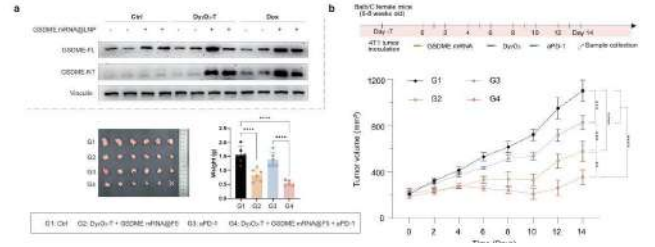

03 研究结论 Conclusion

本研究系统阐明了氧化镝（Dy_2O_3）及其结构工程化纳米管结构（Dy_2O_3-T）在诱导肿瘤细胞焦亡和激活抗肿瘤免疫中的关键机制与治疗潜力。

1. **Dy_2O_3 具有天然的焦亡诱导能力。**
   在十种稀土氧化物中，Dy_2O_3 对 GSDME^{high} EMT6 细胞的细胞毒性最强，可诱导 GSDME 裂解、细胞膜起泡和典型焦亡形态学改变。TEM 与 EDX 证实 Dy_2O_3 在胞内发生生物转化，形成 Dy–磷酸盐复合物并造成膜破裂，触发 GSDME 依赖性焦亡。
2. **结构工程化的 Dy_2O_3-T 具有更高的缺陷密度与生物反应性。**
   Dy_2O_3-T 具备管状自组装空腔结构，表面积提升约 8.4 倍，富含氧空位，表现出更快的 Dy^{3+} 释放和更强的细胞膜破坏能力。其在溶酶体中快速发生结构变化并高效转化，显著增强焦亡诱导效率。
3. **Dy_2O_3-T 可介导溶酶体损伤并强力启动 GSDME 依赖性焦亡。**
   Dy_2O_3-T 导致溶酶体膜蛋白广泛去磷酸化，提示溶酶体完整性受损；同时显著提升 GSDME-NT 片段，表明其焦亡诱导更为强烈。转录组显示免疫和炎症通路显著上调，包括细胞因子及 PD-L1/PD-1 信号。CT 成像进一步证明 Dy_2O_3-T 在肿瘤内具有持续滞留和良好扩散性。
4. **Dy_2O_3-T 与抗 PD-1 协同实现强效抗肿瘤治疗。**
   在 GSDME^{high} EMT6 模型中，Dy_2O_3-T + 抗 PD-1 显著抑制肿瘤生长，增强 CD8$^+$ T 细胞浸润和 IFN-γ 水平，且无系统毒性。在 GSDME^{low} 4T1 模型中，通过 GSDME mRNA-LNP 恢复 GSDME 表达后，Dy_2O_3-T 可重新诱导焦亡，并与抗 PD-1 协同发挥明显抑瘤和免疫激活效果，同样未观察到毒性。

04 研究前景 Prospects

本研究揭示了 Dy_2O_3 通过生物转化与溶酶体损伤诱导焦亡的潜力，并证明结构工程化的 Dy_2O_3-T 可作为高效的焦亡驱动纳米平台。未来，可进一步优化 Dy_2O_3-T 的尺寸、形貌与缺陷结构，以提升其在肿瘤微环境中的生物转化效率和免疫激活能力。针对广泛存在的 GSDME^{low} 肿瘤类型，将 Dy_2O_3-T 与基因递送体系（如 GSDME mRNA-LNP）结合，仍具有显著的拓展空间，可实现更全面的焦亡重建与免疫唤醒。通过推进安全性、药代动力学及长期免疫效应的系统评估，该平台有望发展为适用于多类型实体瘤的可转化纳米免疫治疗策略。

姓名：于思琪　　单位：国家纳米科学中心 & 中丹学院　　邮箱：yu_siqi00@163.com

中国科学院大学
University of Chinese Academy of Sciences

前沿交叉科学学院
School of Advanced Interdisciplinary Sciences

靶向诱导肿瘤焦亡的OMV用于治疗免疫冷肿瘤

高晓宇

国家纳米科学中心，中国科学院大学，北京，100190

引言 Introduction

细菌外膜囊泡（OMVs）因其天然免疫原性，作为疫苗载体被广泛研究。但OMVs皮下注射易引发肿瘤微环境负反馈，且作用机制主要依赖于天然免疫细胞。本研究构建GD-OMV纳米平台，为基于OMVs的免疫治疗提供新策略与新机制。

01 研究方法 Methods

首先，通过化学交联技术，利用具有谷胱甘肽（GSH）响应性的连接子将焦孔素蛋白GSDMD整合至OMVs表面，构建GD-OMV纳米平台。采用多种手段对其形貌、尺寸及结构进行表征，通过体外实验验证其在GSH环境下的蛋白释放能力。随后，建立皮下瘤小鼠模型，通过静脉注射给药，利用活体成像技术评估其在肿瘤部位的富集情况。监测肿瘤体积变化评估其抗肿瘤效果，并利用免疫学方法分析肿瘤微环境中免疫细胞浸润及细胞因子水平，以揭示其通过诱导焦亡逆转免疫抑制的作用机制。

02 研究结果 Results

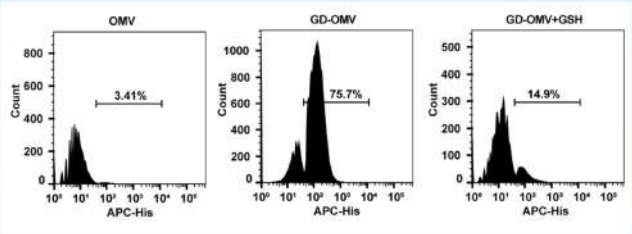

GD-OMV 的构建及 GSH 响应性释放

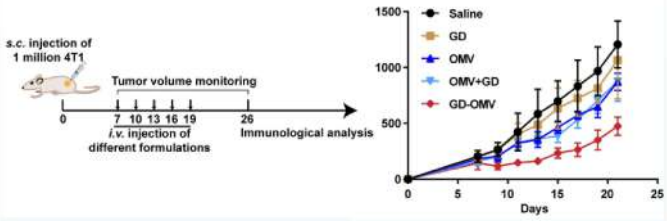

GD-OMV 在皮下肿瘤模型中的抗肿瘤作用

03 研究结论 Conclusion

本项目依据OMV的成分、结构特征和细胞焦亡的必要条件开发了一种肿瘤焦亡新技术。本研究构建了GD-OMV纳米平台。该平台通过具有GSH响应性的连接子，将关键的焦孔素蛋白GSDMD高效地交联于OMV表面。 GSDMD蛋白的包裹可避免由于 OMV 高免疫原性所导致的血液快速清除，并且遮蔽了表面 LPS 以提高 OMV 血液注射的安全性。

在皮下肿瘤模型中，本研究证实了GD-OMV能够通过静脉注射后依赖其纳米尺寸效应高效富集于肿瘤部位。进入肿瘤细胞后，GD-OVM在细胞内高浓度GSH的触发下释放GSDMD。与此同时，OMV本身所携带的丰富LPS可有效激活细胞内的Caspase-11炎症小体通路。活化的Caspase-11进而精确切割GSDMD，释放其N端孔道结构域，该结构域在肿瘤细胞膜上形成孔道，从而精准地触发肿瘤细胞发生焦亡，释放大量肿瘤抗原、DAMPs 和促炎因子，有效调控系统性免疫反应，使得免疫冷肿瘤变成免疫热肿瘤，改善肿瘤免疫抑制微环境。该项目为基于 OMV 的肿瘤治疗提供了新策略和新机制。

04 研究前景 Prospects

本研究开发的GD-OMV平台为基于细菌外膜囊泡（OMV）的肿瘤免疫治疗提供了新范式，其精准诱导焦亡并逆转免疫抑制的机制，在联合其他疗法治疗免疫冷肿瘤方面具有广阔的临床转化前景。

姓名：高晓宇　　单位：国家纳米科学中心　　邮箱：gaoxy2021@nanoctr.cn

中国科学院大学
University of Chinese Academy of Sciences

前沿交叉科学学院
School of Advanced Interdisciplinary Sciences

时间分辨光致发光研究纳米纤维与蛋白质相互作用的动态自组装

张瑞佳，徐翰林，任超，姚庆鑫，高远*
国家纳米科学中心，中国科学院大学，北京，100190

引言 Introduction

超分子纳米纤维与蛋白质之间的相互作用，对于功能性生物材料而言至关重要。然而，目前尚缺乏能够直接阐释超分子纳米纤维 - 蛋白质相互作用的方法。与单组分体系类似，我们证实了时间分辨光致发光（PL）可有效监测两组分体系的共组装过程以及纳米纤维-蛋白质之间的动态自组装过程。以用于模型组装的四肽FFKY为例，其荧光组装分子与非荧光组装分子的共组装影响了其荧光寿命，通过该变化能够对非荧光组装分子的组装动力学参数进行量化分析。我们同样利用此方法对纳米纤维 - 蛋白质复合物展开监测。自组装过程中的变化情况表明，超分子纳米纤维与特定蛋白质之间存在选择性相互作用。总体而言，时间分辨光致发光技术是一种适用于在高度动态且非平衡条件下，体外研究纳米纤维 - 蛋白质相互作用的有效手段 。

01 研究方法 Methods

- **核心技术**: **时间分辨光致发光**。
- **基本原理**: 荧光寿命与分子组装状态相关（单体的荧光寿命短，组装体的荧光寿命长）。
- **关键模型**: 通过**双指数衰减模型** $I(t) = A + I_1 e^{-t/\tau_1} + I_2 e^{-t/\tau_2}$ 对荧光衰减曲线进行解卷积，得到单体 (τ_1) 和组装体 (τ_2) 的比例。

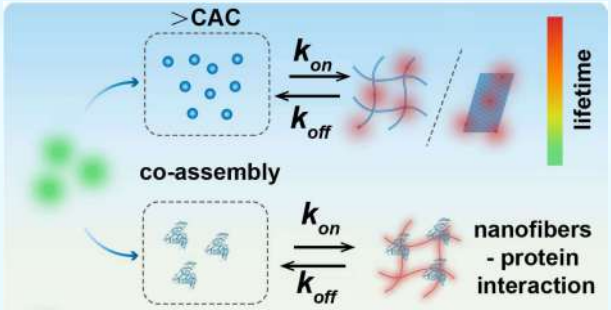

图1：时间分辨PL揭示动态共组装过程

02 研究结果 Results

第一部分：测定非荧光组分的组装动力学

- **模型体系**: 荧光多肽 **NapFFK(dansyl)Y** + 非荧光多肽 **NapFFK(Nap)Y**。
- 通过固定荧光多肽浓度，改变非荧光多肽浓度，成功测定了非荧光肽的**临界组装浓度 CAC** 和**组装/解组装速率常数（k_{on}：k_{off}）**

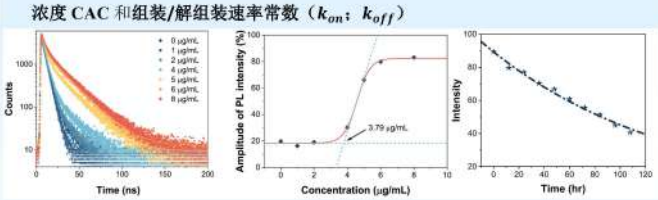

图2：(左) 不同浓度下的荧光寿命曲线；(中) 通过PL强度确定非荧光多肽的CAC；(右)共组装体系解组装过程中PL强度变化

揭示纳米纤维-蛋白质特异性相互作用

- **模型蛋白质**: BSA (α-螺旋丰富) 和 β-LG (β-折叠丰富)。
- **关键发现**:
  ① BSA能**促进**荧光肽在低于 CAC 浓度下组装成纳米纤维，而 β-LG 不能。
  ② BSA与纳米纤维形成复合物，并**显著延缓**纳米纤维的解组装动力学。
  ③ TEM图像显示纳米纤维与BSA蛋白簇结合。

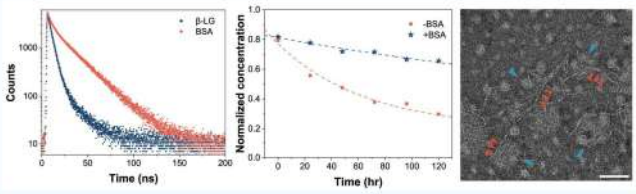

图3：BSA（而非β-LG）与纳米纤维发生特异性相互作用，促进组装并稳定纤维结构

03 研究结论 Conclusion

- 开发了一种基于时间分辨PL的通用方法，用于实时、定量研究动态自组装。
- 成功将应用从单组分体系拓展至多组分共组装体系，并能测定非荧光组分的组装动力学。
- 首次实现了对纳米纤维-蛋白质相互作用的动力学层面的监测与验证。
- 揭示了蛋白质对纳米纤维组装的选择性调控作用。

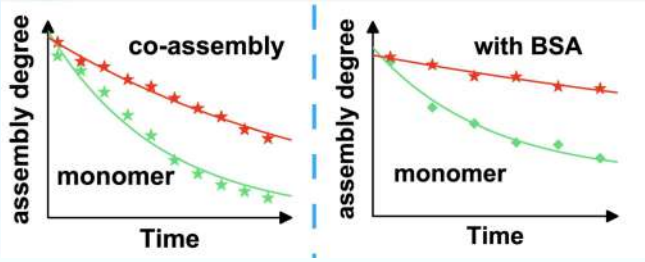

图4：(左) 测定共组装体系的组装动力学；(右)蛋白质对纳米纤维组装的选择性调控作用

开发了一种实时、定量的动态相互作用研究新范式

- **结论一：方法创新，突破局限**

  成功将**时间分辨光致发光技术**应用于**两组分动态共组装系统**，实现了对**非荧光组分**组装动力学的定量测量，突破了传统方法仅限荧光体系的局限。

- **结论二：揭示相互作用，证实特异性**

  首次在**动力学层面**证实了超分子纳米纤维与蛋白质（BSA）之间存在**特异性、高亲和力的相互作用**，该相互作用能**促进组装**并**显著稳定组装体结构**。

- **结论三：提供普适性研究工具**

  本方法为在高度动态、非平衡的复杂生物环境中，实时研究超分子组装体与各类生物大分子的相互作用，提供了一个**强大、通用且定量的研究平台**。

04 研究前景 Prospects

- 方向一：**靶向蛋白质探索**

  利用此方法，系统性探索纳米纤维与疾病关键蛋白（如K-RAS, p53等）的相互作用，为理解疾病机制提供新视角。

- 方向二：**智能生物材料设计**

  基于对相互作用动力学的精确理解，理性设计能够特异性捕获、调控或递送靶蛋白的智能型超分子材料。

- 方向三：**诊断与治疗应用**

  在疾病诊断（如生物传感器）和靶向治疗（如药物递送系统）等领域展现出巨大的应用潜力。

[1] Zhang, R., Xu, H., Ren, C., Yao, Q. and Gao, Y.* **Small**, *2025*, 21, 2411343.
[2] Hu, X.#, Yao, Q.#, Wu, X.#, Chen, J., Zhang, R., Zhao, Y. and Gao, Y.* **Nat. Commun.** *2025*, 16, 5974.

姓名：张瑞佳　　单位：国家纳米科学中心　　邮箱：zhangrj2020@nanoctr.cn

中国科学院大学
University of Chinese Academy of Sciences

前沿交叉科学学院
School of Advanced Interdisciplinary Sciences

基于ATTEC技术治疗肥胖相关代谢综合征的研究

张小瑜，赵颖，聂广军*
国家纳米科学中心，中国科学院大学，北京，100190

引言 Introduction

肥胖相关代谢综合征已成为全球性公共健康挑战，表现为腹型肥胖、血糖血脂异常、高血压等症状，由高脂饮食引发脂滴堆积、线粒体功能障碍及慢性炎症导致。

01 研究方法 Methods

➢ **分子设计与合成**

构建三元 ATTEC 分子，同时搭载脂滴配体、线粒体配体及自噬体配体，实现 “分子桥” 作用。

结合分子对接筛选最优结构，通过**薄层色谱（TLC）结合机器学习**优化合成工艺，提升产率。

➢ **实验模型与检测**

细胞实验：以脂肪细胞为研究对象，检测脂滴降解、线粒体形态及细胞毒性。

动物模型：构建 C57BL/6J 小鼠代谢综合征模型。

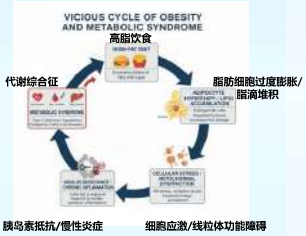

02 研究结果 Results

➢ **分子对接模拟结果显示药物分子与靶点结合能分别为 -6.93、-5.38 kcal/mol，通过氢键稳定结合靶点。**

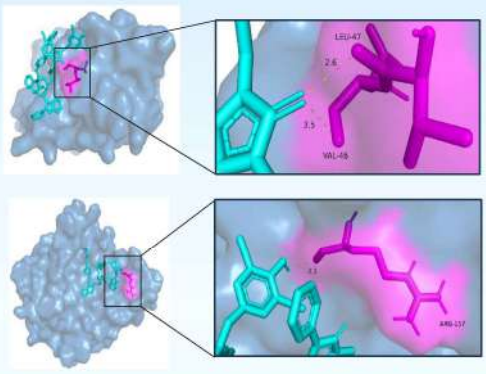

➢ **构建稳定的代谢综合征小鼠模型，为后续体内药效验证及机制研究奠定基础**

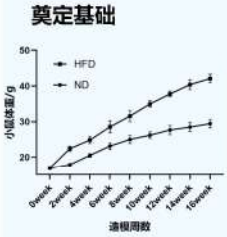

脂肪组织油红染色

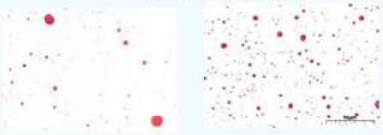

Control组　　HFD组 (16 weeks)

03 研究结论 Conclusion

➢ **成功设计并合成具有靶向识别功能的三元 ATTEC 分子，实现脂滴与受损线粒体的同步选择性自噬。**

➢ **细胞实验证实 ATTEC 分子可有效降解脂滴、修复线粒体功能，且生物安全性良好。**

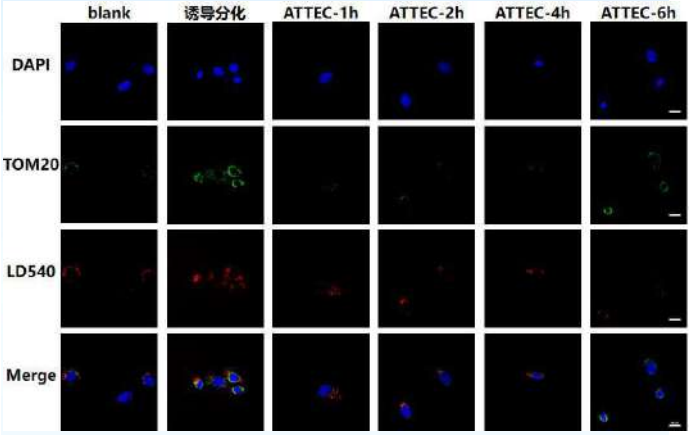

➢ **动物实验证实ATTEC分子可有效降低体重，调控血糖，修复维持正常代谢调控稳态。**

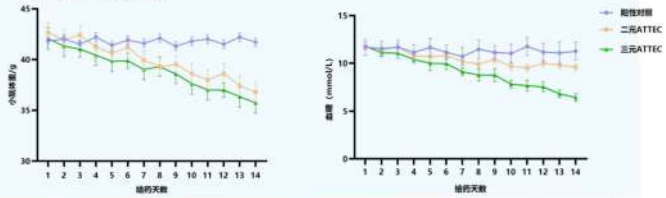

04 研究前景 Prospects

➢ **ATTEC 技术通过重建细胞能量代谢活性，为肥胖相关代谢综合征治疗提供了创新性解决方案。**

姓名：张小瑜　　单位：国家纳米科学中心　　邮箱：zhangxy2023@nanoctr.cn

中国科学院大学
University of Chinese Academy of Sciences

前沿交叉科学学院
School of Advanced Interdisciplinary Sciences

金属-核酸配位纳米颗粒增强先天免疫用于肿瘤免疫治疗

黄焱娟#，李宜珂#，孙佳姝*
国家纳米科学中心，中国科学院大学，北京，100190

引言 Introduction

Metalloimmunotherapy represents a new paradigm in cancer immunotherapy by leveraging the immune-modulatory functions of metal ions, either alone or in combination with agonists. However, the low bioavailability of free metal ions and agonists limits robust stimulation of antitumor immune responses. Here we developed multivalent metal–nucleotide nanoagonists (Mn-MNAs) through aqueous coordination of multiple nucleotide based innate immune agonists with $Fe^{2+}$and Mn^{2+}, which not only enhanced the stability and cellular uptake of the agonists but also amplified the antitumor immunity by concurrently activating the stimulator of interferon genes (STING) and toll-like receptor 9 (TLR9) pathways in the CT26 and B16F10 tumor model. Overall, multivalent nanoagonists open new avenues for cancer metalloimmunotherapy.

01 研究方法 Methods

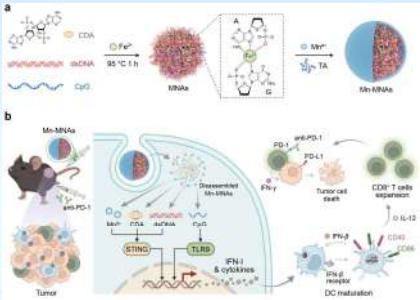

Figure 1. Schematic illustration of multivalent metal–nucleotide nanoagonists (Mn–MNAs) for enhanced cancer immunotherapy.

02 研究结果 Results

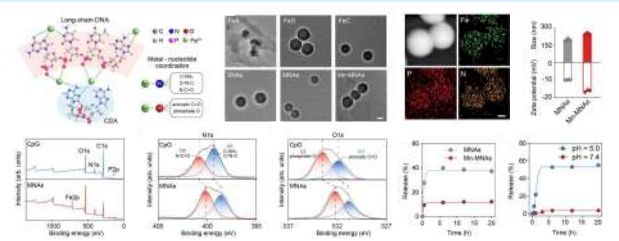

Figure 2. Characterization of Mn-MNAs.

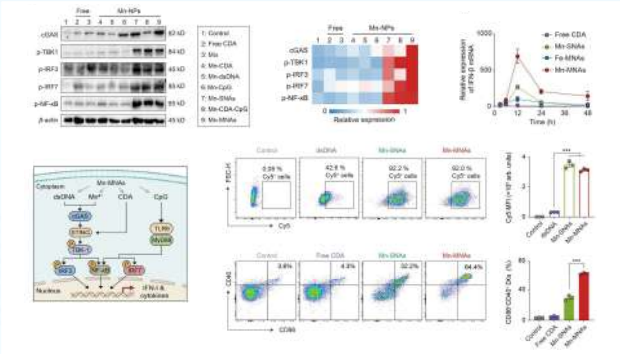

Figure 3. In vitro immunological activation by Mn-MNAs.

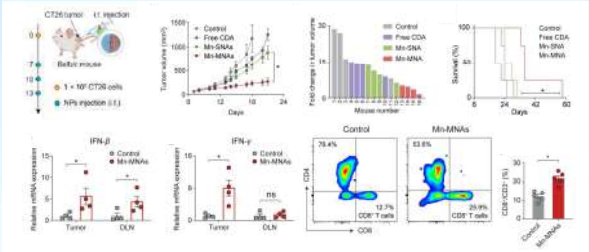

Figure 4. Mn-MNAs enhance anti-tumor efficacy in CT26 colon tumor model by promoting pro-inflammatory cytokine expression and $CD8^+$ T cell expansion.

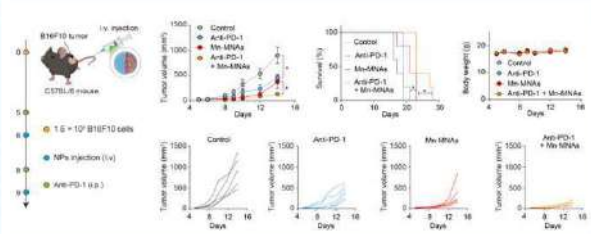

Figure 5. Mn-MNAs enhance anti-tumor efficacy in B16F10 melanoma tumor model via systemic injection.

03 研究结论 Conclusion

In this study, multivalent metal–nucleotide nanoagonists (Mn-MNAs) have been constructed through simple but efficient coordination-driven self-assembly to enhance cancer metalloimmunotherapy. These Mn-MNAs composed of multiple nucleotide-based agonists and Mn^{2+} exhibited well-defined spherical morphology, high agonist-loading efficiency, excellent physiological stability, and enhanced cellular uptake. The synergistic activation of the STING and TLR9 pathways by Mn-MNAs elicited amplified and prolonged anti-tumor immune responses. Notably, systemic administration of Mn-MNAs effectively suppressed the growth of poorly immunogenic B16F10 melanoma tumors, and markedly extended animal survival when combined with checkpoint therapy.

04 研究前景 Prospects

This strategy holds significant potential as a platform not only for the DNA delivery, but also for the next generation of mRNA vaccines, opening new avenues for cancer immunotherapy.

姓名：黄焱娟　　单位：中国科学院大学国家纳米科学中心　　邮箱：huangyj2021@nanoctr.cn

中国科学院大学
University of Chinese Academy of Sciences

前沿交叉科学学院
School of Advanced Interdisciplinary Sciences

基于集成微流体装置的循环肿瘤细胞高纯度富集用于单细胞分析

夏晨峰[a]，吴淑婷[b]，王小波[c]，李雪杰[a]，陈丹蕾[a]，曾萍萍[b]，胡志远[a,b*]，王涛[c*]，方治国[d*]

a.国家纳米科学中心，中国科学院大学，北京，100190，中国

b.福建医科大学基础医学院，福建，福州，350108，中国

c.中国人民解放军总医院肿瘤医学部，北京 100071，中国

d.西南大学药学院，重庆，400715，中国

引言 Introduction

Circulating tumor cells (CTCs) serve as crucial biomarkers for cancer diagnosis, treatment monitoring, and drug resistance assessment. However, their extreme rarity and biological heterogeneity pose significant challenges for reliable isolation from whole blood. Traditional CTC enrichment methods often suffer from low purity, long processing times, or damage to cellular viability, limiting their compatibility with downstream single-cell analyses. To address these limitations, we developed an integrated magnetic-fluidic device that enables rapid, high-purity, and viability-preserving enrichment of CTCs directly from whole blood. The system combines immunomagnetic nanoparticle labeling with precisely engineered microfluidic flow fields, allowing efficient capture of epithelial CTCs while minimizing background contamination.

01 研究方法 Methods

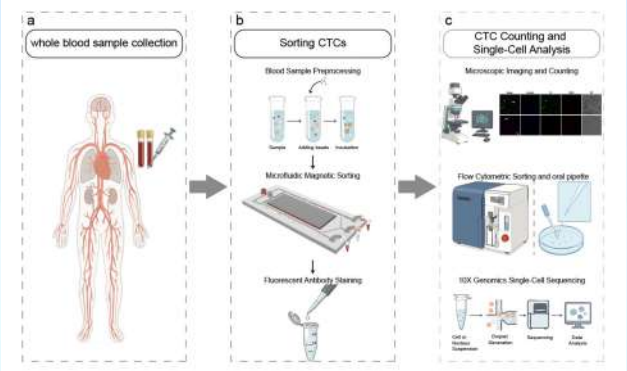

Figure 1. Schematic workflow of circulating tumor cells isolation and downstream analysis. (a) Peripheral blood was collected from patients. (b) CTCs in the blood were first captured by EpCAM antibody-modified magnetic beads. The blood sample was then injected into the device for sorting, and after 2 minutes under the action of magnetic force and fluid resistance, the enriched fraction was collected at the designated CTC outlet. Subsequently, it was stained with pan-CK$^+$/CD45$^-$/Hoechst$^+$ markers for reliable CTC identification. (c) The captured cells were validated by microscopic imaging and immunofluorescence staining and then used for single-cell multi-omics analysis.

02 研究结果 Results

Model System & Optimization of Flow Parameters:

MCF-7 breast cancer cell line was added to PBS solution. By adjusting the inner and outer flow rates of the device, the optimal operating conditions were determined as follows:

- **Inner PBS sheath flow: 450 μL/min**
- **Outer sample flow: 250 μL/min**

Under these conditions, magnetically labeled MCF-7 cells exhibited sufficient lateral magnetic displacement while avoiding shear stress induced by excessive flow velocity, providing a stable and efficient environment for cell sorting.

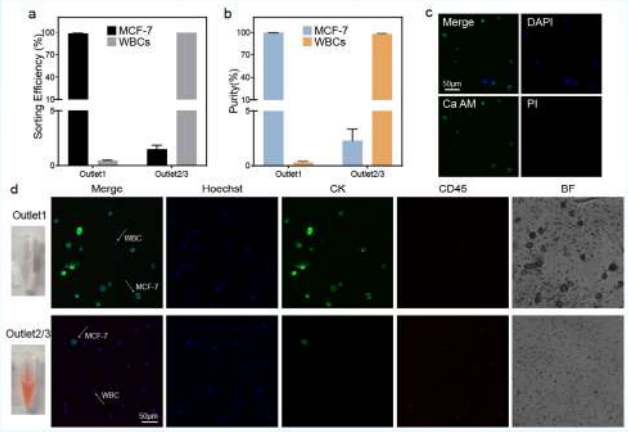

Figure 2. performance evaluation of the magnetic-fluidic device.

(a-b) Using spiked MCF-7 artificial blood samples, the device achieved :

- **CTC (MCF-7) recovery rate: 98.50%**
- **WBC depletion efficiency: 99.55%**
- **Final CTC purity: 99.68%**

(c) Live/dead staining with **Calcein AM$^+$ / PI$^-$** showed that enriched CTCs maintained outstanding viability with no observable membrane damage.

(d) Representative immunofluorescence images of cells collected from Outlet 1 (CTC-enriched fraction) and Outlet 2/3 (WBC-enriched fraction). MCF-7 cells are identified as Hoechst$^+$/CK$^+$/CD45$^-$, while WBCs are Hoechst$^+$/CK$^-$/CD45$^+$. BF: bright-field images (Scale bar = 50 μm).

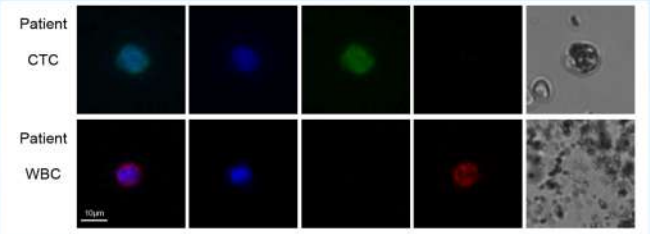

Figure 3. Detection of CTCs in breast cancer patient blood samples using the magnetic–fluidic device. The magnetic–fluidic device was applied to peripheral blood samples from breast cancer patients to assess its capability for capturing CTCs in real clinical specimens. **CTCs: Hoechst$^+$/pan-CK$^+$/CD45$^-$; WBCs: Hoechst$^+$/pan-CK$^-$/CD45$^+$**, the device successfully isolated rare CTCs from the clinical samples. These results confirm the feasibility and clinical applicability of the magnetic–fluidic platform for efficient and reliable CTC detection in breast cancer patient blood.

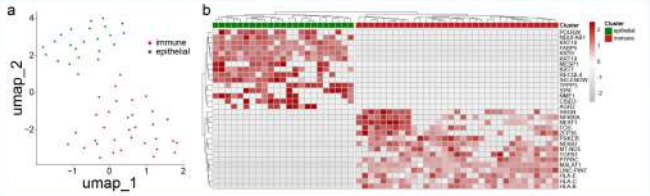

Figure 4. Single-cell transcriptomic profiling of CTCs from a breast cancer patient. To evaluate the platform's suitability for CTC molecular analysis, single-cell transcriptomic sequencing was performed on CTCs enriched from 6 mL peripheral blood of a breast cancer patient. (a) UMAP analysis classified 56 enriched cells into epithelial cluster (23 CTCs) and immune cluster. (b) A heatmap of differentially expressed genes (n=56) distinguished the two clusters (epithelial: green; immune: red), with distinct key gene expression patterns: the epithelial cluster highly expressed cytokeratin genes (KRT7, KRT8, KRT18, KRT19), and the immune cluster highly expressed immune cell-related genes (e.g., PTPRC (CD45)).

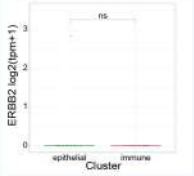

Figure 5. ERBB2 (HER2) expression was uniformly low and not significantly different between the two clusters. Notably, the patient was pathologically confirmed as HER2-Low breast cancer and received T-DXd (a HER2-targeted drug) after blood collection. However, our platform's enrichment analysis showed the HER2 loss phenotype was already captured in the pre-treatment CTC transcriptome; follow-up revealed new liver metastases after only 2 treatment cycles (2 months), with radiological evidence of disease progression.

03 研究结论 Conclusion

This study focused on the development and validation of technologies for CTC enrichment and clinical application, with the key conclusions as follows:

1. **A magnetic-fluidic device was successfully developed, enabling rapid enrichment of high-purity viable circulating tumor cells (CTCs) directly from whole blood;**
2. **Its reliability in enriching CTCs from patients' blood was validated using real clinical samples;**
3. **The device exhibits excellent compatibility with downstream single-cell transcriptomic analysis;**
4. **By combining enrichment analysis with single-cell RNA sequencing (scRNA-seq), Combined with scRNA-seq, clinically relevant biological features were identified. This molecular signal preceded radiological progression by ~2 months, implicating target loss and clonal heterogeneity, and demonstrating CTC transcriptomes' potential to predict therapeutic failure before conventional imaging.**

04 研究前景 Prospects

Future research will focus on the following directions:

1. Conduct multi-center, longitudinal clinical validation to further confirm the platform's applicability and stability in various clinical scenarios;
2. Integrate multi-omics technologies (e.g., CITE-seq, single-cell DNA/ATAC sequencing) to achieve more comprehensive molecular characterization of CTCs;
3. Optimize immunocapture strategies to improve the detection rate of mesenchymal or rare subclonal CTCs through antibody cocktail combinations;
4. Develop automated analytical pipelines to provide technical support for real-time clinical reporting.

姓名：夏晨峰　　单位：国家纳米科学中心　　邮箱：xiacf2023@nanoctr.cn

中国科学院大学
University of Chinese Academy of Sciences

前沿交叉科学学院
School of Advanced Interdisciplinary Sciences

Artificial intelligence-guided design of LNPs for in vivo targeted mRNA delivery via analysis of the spatial conformation of ionisable lipids

Lin-Jia Su†, Nan-Nan Wang†, **Rui Luo**†, Zi-Han Ji, Yurui Gao*, Hao Wang*, Yao-Xin Lin*
Laboratory of Theoretical and Computational Nanoscience, National Center for Nanoscience and Technology (NCNST), Beijing, P. R. China. 100190

引言 Introduction

Lipid spatial conformation influences the assembly, delivery, and release of mRNA drugs. We developed a series of novel ionizable lipids with varying structural features, including polar amino heads, degradable linkers, and hydrophobic tails, which generate different spatial conformations. Using molecular dynamics (MD) simulations, we identified over 2,000 spatial conformations for each lipid in the aqueous phase. Experimental data confirmed that the arrangement of head and tail groups is crucial for mRNA delivery efficiency and organ-specific expression.

To accelerate lipid discovery and design, we converted these spatial conformation data into 3D density maps, projecting structural features for further analysis. Machine learning models, trained with minimal chemical structure features, identified optimal lipids with 80% accuracy. AI-guided lipids displayed stable conical conformations. Notably, lipid P1, with its unique three-tail structure, enhanced spleen-targeted mRNA delivery by promoting IgM protein corona formation.

01 研究结果 Results

• Data Development

Spatial conformation facilitates mRNA binding and release

Spatial conformation facilitates delivery efficiency in vitro and in vivo

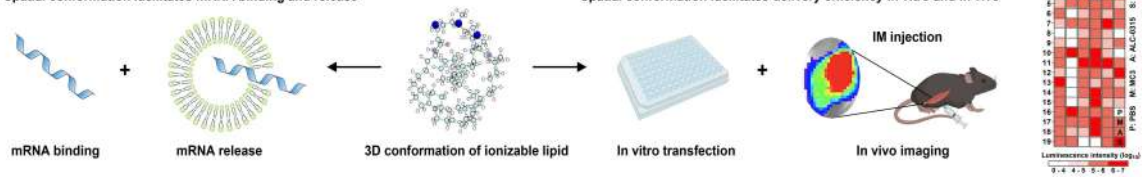

Small Dataset

n = 115

• Model Development

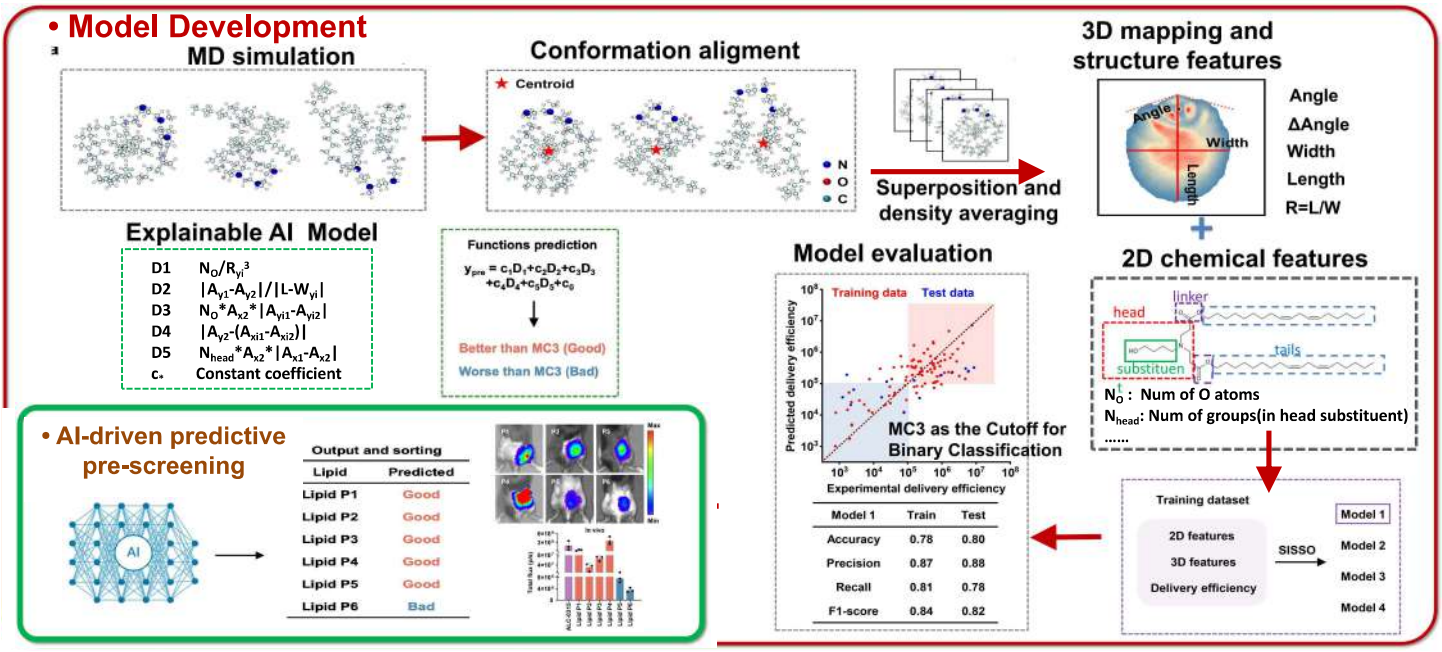

02 研究结论 Conclusion

This study highlights the importance of lipid spatial conformation, showing that cone-shaped lipids with exposed head groups enhance mRNA encapsulation, membrane insertion, and endosomal escape. Machine learning models identified these lipids as more efficient, with better tissue targeting and faster mRNA release. These findings stress the need to consider lipid geometry and tail arrangement in mRNA delivery system design. While AI has accelerated lipid discovery, further research is needed to improve datasets and methods for capturing lipid conformation complexity. Future progress will optimize lipid nanoparticles for more efficient and targeted mRNA therapies.

姓名：罗锐 单位：国家纳米科学中心 邮箱：luor2021@nanoctr.cn

中国科学院大学
University of Chinese Academy of Sciences

前沿交叉科学学院
School of Advanced Interdisciplinary Sciences

Bioinformatics-Driven Design of Peptides for Membrane Stabilization During Cryopreservation

Yihang Gao†, Ying Ou†, Yurui Gao*, Shenglin Jin*, jianjun Wang*

Laboratory of Theoretical and Computational Nanoscience, National Center for Nanoscience and Technology (NCNST), Beijing, P. R. China. 100190

引言 Introduction

During cryopreservation, cooling shifts cell membranes from a liquid-crystalline to a gel phase, impairing water transport and causing cell death. Inspired by G3LEA proteins, we conducted a bioinformatics analysis of 11-mer repeats across LEA proteins and identified AKE, a class A α-helical peptide that reduces phase transition temperature (T_m). Structural optimization produced a charge-segregated helix with segregated positive faces, enhancing electrostatic binding to lipid heads and hydrophobic insertion into tails. Replacing lysine with arginine strengthened interactions and lowered free energy. The resulting peptide, ARE, further reduced T_m, improved water permeability and osmotic resistance, and increased post-thaw RBC recovery by 52%. By integrating structural design with charge modulation, this study establishes a regulatory model of membrane behavior during low-temperature phase transition and provides a theoretical framework and design basis for the rational development of membrane-stabilizing peptides.

01 研究结果 Results

• Peptides Design

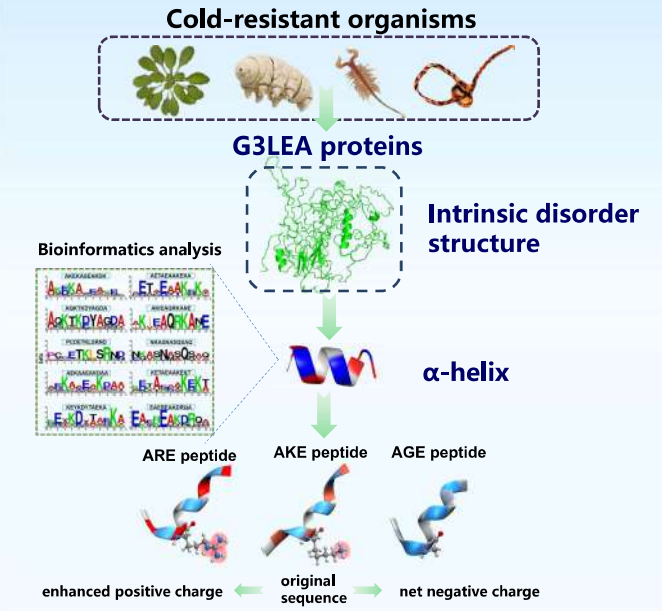

• Mechanism of Peptide-Mediated Cryoprotection

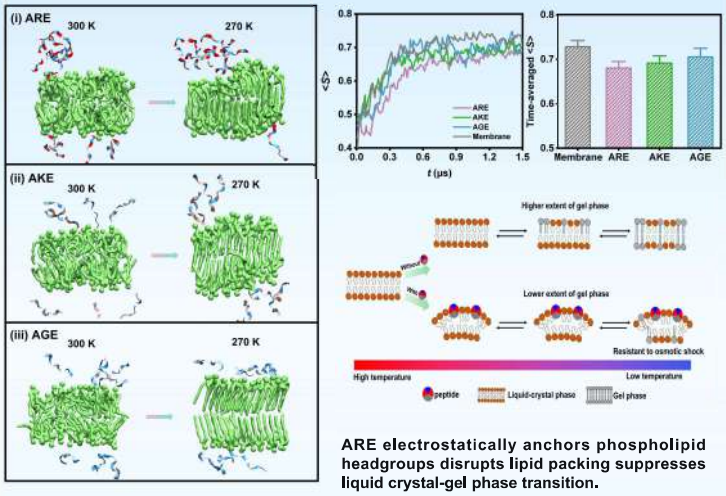

ARE electrostatically anchors phospholipid headgroups disrupts lipid packing suppresses liquid crystal-gel phase transition.

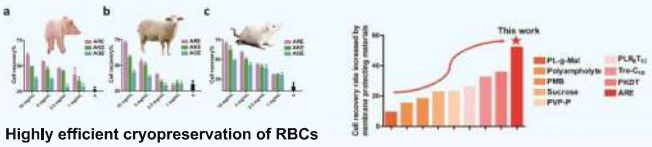

Highly efficient cryopreservation of RBCs

• Molecular Insights into Peptide-Membrane Interactions

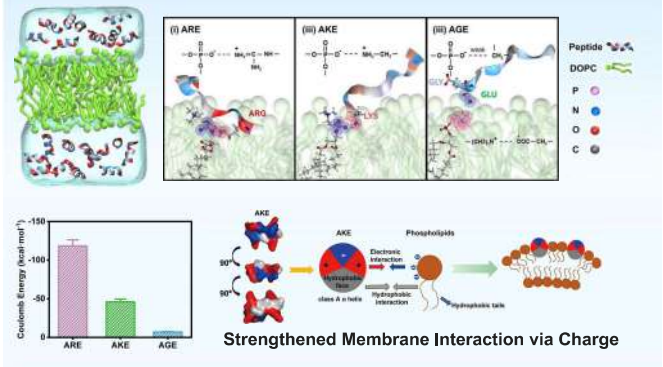

Strengthened Membrane Interaction via Charge

Reference: *Angew. Chem. Int. Ed*, **2025**, e202516336

02 研究结论 Conclusion

This study establishes a structural design principle for membrane-stabilizing peptides, exemplified by the optimized peptide ARE. Featuring a charge-segregated α-helix, ARE strengthens electrostatic binding to lipid headgroups while orienting hydrophobic residues toward lipid tails. This configuration perturbs lipid packing, facilitates water permeation, and significantly enhances membrane cryoprotection. Overall, our work establishes a regulatory model of membrane behavior during low-temperature phase transition and provides a theoretical framework for the rational design of protective peptides.

姓名：欧莹　　单位：国家纳米科学中心　　邮箱：ouy2022@nanoctr.cn

中国科学院大学
University of Chinese Academy of Sciences

前沿交叉科学学院
School of Advanced Interdisciplinary Sciences

A Sequential Drug Delivery System Targets the Circadian Machinery to Reverse Doxorubicin Resistance in Breast Cancer

Yining Niu [a,b], Lixuan Wang [a,b], Jiayi Sun [a], Hao Wu [a], Motao Zhu [a,b,*]

a. National Center for Nanoscience and Technology of China, Beijing 100190, China
b. University of Chinese Academy of Sciences, Beijing 100049, China

引言 Introduction

Chronotherapy has garnered increasing interest in cancer treatment, yet its application in tumors with disrupted circadian rhythms has proven challenging. To address this, we developed a novel, dual-carrier hierarchically assembled delivery system (Chrono-ND-NPs) for the sequential release of the circadian modulator nobiletin (NOB) and the chemotherapeutic doxorubicin (DOX). In chemoresistant breast cancer cells, Chrono-ND-NPs restored the expression of disrupted circadian genes and significantly enhanced antitumor efficacy. These findings highlight the translational potential of our system and offer a novel strategy for precision chemotherapy.

01 研究方法 Methods

The Chrono-ND-NPs system comprises two modular components: an amphiphilic peptide assembly for encapsulating NOB, ensuring fast release, and a structurally DNA tetrahedron for encapsulating DOX and releasing it gradually through enzymatic degradation of the DNA scaffold.

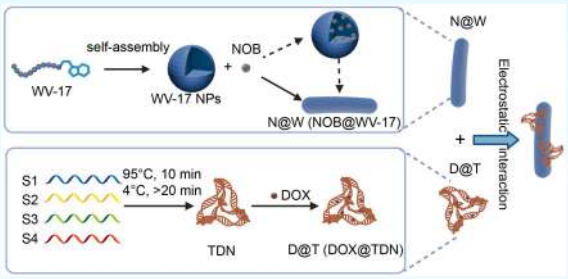

Scheme 1. Schematic illustration of the Chrono-ND-NPs delivery system.

02 研究结果 Results

Characterization of D@T, N@W, and Chrono-ND-NPs

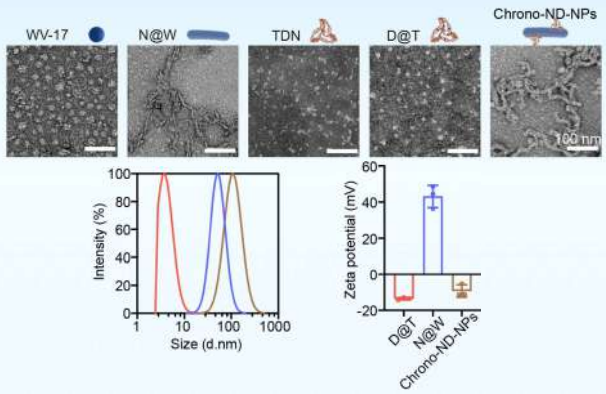

Chrono-ND-NPs restored the dysregulated circadian rhythm and inhibited tumor growth

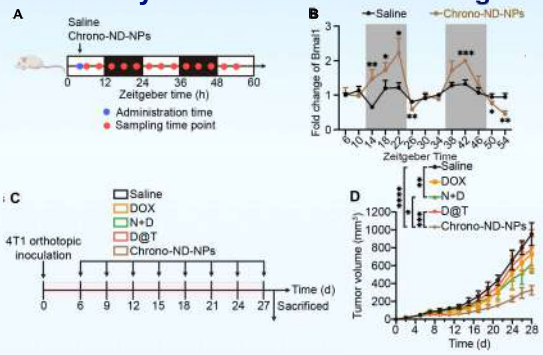

03 研究结论 Conclusion

By reprogramming the disrupted tumor circadian rhythm, chrono-ND-NPs improved chemotherapeutic efficacy, establishing a novel approach for sequential precision chemotherapy in cancer.

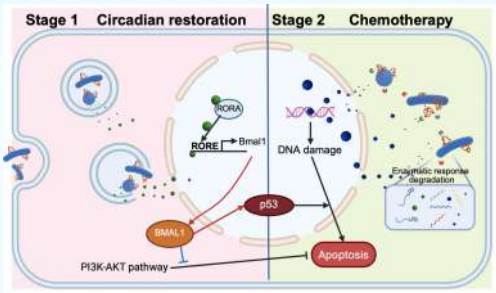

04 研究前景 Prospects

Confirming the safety and efficacy of Chrono-ND-NPs in larger animal models is essential for successful clinical translation. Adapting this platform for other circadian-modulating agents (e.g., mRNA or CRISPR-based tools) or exploring synergies with immunotherapy could further broaden its therapeutic utility.

姓名：纽一宁　　单位：国家纳米科学中心　　邮箱：niuyn2022@nanoctr.cn

中国科学院大学
University of Chinese Academy of Sciences

前沿交叉科学学院
School of Advanced Interdisciplinary Sciences

微纳塑料从肠道到肠系膜的转运和生物效应研究

刘冠宇　陈春英*
国家纳米科学中心，中国科学院大学

引言 Introduction

Micro- and nanoplastics (MNPs), as emerging environmental contaminants, exhibit poorly understood transport mechanisms in vivo. In this study, we demonstrate that orally administered polystyrene nanoparticles (PS NPs) traverse the intestinal epithelial barrier via mesenteric lacteals and accumulate at mesenteric lymphatic valves. Notably, cationic PS NPs cause significant structural damage to the valve leaflets and tight junctions, accompanied by downregulation of the mechanosensitive ion channel PIEZO1 and its downstream pathways, ultimately leading to valve dysfunction. Collectively, we identify the mesenteric lymphatic valve as a key regulatory checkpoint for cross-organ nanoparticle transport and provide the first evidence that nanoplastics can disrupt lymphatic biomechanics by impairing valve integrity.

01 研究方法 Methods

In this study, we used PS, a microplastic commonly found in everyday life, as a model material. To further explore the fate of PS MSS in C57BL/6 mice, C57BL/6 mice (6 to 7 weeks, male) were orally gavaged. Then we investigated the biological effects of PS NPs within lymphatic vessels using both stereomicroscopy and confocal microscopy.

02 研究结果 Results

Characterization of PS NPs

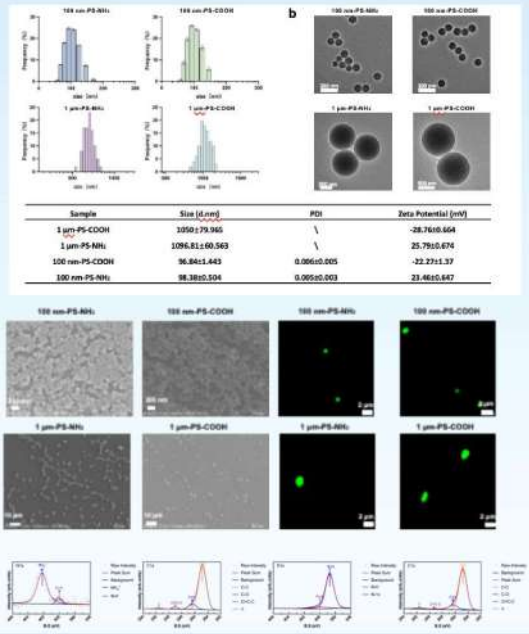

Sample	Size (d.nm)	PDI	Zeta Potential (mV)
1 μm-PS-COOH	1050±79.965	\	-28.76±0.664
1 μm-PS-NH₂	1096.81±60.563	\	25.79±0.674
100 nm-PS-COOH	96.84±1.443	0.006±0.005	-22.27±1.37
100 nm-PS-NH₂	98.38±0.504	0.005±0.003	23.46±0.647

PS crosses the intestinal barrier and accumulates at lymphatic valves.

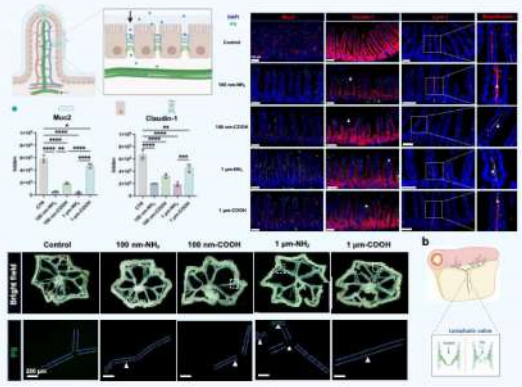

PS NPs impair mesenteric lymphatic valve function via modulation of PIEZO1 and downstream signaling proteins

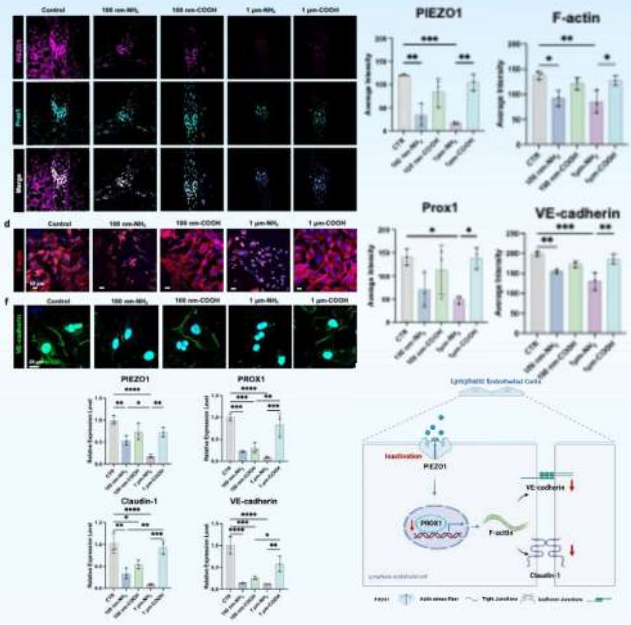

03 研究结论 Conclusion

After 5 days of high dose exposure, PS microplastics could penetrate through the mucus layer and tight junctions of the intestine into the lacteal, and induce an immune response. This study is the first to identify the mesenteric lymphatic valve as a critical checkpoint for cross-organ transport of nanoplastics, demonstrating that PS NPs exert distinct toxicological effects on lymphatic valve structures.

04 研究前景 Prospects

This study reveals the mesenteric lymphatic valve as a previously unrecognized checkpoint that governs cross-organ transport of micro- and nanoplastics, providing mechanistic evidence that cationic PS NPs disrupt valve integrity by impairing junctional architecture and downregulating mechanosensitive pathways such as PIEZO1. These findings reshape current understanding of nanoplastic biodistribution and highlight new research directions, including defining the molecular basis of lymphatic valve vulnerability, clarifying the long-term systemic consequences of lymphatic dysfunction, and establishing lymphatic-focused toxicological frameworks. Furthermore, this conceptual advance opens opportunities for developing interventions that stabilize mucosal and lymphatic structures to mitigate nanoplastic-induced injury.

姓名：刘冠宇　　单位：国家纳米科学中心　　邮箱：liugy2022@nanoctr.cn

中国科学院大学
University of Chinese Academy of Sciences

前沿交叉科学学院
School of Advanced Interdisciplinary Sciences

多肽-核酸相互作用的定量测量与作用机制探究

徐慧中，马丽露丝，王琛*，杨延莲*
中丹学院，国家纳米科学中心，中国科学院大学，北京，100190

引言 Introduction

蛋白质与核酸之间的相互识别对理解生命活动中的各个过程至关重要。我们通过流式细胞术与概率统计方法，测定了同型多肽与单链DNA（ssDNA）相互作用的平衡解离常数（K_D）及结合自由能（ΔG_A），为揭示蛋白质-核酸特异性识别机制的选择性和特异性提供了分子基础。

01 研究方法 Methods

在课题组前期的工作中，研究人员利用微球辅助流式细胞术，与Langmuir吸附模型结合，建立了检测多肽-多肽、多肽-氨基酸、糖-氨基酸等生物分子相互作用的方法。我们利用这种测量方法在多肽-核酸相互作用体系进一步检测。使用多肽偶联的聚苯乙烯微球作为固定相，不同浓度的荧光修饰ssDNA作为流动相，实验测量之后通过一系列统计方法获得多肽-ssDNA相互作用的热力学参数。

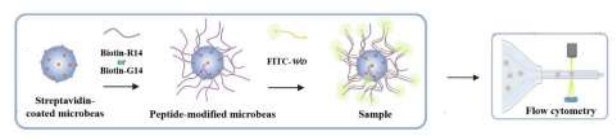

Chen, M. *et al. ChemBioChem*, **e202400891** (2024).

02 研究结果 Results

获得了精氨酸同型寡聚八肽（R8）和天冬氨酸同型寡聚八肽（D8）与25条ssDNA相互作用的结合自由能。不同带电性质的肽（D8 和 R8）的ΔG_A波动趋势相似的。在多肽-ssDNA 相互作用中存在位点效应，ΔG_A呈现阶梯式变化。突变的对称性同样改变了结合自由能。同时，在多肽-ssDNA 相互作用中存在最小片段效应。

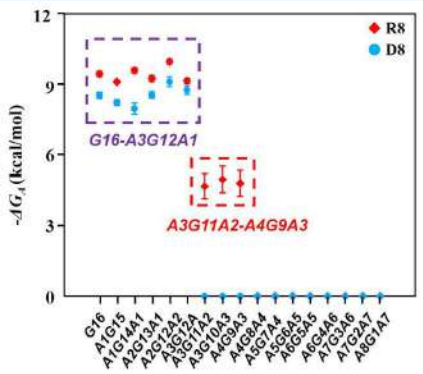

R8/D8-ssDNA的结合自由能
ΔG_A根据大小用颜色区分：绝对值大于7 kcal/mol的用紫色虚线框选，3-7 kal/mol的用红色虚线框选，低于3 kcal/mol的亲和力太弱，无法在仪器范围内检测，ΔG_A取值为0。

03 研究结论 Conclusion

通过数据及机理分析，我们主要获得了以下结论：

（1）成功开发了一种基于微球辅助流式细胞术的相互作用热力学参数定量测量的检测方法，得到多肽-ssDNA相互作用的热力学参数K_D和ΔG_A。

（2）氢键在多肽-ssDNA中发挥主导作用；

（3）静电相互作用能够影响相互作用，但不起主导作用；

（4）相互作用结合力由不同性质的分子间作用力通过协同作用促成。

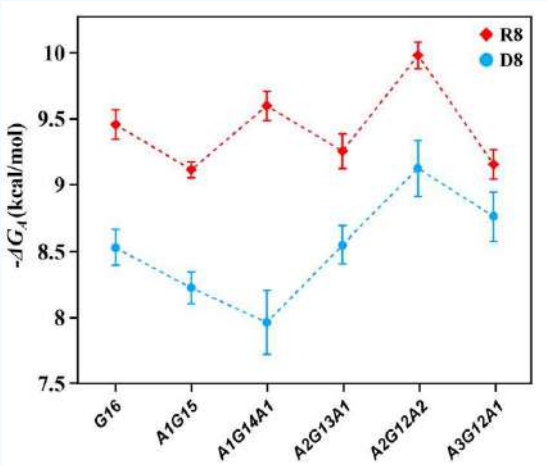

R8/D8-ssDNA的结合自由能波动
从*G16*到*A3G12A1*共6条ssDNA与多肽的结合自由能，R8组用红色表示，D8组用蓝色表示。

04 研究前景 Prospects

这项工作揭示了多肽与核酸相互作用的热力学原理，不仅将丰富我们对研究蛋白质-DNA复合物结构特征和相互作用特异性的分子基础的理解，还将为设计高特异性与亲和力的DNA结合肽提供理论基础。这些进展有望在生物传感、基因调控以及精准靶向等领域得到广泛应用。

姓名：徐慧中　　单位：中丹学院/国家纳米科学中心　　邮箱：xuhuizhong23@mails.ucas.ac.cn

中国科学院大学
University of Chinese Academy of Sciences

前沿交叉科学学院
School of Advanced Interdisciplinary Sciences

Surface structure change properties: Auto-soft bionic fibrous membrane in reducing postoperative adhesion

周伟贤，许杉杉，刘颖*
国家纳米科学中心，中国科学院大学，北京
深圳大学，深圳

引言 Introduction

Peritoneal adhesion (PA) is the most frequent complication following abdominal surgery. The PA in clinical trials has been successfully reduced by using barriers. However, the shortcomings of commercial adhesion barriers, such as rapid degradation rate of gel barrier and poor operation ability of solid barrier, remain challenges. A fibrous membrane with an ECM-like structure was fabricated. The adhesion complication were reduced significantly by regulating the surface structure. The fibrous membrane decreased inflammatory response, PA and intestinal obstruction. Fibrous membrane was flexible, showing excellent effectiveness and biocompatibility. In addition to the rat and miniature pig models, a randomized, placebo-controlled, and multicenter clinical pilot study with 150 patients confirmed that the fibrous membrane served as a favorable implant for preventing post operation PA.

01 研究方法 Methods

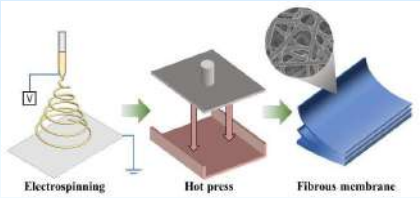

The fibrous membranes with different thicknesses (50, 60, 100, 120, 160, or 200 μm) were prepared. Two copolymers PLGA (Mw = 60,000, (D, L) LA/GA = 75/25) and PELA (Mw = 10,000, PEG-b-PLA, (D, L) LA/ EG = 50/50) were purchased from Jinan Daigang Biological Technology Co. LTD. The molecular weights were measured using standard polystyrene calibration by size exclusion chromatography (SEC) in THF (tetrahydrofuran) solvent. The mixture of PLGA and PELA was dissolved in a mixed solvent of N, N-dimethylformamide (DMF), and acetone (DMF:acetone = 5:5, volume ratio). The weight ratio of PLGA:PELA was 85:15. The total polymer concentration in the solution was 50w/v% for electrospinning and 5w/v% for casting.

02 研究结果 Results

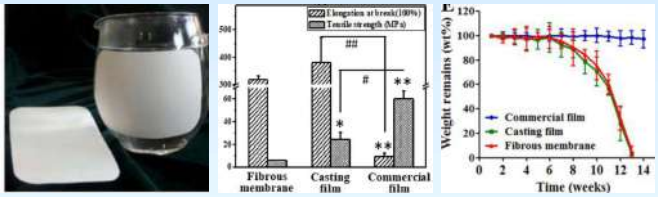

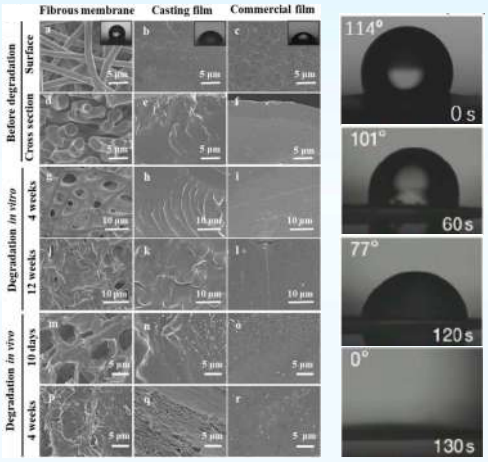

- Fibrous membrane prominent flexibility and tissue-like modulus
- ECM similar matrix and controllable biodegradability *in vivo*
- Flexibility and hygroscopicity of fibrous membrane on the wound.

02 研究结果 Results

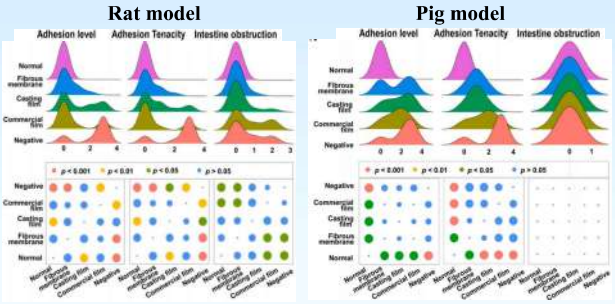

- Fibrous membrane integrated with cecum closely
- Fibrous membrane declined adhesion level and adhesion tenacity effectively.

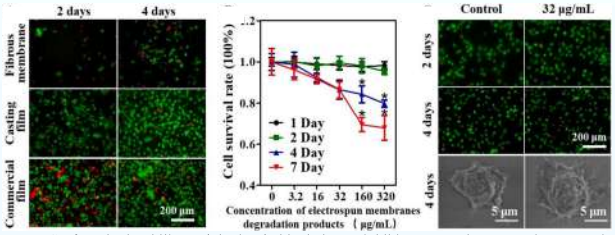

- Surface hydrophilic and hydrophobic balance inhibits macrophage attachment and accumulation
- Biocompatible fibrous membrane support cell proliferation and reduced post-operation inflammatory responses

03 研究结论 Conclusion

- ✓ Biocompatible, flexible fibrous membrane with ECM-like structure
- ✓ Fibrous membrane reduced adhesion on rat, pig and human trials
- ✓ Auto-soft, hydrophilic and hydrophobic balance modulates inflammatory microenvironment for tissue repair

04 研究前景 Prospects

- Based on the advantages of the ECM-like structure, the degradation rate, mechanical strength, and biological activity of the fibrous membrane can be further regulated, to enhance the synergistic effect of anti-adhesion and tissue repair.
- Efforts can be made to optimize large-scale production processes. After reducing costs, it can enter clinical application in hospitals at all levels and capture the market share of anti-adhesion materials.
- It can be combined with minimally invasive surgical instruments, postoperative anti-inflammatory drugs, and rehabilitation care protocols to form an integrated anti-adhesion treatment system
- The design concept of its ECM-like structure and surface regulation technology can be extended to the field of tissue engineering. It provides references for the research and development of products such as wound dressings, artificial skin, and organ repair scaffolds, expanding its multi-scenario application value in biomedical engineering.
- Based on the multicenter clinical pilot study involving 150 patients, further efforts can be made to expand the sample size for Phase III clinical trials, promoting it to become a routine anti-adhesion implant material for abdominal surgeries.

姓名：周伟贤　　单位：国家纳米科学中心　　邮箱：zhouwx2021@nanoctr.cn

中国科学院大学
University of Chinese Academy of Sciences

前沿交叉科学学院
School of Advanced Interdisciplinary Sciences

基于交联剂的抗体表位定位技术优化

李佳怡，杨雨荷*
国家纳米科学中心，中国科学院大学

引言 Introduction

Electronic microscope-based antibody epitope mapping technology is a visual proteomics method that capable of providing a comprehensive landscape of the antibody immune response. This method serves as a robust tool for comprehensively tacking the specificity and durability of these responses. However, a current challenge faced by this antibody epitope mapping technique is the potential poor quality of immune complexes caused by the additional flexibility introduced upon antibody binding. Our objective is to incorporate a chemical crosslinker into the antigen to stabilize it prior to antibody incubation, thereby improving the structural stability and overall integrity of the resulting immune complexes.

01 研究方法 Methods

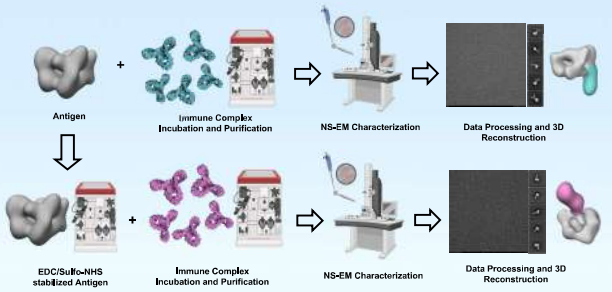

Appropriate crosslinkers and crosslinking conditions were first evaluated and selected to enable the pre-stabilization of the PLA2R. Following EDC/Sulfo-NHS–mediated crosslinking, the PLA2R antigen was co-incubated with monoclonal antibodies (mAbs). The resulting immune complexes were initially assessed by negative-stain electron microscopy (Ns-EM) and subsequently subjected to automated single-particle data acquisition using SerialEM. Multiple iterative rounds of 2D and 3D classification were then performed, ultimately yielding high-resolution three-dimensional reconstructions of the immune complexes.

02 研究结果 Results

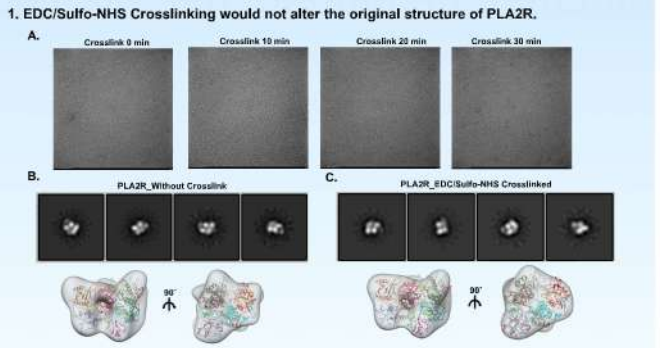

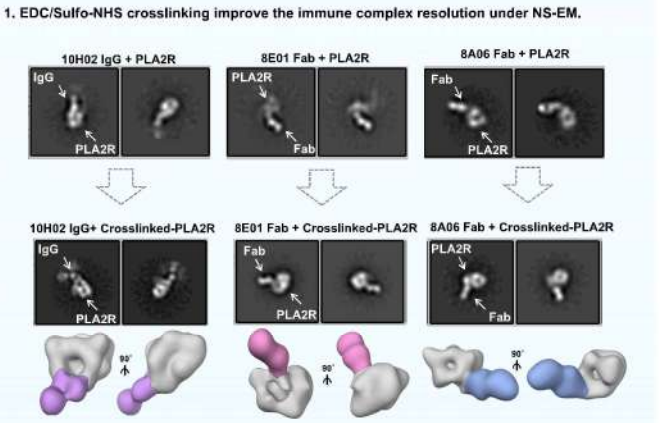

03 研究结论 Conclusion

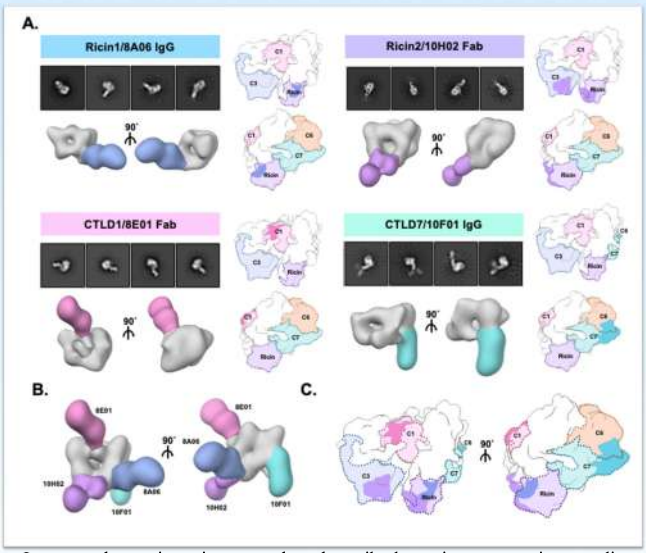

In our electronic microscope-based antibody epitope mapping studies, optimized sample preparation enabled clear two-dimensional projections and reliable three-dimensional reconstructions for antibodies targeting the Ricin2 and CTLD7 epitopes, consistent with predicted binding sites.

However, clear two-dimensional images could not be acquired for antibodies recognizing the Ricin1 and CTLD1 epitopes. Further inspection revealed that their corresponding immune complexes exhibited blurred and loosely organized morphological features. These observations suggested that binding of the Ricin1- and CTLD1-specific antibodies may disrupt the intrinsic structural stability of the PLA2R antigen, thereby inducing partial conformational heterogeneity.

To address this, we implemented a pre-stabilization strategy using the acidic crosslinker EDC. Empirically determined crosslinking parameters preserved the native morphology of PLA2R while substantially improving the clarity of immune-complex projections after antibody incubation, thereby enabling successful 3D reconstruction. These results support the hypothesis of antibody-induced conformational changes and demonstrate the effectiveness of crosslink-mediated antigen stabilization.

Collectively, representative epitope information has now been obtained for all five monoclonal antibody classes, and their approximate binding regions have been delineated. Notably, the Ricin2 epitope aligns closely with previously reported high-probability binding sites, reinforcing the reliability of our structural analyses.

04 研究前景 Prospects

This crosslinker based electron microscope-based antibody epitope mapping technology established here offers a broadly applicable strategy for improving structural reconstructions in systems limited by antigen flexibility or instability. By enhancing complex integrity and image quality, this method has the potential to benefit a wide range of epitope-mapping and structural immunology studies.

Moreover, this work provides the first structural information of four distinct immunological epitopes on the PLA2R antigen. These structural insights not only deepen our understanding of PLA2R immunogenicity but also furnish a valuable framework for future therapeutic development, like targeted antibody design and improved diagnostic strategies.

姓名：李佳怡　　单位：国家纳米科学中心　　邮箱：lijy2023@nanoctr.cn

中国科学院大学
University of Chinese Academy of Sciences

前沿交叉科学学院
School of Advanced Interdisciplinary Sciences

Research on Freeze-Assembly Nanodrugs Targeting α1-Receptors for Inhibiting Bone Metastasis of Prostate Cancer

Huiru Yang, Tianjiao Ji*
National Center for Nanoscience and Technology, University of Chinese Academy of Sciences, Beijing, China, 100190

引言 Introduction

Prostate cancer bone metastasis causes severe skeletal complications and pain, yet effective treatments that simultaneously suppress tumors, preserve bone, and relieve pain are lacking. Repurposing the α1-antagonist prazosin (PRZ) offers promise, as it demonstrates tumor-selective cytotoxicity, immunomodulation, and analgesia. However, its clinical translation is limited by poor solubility and pharmacokinetics. To overcome these challenges, we developed prazosin-loaded nanoparticles (PRZ NPs) using an innovative **freeze-assembly** method. This study aims to evaluate whether PRZ NPs can achieve coordinated tumor inhibition, bone protection, and pain relief via localized drug delivery and microenvironment remodeling.

01 研究方法 Methods

1. **Cell Experiments**

Cell Lines: RM-1、Hepa1-6、Pan02、LLC、4T1、KPC

Assays:

- CCK-8 assay: Detect PRZ's anti-proliferative activity (IC50 calculation)
- Flow cytometry: Analyze cell apoptosis rate
- Western Blot: Detect apoptotic proteins (Bcl-2, Bax)

2. Preparation and Characterization of PRZ NPs

Synthesis: Freeze-assembly (vs. traditional nanoprecipitation as control)

Process: PRZ + DSPE-PEG 2k dissolved in $CHCl_3$ → mixed with H2O → liquid nitrogen freezing → grinder milling → PRZ NPs

Formulation Optimization:

Variables: Organic/aqueous phase ratio, PRZ:DSPE-PEG 2k ratio, drug concentration

Characterization:

- DLS: Particle size, PDI, zeta potential
- TEM: Morphology and dispersibility
- Lyophilization-redissolution test: Stability verification

3. In Vivo Experiments

Animal Model: Mouse model of PCa bone metastasis (intra-tibial inoculation of RM-1 cells)

Detection Methods:

- Bioluminescence imaging: Monitor tumor progression
- Micro-CT: Evaluate bone destruction
- Behavioral tests: Assess analgesic effect (pain score recording)
- WB/IF/Sequencing: Explore immunomodulatory mechanisms (PD-L1, JAK/STAT pathway, CD8+ T cells)

02 研究结果 Results

1. Specific Anti-Tumor Activity of PRZ

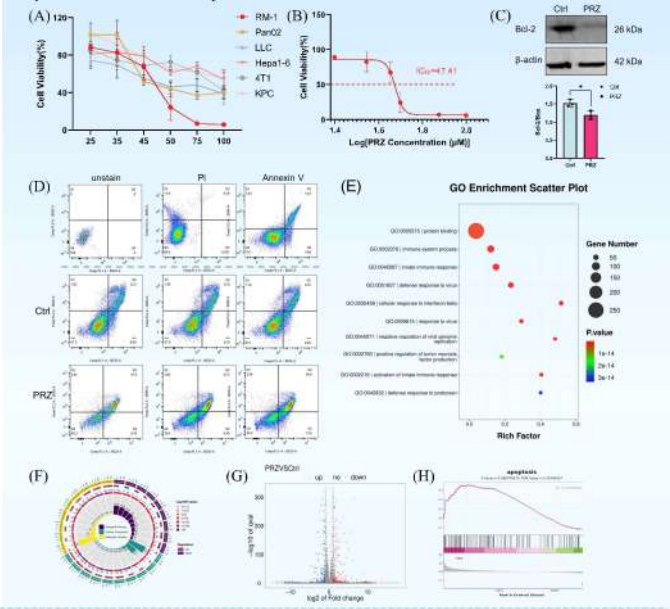

2. Preparation and Characterization of PRZ NPs

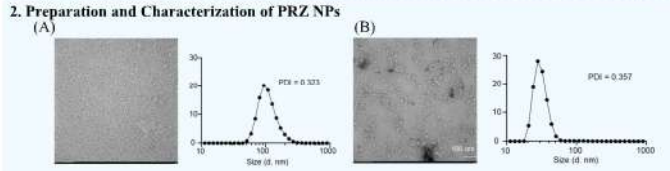

3. In Vivo Synergistic Effects

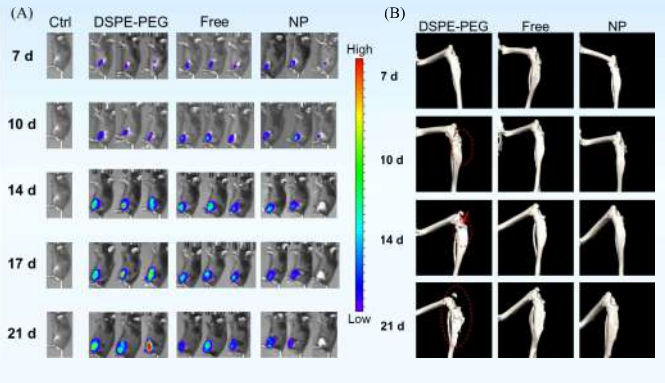

03 研究结论 Conclusion

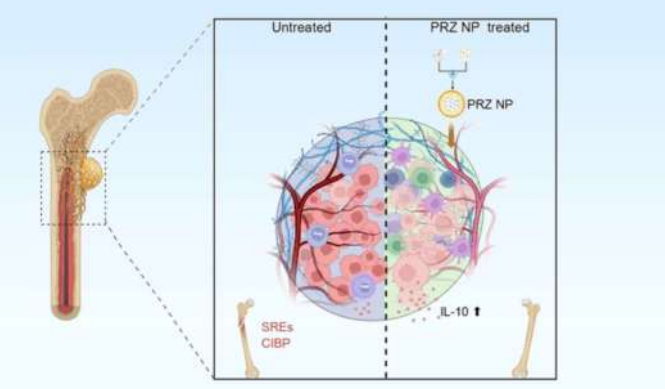

1. PRZ exhibits specific killing activity against prostate cancer cells and induces apoptosis by regulating Bcl-2/Bax.
2. Freeze-assembled PRZ NPs have uniform size, good stability, and efficient drug loading.
3. In vivo, PRZ NPs achieve triple effects: inhibiting tumor growth, protecting bone from destruction, and relieving CIBP.
4. PRZ NPs remodel the immunosuppressive microenvironment via upregulating PD-L1 and promoting CD8+ T cell infiltration.

04 研究前景 Prospects

1. Mechanism Deepening:

Clarify the synergistic relationship between PD-L1-mediated analgesia and immune remodeling; verify the regulatory role of the JAK/STAT pathway.

2. Formulation Optimization

Improve pharmacokinetic (PK) properties and tissue distribution of PRZ NPs; conduct safety evaluations (blood routine, liver/kidney function, organ pathology).

3. Combined Therapy

Explore combinations of PRZ NPs with immune checkpoint inhibitors or chemotherapeutics to enhance therapeutic efficacy.

4. Clinical Translation

Promote the clinical translation of "old drug repurposing" (PRZ) to provide a safe and effective novel strategy for patients with advanced PCa bone metastasis.

姓名：阳卉茹　　单位：国家纳米科学中心　　邮箱：yanghr2023@nanoctr.cn

中国科学院大学
University of Chinese Academy of Sciences

前沿交叉科学学院
School of Advanced Interdisciplinary Sciences

调节脂肪组织胶原交联辅助干预脂肪性肝病的研究

韩渊越，赵颖*
国家纳米科学中心，中国科学院大学，北京，100190

引言 Introduction

代谢功能障碍相关脂肪性肝病（MASLD）目前全球流行率超过30%，我国MASLD发病率也在逐年增加，已成为严重的公共卫生问题。目前缺乏针对疾病源头的有效干预策略，现有药物多存在肝外副作用或疗效局限。本研究聚焦于脂肪组织功能障碍在MASLD发生发展中的核心驱动作用。在肥胖状态下，脂肪组织发生细胞外基质（ECM）重塑，其中晚期糖基化终末产物（AGEs）介导的胶原交联是关键环节。它不仅导致组织纤维化、僵硬，物理限制脂肪细胞正常扩张，还通过AGEs-RAGE信号通路持续引发炎症，共同导致脂肪组织储脂功能受损。这引发脂质“溢出”，过量游离脂肪酸涌入肝脏，是驱动肝脏脂质过度堆积和后续损伤的源头。基于此，我们提出科学假设：靶向干预脂肪组织中的AGEs胶原交联，有望恢复其正常功能，从而从源头上缓解肝脏的脂质输入。为验证此假设，本研究设计并构建了靶向脂肪细胞的载药脂质体纳米颗粒（ALT@PTP-LNPs），旨在特异性递送AGEs交联抑制剂至脂肪组织，探索其通过缓解脂肪组织纤维化与炎症，进而改善肝脏脂质代谢紊乱的治疗潜力，为MASLD的治疗提供新策略。

01 研究方法 Methods

我们对来自黄骅市人民医院的正常人和MASLD患者的大网膜脂肪组织进行了分析，通过样本的HE、天狼星红和AGEs免疫荧光染色，初步验证了MASLD患者脂肪组织中存在纤维化与AGEs异常积累。并用高糖高脂饮食饲喂小鼠建立MASLD动物模型，分析统计小鼠脂肪性肝病进展情况和脂肪组织状态。此外我们设计了一个脂肪组织归巢肽PTP修饰的脂质体纳米颗粒，并完成了其基本理化性质表征。

02 研究结果 Results

对MASLD患者的临床脂肪组织样本分析发现，其内脏脂肪中出现纤维化以及AGEs的荧光信号强度显著高于正常组织，这初步证实了AGEs交联在MASLD患者脂肪组织中的异常积累。

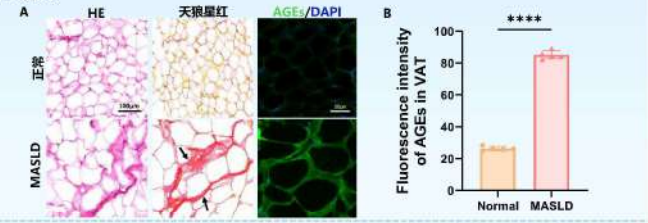

A. 正常人和MASLD患者脂肪组织切片染色对比；B. 内脏脂肪AGEs荧光信号强度统计

通过高糖高脂饮食喂养，我们成功建立了小鼠MASLD模型。模型小鼠表现出典型的疾病特征，包括体重显著增加并出现血脂异常，胰岛素抵抗，肝脏达到轻度脂肪变性，内脏脂肪组织出现纤维化和AGEs沉积。

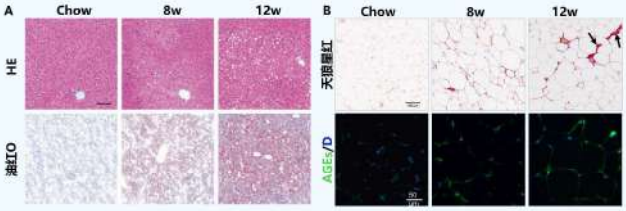

A. 正常饮食小鼠和MASLD模型小鼠肝脏切片HE、油红染色对比；B. 正常饮食小鼠和MASLD模型小鼠脂肪组织切片天狼星红染色和AGEs荧光染色对比

我们成功合成了靶向脂肪细胞的载药脂质体纳米颗粒ALT@PTP-LNPs，并对其进行了初步表征，平均粒径约为200nm，PDI为0.078。

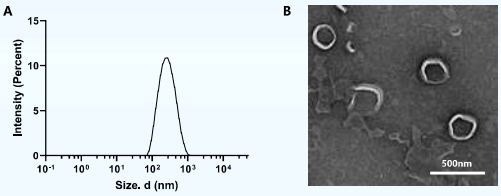

A. ALT@PTP-LNPs的纳米粒度仪表征结果；B. 乙酸氧铀负染纳米颗粒的透射电镜扫描结果

03 研究结论 Conclusion

在收集到的临床样本中我们观察到明显的AGEs积累和胶原沉积，且小鼠MASLD模型与临床分析结果相对应。在小鼠MASLD模型中，8周时已达到轻度肝脂肪变性，脂肪细胞面积与正常鼠相比明显增大；8-12周肝脏脂质积累进一步增加，处于轻度向中度脂肪变性过渡阶段，脂肪细胞面积无显著变化，说明脂质从脂肪组织向肝脏“溢出”，与血脂升高相对应。脂肪组织发生纤维化，限制了脂肪细胞的正常扩张和储脂能力。此外通过检测口服葡萄糖2小时内血糖变化，我们观察到模型组小鼠出现胰岛素抵抗症状，提示模型组小鼠代谢受损。

我们合成的脂质体纳米颗粒平均粒径约200nm，分散较为均一，脂肪组织毛细血管的直径为2~5μm，纳米颗粒可以通过血管递送到脂肪组织，具备进行后续实验的基础。

04 研究前景 Prospects

该研究将MASLD的干预靶点从肝脏本身前移至脂肪组织，有望开发一种针对MASLD源头的新型疗法，在MASLD发展早期对疾病进行及时干预，以避免不可逆的肝损伤。

姓名：韩渊越　　单位：国家纳米科学中心　　邮箱：hanyy2023@nanoctr.cn

中国科学院大学
University of Chinese Academy of Sciences

前沿交叉科学学院
School of Advanced Interdisciplinary Sciences

中国科学院大学2025年研究生学术论坛前沿交叉科学分论坛

Hydrochar Mitigates Saturated LCFA Inhibition and Enhances DIET-Mediated Methane production

Muhammad Abrar, Shanfei Fu, Rongbo Guo*

Qingdao Institute of Bioenergy and Bioprocess Technology, Chinese Academy of Sciences

*Corresponding author: guorb@qibebt.ac.cn

引言 Introduction

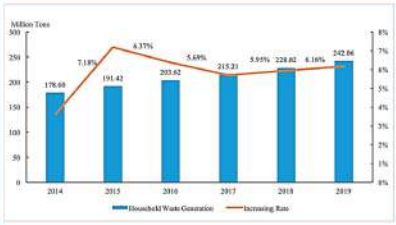

Fig. 1. China's Escalating Household Waste generation, 2014–2019 with annual growth rates averaging **6.2%** and peaking at **7.18%** in 2019.

- Rapid economic growth in Asia and especially in China, will lead to a huge increase of food waste production that is expected to increase by **278–416 million tones** [1].
- Among various waste management practices, anaerobic digestion **(AD)** is a useful method to transform food waste into biofuel and bio-fertilizer.

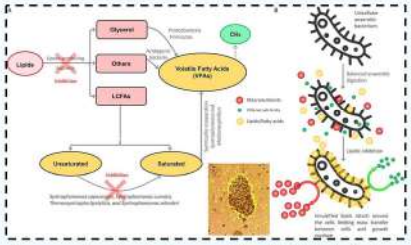

- Long-chain fatty acids (LCFAs) from lipid-rich waste cause severe mass transfer inhibition in AD, reducing methane yields by 40-60% through cell membrane disruption and pH collapse.
- Lipid waste provide **70% more energy potential** per kg. if inhibition can be overcome [2].
- **Aim:** Employ cotton stalk hydrochar to mitigate saturated LCFA inhibition and enhance methane production through DIET enhancement.

03 Conclusion (研究结论)

- **Hydrochar treatment:** 12.2% ↑ methane, 21% ↓ lag phase, pH buffering + DIET enhancement **Scalable solution**: Cotton stalk waste → valuable bioaugmentation tool

04 Prospects (研究前景)

- Scale-up to continuous reactors
- Techno-economic analysis
- Application to other inhibitory compounds (ammonia, sulfide)

01 研究方法 Methods

Hydrochar production from Cotton Stalk

Hydrochar mediated methane, VFA, pH, and gene expression

02 研究结果 Results

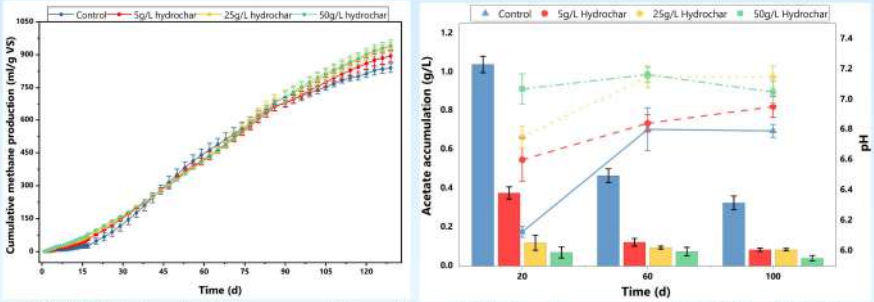

Figure 2. (a) Effect of hydrochar on cumulative methane yield. Error bars represent ±1 SD (n=3).. Control: 839±14 mL/g VS; 5 g/L HC: 894±14 mL/g VS; 25 g/L HC: 937±16 mL/g VS; 50 g/L HC: 942±14 mL/g VS (highest yield).
(b) Figure 2. Acetate concentration (bars) and pH (lines) during LCFA degradation. Hydrochar prevented initial pH drop to 6.0 (control) and maintained optimal range (6.6–7.2) for acetoclastic methanogens.

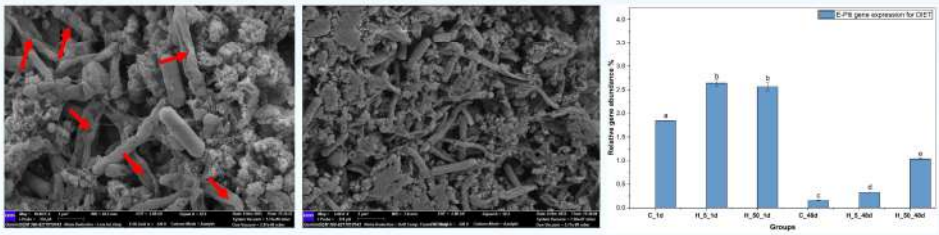

Figure 3 (a). Microbial cells in control reactor showing LCFA-induced membrane disruption (red arrows). **(b)** Dense biofilm formation on hydrochar surface with intact cell morphology. **(c)** Temporal enrichment of e-pili genes in 50 g/L hydrochar reactor vs. control. Initial phase: **1.4-fold upregulation**; Mid-phase: **6.6-fold upregulation** (padj=0.003). Error bars: ±1 SE.

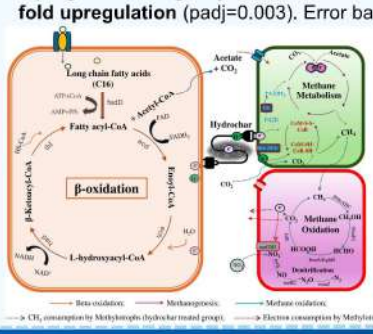

DIET Bypass: Hydrochar's conductive surface (C/H=10.71) enables direct electron transfer
e-pili Amplification: **6.6-fold upregulation** accelerates syntrophic β-oxidation-methanogenesis coupling.
Metabolic Rerouting: ***Methanoculleus/Methanothrix*** **ratio** favoring LCFA-tolerant hydrogenotrophic archaea.
pH Buffering: Hydrochar maintains **pH 6.6–7.2** vs. control drop to 6.0.
Transient Sink: Methylomonas oxidizes slight portion of **CH_4** in mid-phase, but DIET enrichment compensates by **+12.2% net yield**.

邮箱：abrarrao822@mails.ucas.ac.cn
单位：中国科学院青岛生物能源与过程研究所

References:
1. Negri et al., 2020. *Renew Sust Energy Rev* 133:110138.
2. Sun et al., 2022. *Appl Environ Microbiol* 88:e0104222.

中国科学院大学
University of Chinese Academy of Sciences

前沿交叉科学学院
School of Advanced Interdisciplinary Sciences

面向非正态过程的监控新方案：基于似然比检验的瑞利分布控制图

贾通通[1,2], 王金洋[1], 张久军[1]

1 辽宁大学数学与统计学院，
2 中国科学院大学杭州高等研究院

引言 Introduction

控制图作为统计过程监控（SPM）核心工具，可实时预警异常、量化过程稳定性、支撑工艺改进，是工业质量管控关键；但现有方案多基于正态假设，对瑞利分布等非正态过程适配性差、易误漏报，且瑞利分布专用监控方案少、小偏移灵敏度不足，而生物制造中发酵菌体浓度、产物纯度等关键参数常呈非正态，传统方案难以适配，本研究构建的基于似然比检验（LRT）的瑞利分布新控制方案，因适配非正态、提升了小偏移灵敏度，有望为该领域非正态参数监控提供新选择。

01 研究方法 Methods

- 基础理论：瑞利分布（如图1）

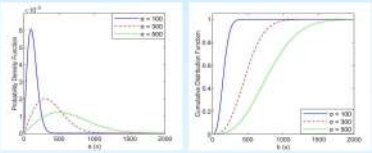

图 1. 瑞利分布的 PDF 和 CDF

概率密度函数： $f(x)=\frac{x}{\sigma^2}e^{-\frac{x^2}{2\sigma^2}}\quad(x>0,\sigma>0)$

- 核心创新

假设检验： $H_0:\sigma=\sigma_0\quad H_1:\sigma=\sigma_1$

构建统计量：基于对数似然比，并引入EWMA平滑机制，增强对小漂移的敏感性。

$$\ln LR_t=n\left[\left(\frac{\hat{\sigma}_t^2}{\sigma_0^2}-1\right)-\ln\left(\frac{\hat{\sigma}_t^2}{\sigma_0^2}\right)\right]$$

$$B_t=(1-\lambda)B_{t-1}+\lambda\hat{\sigma}_t^2$$

- 三大控制方案

DELR (双边)：监测参数 σ 的双向漂移。

$$DEL_t^*=\frac{B_t}{\sigma_0^2}-\ln\frac{B_t}{\sigma_0^2}$$

UELR (上单边)：专用于监测参数 σ 的上升。

$$UEL_t^*=\frac{Z_t^+}{\sigma_0^2}-\ln\frac{Z_t^+}{\sigma_0^2},\ Z_t^+=\max\{\sigma_0^2,B_t\}$$

LELR (下单边)：专用于监测参数 σ 的下降。

$$LEL_t^*=\frac{Z_t^-}{\sigma_0^2}-\ln\frac{Z_t^-}{\sigma_0^2},\ Z_t^-=\min\{\sigma_0^2,B_t\}$$

- 控制限确定：

采用数值模拟法，设定常见样本量 (n=3,5,10)、平滑参数 (λ=0.05,0.1,0.2)与目标平均运行长度（ARL_0=370,500），通过 10000 次模拟迭代确定各方案控制限（如表1）。

表 1 控制方案的控制限

控制方案	n	ARL=370			ARL=500		
		λ			λ		
		0.05	0.10	0.20	0.05	0.10	0.20
DELR 方案	3	1.02626	1.06328	1.14917	1.02898	1.06880	1.16014
	5	1.01582	1.03823	1.09007	1.01746	1.04146	1.09665
	10	1.00793	1.01915	1.04527	1.00875	1.02077	1.04855
UELR 方案	3	1.01973	1.05219	1.12992	1.02281	1.05777	1.14251
	5	1.01188	1.03102	1.07756	1.01364	1.03457	1.08515
	10	1.00588	1.01547	1.03860	1.00681	1.01727	1.04221
LELR 方案	3	1.01891	1.04803	1.11539	1.02165	1.05312	1.12531
	5	1.01158	1.02915	1.07086	1.01310	1.03251	1.07680
	10	1.00577	1.01486	1.03610	1.00660	1.01649	1.03924

02 研究结果 Results

- 模拟实验验证：当参数无偏移δ=1时，DELR、UELR、LELR 的 ARL值均接近预设的ARL_0，运行稳定；样本量越大，监控效率与稳定性越优（如 n=10 时，参数偏移 δ = 0.8，DELR 的 ARL 较 n=3 缩短约 50%）；平滑参数 λ =0.05 对小偏移更敏感，λ=0.2 对中等偏移响应更迅速。
- 与现有方案对比：DELR 监控参数减小时，ARL 显著低于现有 REWMA 方案（如n=5 λ =0.2 ARL_0 = 370 δ=0.9 时，DELR 的 ARL 为 52.31，REWMA 为 65.04），监控优势明显；UELR、LELR 监控对应单边偏移时，ARL 均低于基于威布尔分布的 CUSUM 方案（如 n=5 λ =0.1 ARL_0 = 370 δ=1.05，UELR 的 ARL 为 67.65，CUSUM 为 75.96），灵敏度更高。
- 实证验证：以玻璃纤维强度数据（经检验符合瑞利分布）为例。

DELR可准确识别参数 0.7 倍（减小）与 1.35 倍（增大）偏移，且无偏移时统计量波动更接近目标值，如图2；UELR、LELR 分别精准捕捉参数 1.3倍增大、0.7 倍减小偏移，验证了方案实用性，如图3、图4。

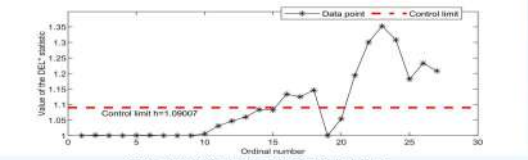

图 2. 玻璃纤维强度数据的 DELR 控制方案

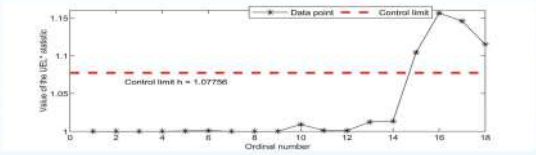

图 3. 玻璃纤维强度数据的 UELR 控制方案

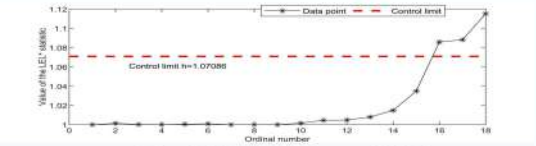

图 4. 玻璃纤维强度数据的 LELR 控制方案

03 研究结论 Conclusion

- 本研究提出的 DELR、UELR、LELR 三类控制方案，可有效监控瑞利分布过程尺度参数偏移，解决了现有方案对非正态过程监控效果差的问题。
- 三类方案各具优势：DELR 适用于需全面监控参数双向偏移的场景，UELR、LELR 分别适配仅关注参数增大、减小的单边监控需求，灵活性高。
- 方案设计原理简洁、计算简便，且在非正态分布过程中表现出优异的稳定性与灵敏度，具备向多领域拓展应用的潜力。

04 研究前景 Prospects

本控制图为解决非正态过程监控问题提供了新选择，在生物制造领域具有明确的应用前景：

- 应用于生物基材料强度监控：针对微生物纤维素、生物合成纤维等材料的单丝强度与直径分布（典型右偏数据），本方案的DELR图能灵敏识别强度参数的下降漂移，LELR图可专用于此，从而在原料性能发生劣化时及时预警，有效降低高价值生物材料的批次不合格率，保障其产品均一性与可靠性。
- 应用于药物制剂粒径控制：在疫苗佐剂、脂质体纳米粒的制备过程中，其粒径分布直接影响药效与安全性。本方案的DELR与UELR/LELR图能分别对粒径的双向及单向漂移进行精准监控，为实现符合药品生产质量管理规范（GMP）的实时质量保证提供了关键技术支撑，避免因粒径失控导致的产品报废与资源浪费。
- 应用于细胞培养过程优化：在悬浮培养等工艺中，细胞团尺寸的异常变化是反映培养状态的关键指标。采用UELR或LELR图对其进行单向监控，可及时发现由于营养或剪切力异常导致的尺寸增大或减小趋势，从而指导生物反应器的精准干预，提升整个产程的稳定性与最终产出。

姓名：贾通通　　单位：中国科学院大学前沿交叉科学学院　　邮箱：jiatongtong24@mails.ucas.ac.cn

中国科学院大学
University of Chinese Academy of Sciences

国家纳米科学中心
National Center for Nanoscience and Technology

自组装多肽调控视网膜色素上皮透过性

沈耀邦[a,b,1]，魏林霏[c,1]，徐国洋[a,b]，于伟泓[c,*]，王磊[a,b,*]

a. 中国科学院纳米科学卓越中心，中国科学院纳米材料和纳米效应生物安全重点实验室，国家纳米科学技术中心（NCNST），北京100190，中国
b. 中国科学院大学（UCAS），北京100049，中国
c. 中国医学科学院北京协和医学院，北京协和医院眼科，中国医学科学院眼底病重点实验室，北京100730，中国

引言 Introduction

- 息肉状脉络膜血管病变 (PCV) 病灶点通常发生在视网膜色素上皮 (RPE) 下导致 RPE 脱离而导致视力明显下降甚至丧失
- PCV 患者对临床一线药物抗血管内皮生长因子 (Anti-VEGF) 应答欠佳，50%-60% 的患者在规律 Anti-VEGF 治疗后任表现出持续疾病活动
- 眼底屏障组织 RPE 严格限制亲水性大分子运输表明 Anti-VEGF 对 RPE 的低渗透性极有可能是 PCV 患者对 Anti-VEGF 治疗效率低的主要原因
- 我们设计了两种自组装多肽 (CK & CS)，CK 能够短暂调控 RPE 层的紧密连接状态促使药物由细胞旁途径渗透，CS则通过转胞吞作用进行跨细胞运输，并随着药物去除后 RPE 恢复正常。

01 研究方法 Methods

I. 多肽设计与表征

II. 体内外渗透性

III. 渗透机制探究

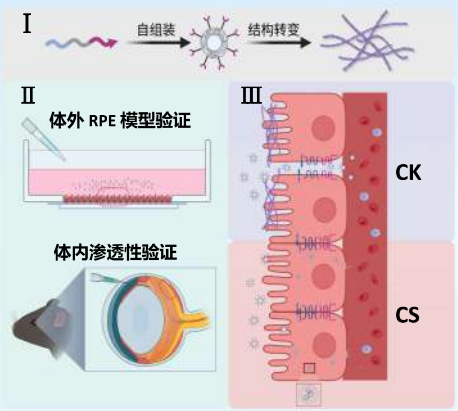

02 研究结果 Results

① 材料表征

a. 圆二色谱 (CD)　b. 透射电镜成像 (TEM)

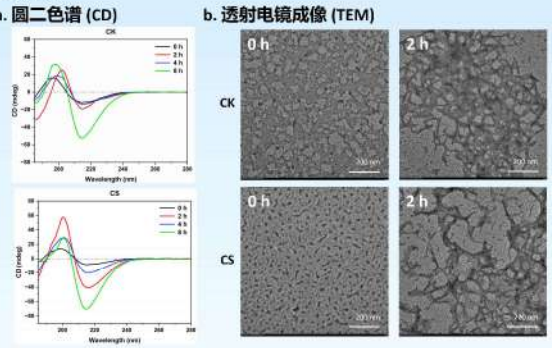

多肽自组装成以 β - 折叠 (a) 为主的纳米纤维网络 (b)

② 多肽穿透 RPE 体外模型

a. 跨上皮电阻 (TEER)　b. 免疫荧光染色

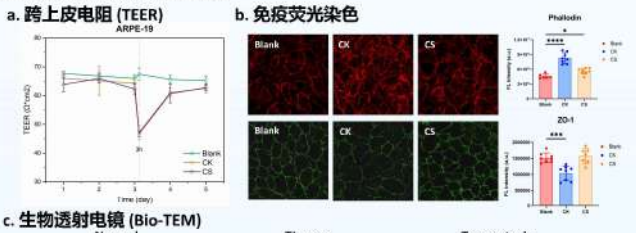

c. 生物透射电镜 (Bio-TEM)

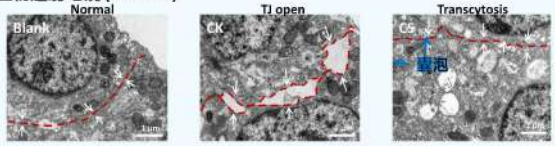

- CK高度重塑细胞骨架并下调紧密连接相关蛋白1 (ZO-1) 水平以影响RPE层紧密连接 (a, b, c)
- CS作用后促进细胞骨架上调影响 RPE 层通透性，但不影响 ZO-1 表达 (a, b)，通过转包吞运输渗透 RPE (c)

③ 多肽穿透 RPE 体内验证

a. 眼球冷冻切片

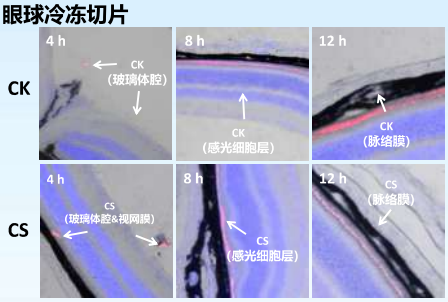

➢ 多肽 (Cy5标记) 从玻璃体腔渗透进入脉络膜

b. 脉络膜铺片免疫荧光染色

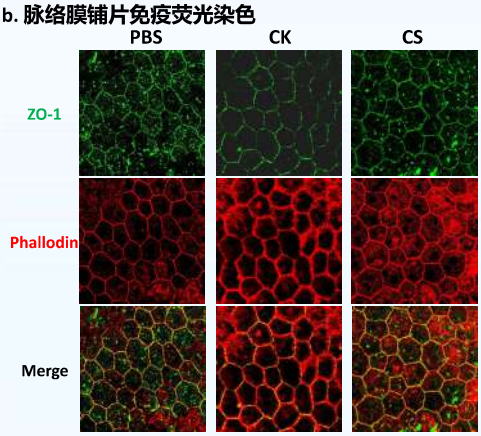

➢ CK 组 ZO-1 显示明显的不连续性且胞内的荧光信号减少，F-actin 呈现出强弥漫性

➢ CS组 ZO-1 和 F-actin 边界特征性共定位没有改变，F-actin胞内表达上调

03 研究结论 Conclusion

✓ CK 主要通过靶向 RPE 膜上受体结合形成纤维网络调控 RPE 层的紧密连接状态促进药物的细胞旁渗透途径

✓ CS 主要结合膜上受体触发受体介导的转胞吞作用进行跨细胞转运

04 研究前景 Prospects

本研究开发了两种创新性针对视网膜色素上皮 (RPE) 具有不同渗透机制的自组装多肽，为解决屏障药物渗透性难的临床问题提供了新思路，并为提高 PCV 患者临床疗效问题以及病理性黄斑区新生血管提供了新的临床治疗策略

References
[1] Yao-Bang Shen, Guo-Yang Xu, Jia-Qi Feng, Xiang-Dan Li, Ai-Qing Zhang, Lei Wang. *Journal of Molecular Science*, 2024, 40 (6): 528-539.
[2] Kuo Zhang, Hui Zhang, Yong-Hong Gao, Jia-Qi Wang, Yuan Li, Hui Cao, Ying Hu, and Lei Wang. *ACS Nano*, 2021, 15 (8), 13065-13076

姓名：沈耀邦　单位：国家纳米科学中心　邮箱：shenyb2023@nanoctr.cn

中国科学院大学
University of Chinese Academy of Sciences

前沿交叉科学学院
School of Advanced Interdisciplinary Sciences

生物活性水凝胶治疗糖尿病外周动脉疾病

孙慧珍，师晓丽*，韩东*

国家纳米科学中心，中国科学院大学，北京，100190

引言

- 下肢外周动脉疾病（PAD）的病理机制复杂，传统上认为是一个由内膜损伤启动、中膜平滑肌细胞（VSMC）增殖迁移导致管腔狭窄的“由内而外”的过程。然而，近年来的研究逐渐揭示了血管外膜在PAD发病中的始动和调控作用，提出了“由外而内”的新视角。
- 水凝胶本身及其携带的药物成分构成一个抗炎的血管外微环境，而ADSCs则作为多种修复性细胞因子（如血管内皮生长因子、抗炎因子）的活体工厂，协同作用以对抗病理刺激。

01 研究方法 Methods

薄膜分散法制备磷脂复合物

羧基与Ca^{2+}成键构成复合水凝胶

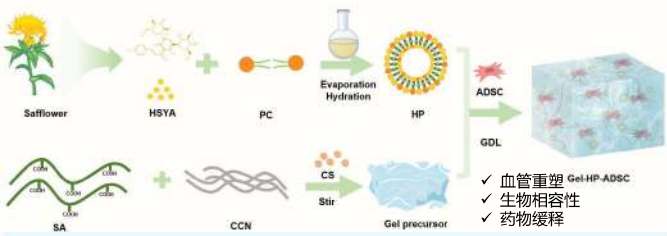

02 研究结果 Results

1.HP是均匀球形纳米颗粒

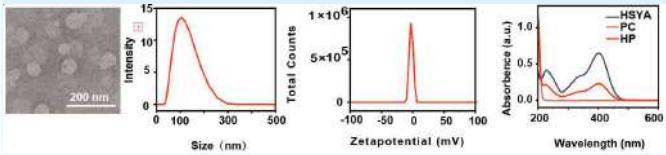

2.Gel-HP孔径大小适合干细胞生存

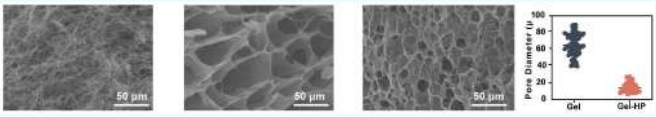

3. Gel-HP具备可注射性以及良好的溶胀性能

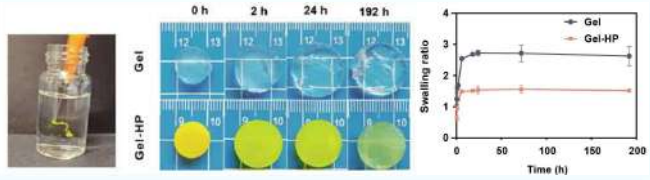

4. ADSCs在Gel-HP三维培养减慢其迁移能力

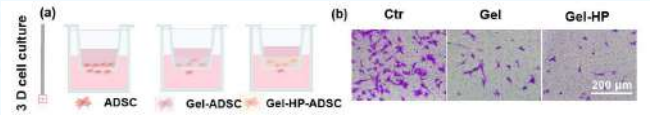

5. Gel-HP三维培养不影响ADSCs成脂分化

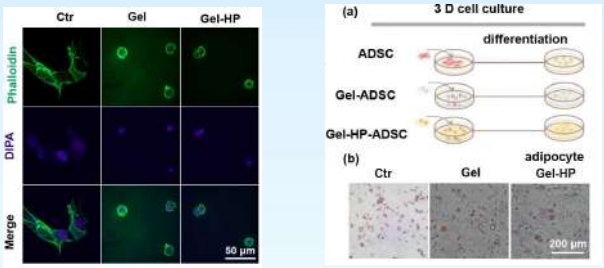

6. Gel-HP-ADSC有效改善血管病变

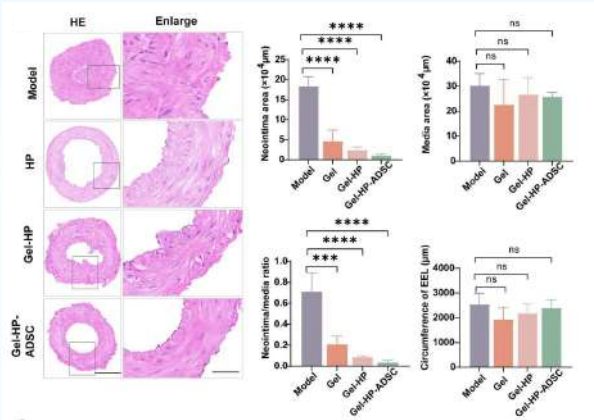

03 研究结论 Conclusion

Gel-HP-ADSC作为仿PVAT复合水凝胶通过模拟其血管周围微环境，调控血管重塑过程而非单纯的血管生成，同时展现出良好的免疫调节功能，为下肢动脉病变的治疗提供了新的策略。

04 研究前景 Prospects

Gel-HP-ADSC体系本身作为一个可编程的通用平台，具有巨大的拓展性。该平台不仅限于HSYA，理论上可以负载其他不同机制的药物（如抗增殖药物、他汀类药物），与ADSCs协同，用于治疗动脉粥样硬化、血管再狭窄等不同血管疾病。

姓名：孙慧珍　　单位：国家纳米科学中心　　邮箱：sun18338975621@163.com

Shuhui Zhang1,2, Tianjiao Ji1,2*, Guangjun Nie1,2*
1 CAS Key Laboratory for Biomedical Effects of Nanomaterials and Nanosafety, CAS Center of Excellence in Nanoscience, National Center for Nanoscience and Technology, Beijing, China
2 School of Nanoscience and Engineering, University of Chinese Academy of Sciences, Beijing, China

中国科学院大学
University of Chinese Academy of Sciences

前沿交叉科学学院
School of Advanced Interdisciplinary Sciences

Nanoformulated Oxaliplatin Reduces Platinum Accumulation in Dermal Fibroblasts to Alleviate Cold Allodynia

Shuhui Zhang, Tianjiao Ji*, Guangjun Nie*
CAS Key Laboratory for Biomedical Effects of Nanomaterials and Nanosafety, National Center for Nanoscience and Technology, Beijing, China, 100190

引言 Introduction

Oxaliplatin (OXA), a first-line chemotherapeutic for colorectal cancer, induces severe peripheral neuropathy in most patients, with cold allodynia as a hallmark symptom. While neurotoxicity mechanisms have been studied, the complete pathophysiology remains unclear. This study reveals that OXA-induced cold allodynia is not solely mediated by direct neural accumulation. Compared to free OXA, liposomal and PEG-PLGA nanoformulations significantly reduced cold hypersensitivity, despite comparable platinum levels in neural tissues. Laser ablation ICP-MS imaging showed substantial dermal fibroblast platinum accumulation with free OXA, but not with nanoformulations. Mechanistically, dermal OXA accumulation activated the NF-κB pathway in ECM-associated fibroblasts, upregulating CCL2 expression. This subsequently activated the CCL2/CCR2/TRPM8 axis, increasing pain sensitivity. These findings elucidate a novel peripheral mechanism for OXA-induced neuropathy through dermal fibroblasts and underscore the potential of nanoformulations in mitigating this dose-limiting side effect.

01 研究方法 Methods

Preparation and Characterization of Nanoformulations

Liposomal oxaliplatin (Lip-OXA) was prepared via a thin-film hydration method using DOPC, cholesterol, and DSPE-PEG2000 (15:5:1 mass ratio). The lipid film was hydrated with an OXA/glucose solution, and unencapsulated drug was removed by dialysis. Poly(lactic-co-glycolic) acid nanoparticles (PLGA-OXA) were synthesized using a W/O/W double emulsion technique with mPEG-PLGA and polyvinyl alcohol (PVA).

In Vivo Efficacy and Mechanism Studies

Tissue platinum content was quantified by ICP-MS following acid digestion. Cold allodynia was assessed in mice after intravenous administration of formulations (4 mg/kg OXA) by measuring paw withdrawal latency on a cold plate. Spatial platinum distribution in skin was mapped using LA-ICP-TOF MS. Single-cell RNA sequencing was performed on skin cell suspensions using the 10x Genomics platform, with subsequent clustering and t-SNE visualization.

Anti-Tumor Efficacy

MC38-Luc cells were maintained under antibiotic selection (G418/puromycin). For in vivo evaluation, an orthotopic colorectal cancer model was established in C57BL/6 mice by surgically suturing MC38 tumor fragments onto the cecum. Five days post-implantation, mice were randomized into four treatment groups (5% Glucose, Free OXA, Lip-OXA, and Liposome) and administered intravenous injections every three days for a total of five doses (4 mg OXA/kg).

02 研究结果 Results

Lip-OXA alleviated the cold allodynia in mice through reducing platinum accumulation in the skin

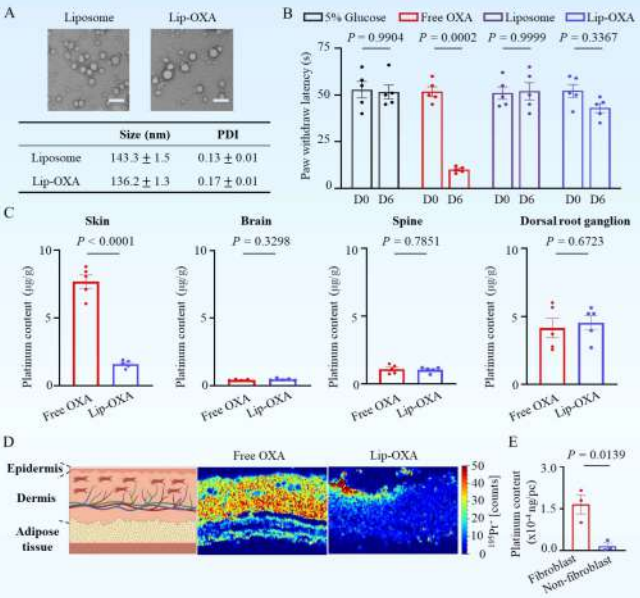

Lip-OXA attenuated the platinum accumulation-mediated CCL2 overexpression in dermal fibroblasts

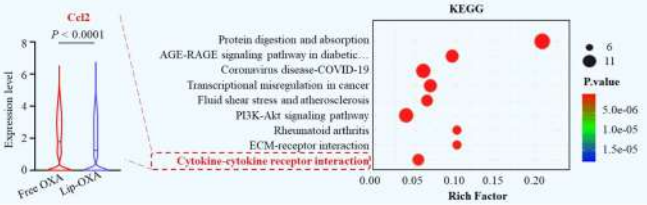

ECM-associated fibroblasts regulate CCL2 secretion through the NF-κB signaling pathway

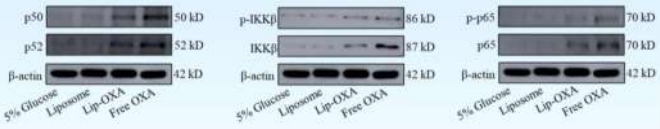

Lip-OXA enhanced the therapeutic efficacy of in situ CRC mice model with decreased cold allodynia

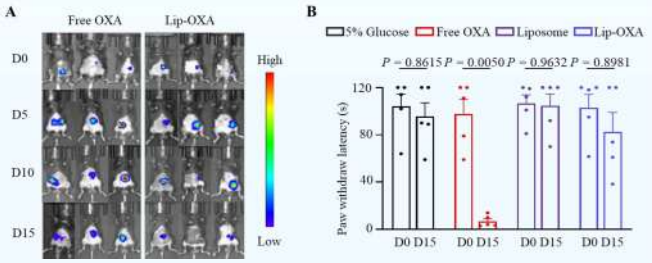

03 研究结论 Conclusion

In summary, we interpreted a mechanism that OXA induced cold allodynia was mediated by Fibro_ECM. Platinum accumulation activated NF-κB pathway in Fibro_ECM to initiate CCL2/CCR2/TRPM8 axis connecting the fibroblasts and nerves to accelerate cold allodynia. This discovery originated from comparing platinum accumulation of Lip-OXA and OXA, since Lip-OXA significantly alleviated chemotherapy-induced cold allodynia in mice compared to free OXA. Notably, the pain-relieving effect was achieved without compromising therapeutic outcomes, as evidenced by the potent antitumor performance of Lip-OXA in the in situ CRC model. These findings not only elucidate a fibroblast-nerve communication through the CCL2/CCR2/TRPM8 axis as a key mediator of OXA-induced neuropathy but also highlight the potential of nanoformulations to decouple toxicity from efficacy by modulating drug biodistribution/accumulation.

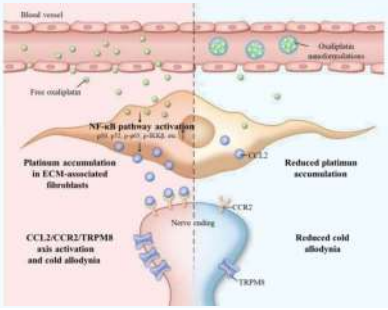

04 研究前景 Prospects

- **Novel Mechanism Elucidation:** This study reveals a previously unrecognized indirect pathway—the dermal fibroblast-mediated CCL2/CCR2/TRPM8 axis—for oxaliplatin (OXA)-induced cold allodynia, shifting focus beyond direct neurotoxicity and opening new avenues for mechanistic research in chemotherapy-induced peripheral neuropathy (CIPN).
- **Nanoformulation Strategy Validation:** The work strongly validates nanomedicine approaches (e.g., liposomal, PLGA-based OXA) as an effective strategy to decouple antitumor efficacy from neuropathic toxicity by altering drug biodistribution, specifically reducing platinum accumulation in the skin and subsequent inflammatory signaling.
- **Clinical Translation Potential:** Demonstrating superior antitumor efficacy coupled with significantly reduced neuropathic pain in a colorectal cancer model, OXA nanoformulations show high potential for clinical translation to improve the therapeutic index and patient quality of life during chemotherapy.
- **Broader Implications:** The findings suggest this fibroblast-nerve communication mechanism might extend to other platinum-based drugs and CIPN types.

姓名：张淑慧　　单位：中国科学院大学国家纳米科学中心　　邮箱：zhangsh2021@nanoctr.cn

中国科学院大学
University of Chinese Academy of Sciences

前沿交叉科学学院
School of Advanced Interdisciplinary Sciences

基于时间生物学的病原真菌防控靶点开发

卢悄佳[1,2†]，余慕群[1†]，孙宪昀[1,2†]，周欣[1]，张芮[1]，张亚豪[1,2]，刘晓兰[1]，李湛彪[3]，蔡磊1,2，刘宏伟[1]，李少杰[1,2]，党云琨[3]，徐小冬[4]，何群[5]，刘一[6]，刘晓[1,2*]

[1]中国科学院微生物研究所真菌学国家重点实验室，北京100101，中国。[2]中国科学院大学生命科学学院，北京100049，中国。[3]云南大学生命科学学院，昆明650091，中国。[4]河南大学生命科学学院作物应激适应与改良国家重点实验室，开封市，475004，中国. [5]中国农业大学生物科学学院农业部土壤微生物学重点实验室，北京市，100193，中国。[6]美国德克萨斯大学西南医学中心生理学系，达拉斯，TX 75390-9040

引言 Introduction

生物钟是保守的时间适应分子机器，利用昼夜节律来调整农业生产是符合绿色农业要求的新式技术。在病原体中，由于缺乏完善的分子机制，相关技术难以落地应用。我们通过解析尖镰孢菌（*Fusarium oxysporum*）生物钟系统，发掘基于时间生物学的抗病新靶点。

01 研究方法 Methods

- 基因表达分析：通过实时定量PCR（RT-qPCR）检测尖镰孢菌中FRQ同源基因（如FoFRQ1和FoFRQ10）的节律性表达，验证生物钟功能。
- 转录组学分析：在自由运行条件下进行时间序列转录组测序，识别24小时周期内振荡的节律基因。
- 突变体构建：构建生物钟核心组分突变体（如 *ΔFofrq1*、*ΔFowcc*），比较与野生型（WT）的基因表达差异。
- 致病性实验：在光暗周期下接种番茄幼苗，评估不同时间点（如宿主ZT0和ZT12）的感染严重程度，分析致病性的昼夜变化。
- 代谢物检测：使用高效液相色谱（HPLC）分析次级代谢物镰刀菌酸（fusaric acid）的生产水平。

02 研究结果 Results

- 尖镰孢菌拥有功能性生物钟，其中FoFRQ1是核心振荡器的主要调节器。
- 生物钟突变体（如 *ΔFowcc*）丧失致病性，而致病性表现出昼夜变异：当病原体与宿主节律同步时，感染严重度在黎明（病原体ZT0）最高；反之，在黄昏（宿主ZT12）峰值偏移。
- 转录组分析发现993个节律基因，富集于转录因子和代谢组分。转录因子FoZafA和FoCzf1受生物钟调控，是关键致病因子.
- FoZafA调节锌饥饿响应，突变体在锌缺乏条件下孢子产量显著降低；FoCzf1激活镰刀菌酸的生物合成，其生产在突变体中大幅减少。

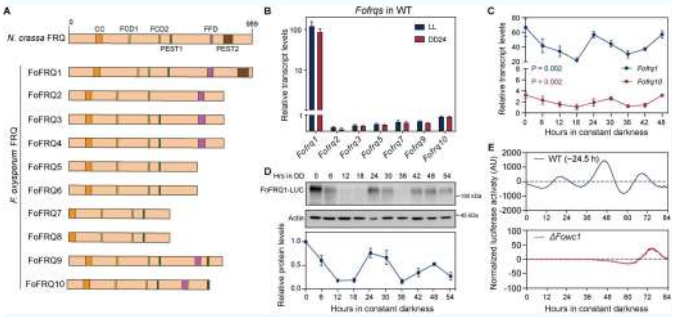

03 研究结论 Conclusion

- **尖镰孢菌生物钟是致病性的关键命令系统，通过协调锌饥饿响应和次级代谢来优化宿主入侵。**
- **生物钟调控的转录因子（如FoZafA和FoCzf1）使病原体适应宿主诱导的应激，并产生毒素代谢物。**
- **这些机制赋予尖镰孢菌绕过宿主防御、在最佳时间感染的能力，为抗病策略提供了新靶点。**

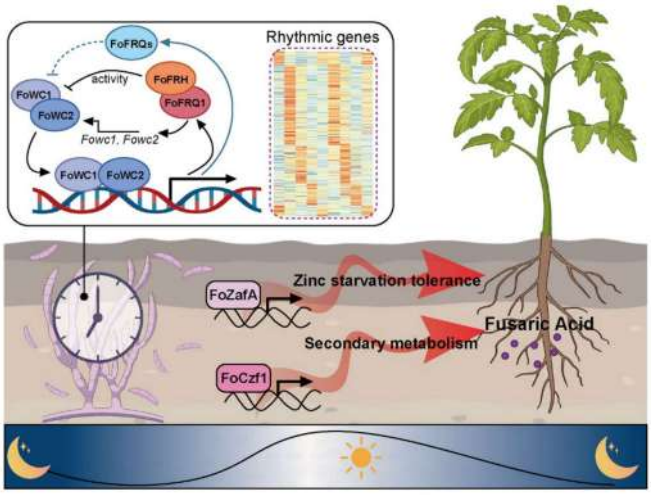

04 研究前景 Prospects

本研究揭示了生物钟在病原真菌致病性中的核心作用，未来可基于时间生物学开发新型抗病策略：

- **靶向生物钟组分：**利用生物钟调节剂干扰病原体节律，降低其致病性。
- **绿色农业应用：**通过调控作物光照周期或施用时间特异性农药，实现精准防控。
- **扩展研究：**探索其他病原真菌的生物钟机制，推动微生物组学和新陈代谢组学的交叉研究。

姓名：卢悄佳　　单位：中国科学院微生物研究所　　邮箱：luqj@im.ac.cn

中国科学院大学
University of Chinese Academy of Sciences

前沿交叉科学学院
School of Advanced Interdisciplinary Sciences

新型氮代谢途径直接氨氧化细菌的多样性

韩群， Gantuya Khasbaatar，王晓康，郑艳宁*，李德峰*

中国科学院微生物研究所，中国科学院大学，北京，100010

引言 Introduction

氮循环是维持生态系统平衡的关键过程，由多种微生物驱动。除典型的氨氧化细菌、古菌及厌氧氨氧化细菌外，部分异养菌如 *Alcaligenes* 也能氧化氨。近年来在 *Alcaligenes* 中发现的新途径——**直接氨氧化（dirammox）**，由谷氨酰胺合成酶 GlnA 与多酶系统 DnfABC 协同完成，将氨和有机氮直接转化为氮气。本研究通过基因组挖掘揭示携带 *dnfABC* 基因簇的微生物在分类学、基因结构及氮代谢途径上的广泛分布与多样性。

01 研究方法 Methods

1、*dnfABC* 基因簇的基因组挖掘与筛选策略

为系统揭示 *dnfABC* 基因簇分布特征与进化趋势，以 *Alcaligenes faecalis* JQ135 的 DnfABC为查询序列，使用 BlastP批量筛选潜在同源基因，并批量下载对应基因组。对阳性基因组进行基因簇结构比对，分析不同细菌属间 ORF 排列与基因方向差异，使用 ChiPlot可视化基因簇结构。

2. dnfABC 的系统发育分析

基于获得的同源序列，利用 ClustalW 进行多序列比对，并在 MEGA 12 中采用邻接法分别构建 DnfA、DnfB、DnfC 的系统发育树。所有系统发育树均通过 iTOL 进行可视化与注释，从而揭示 dnfABC 基因簇的进化关系。

3. 氮循环功能基因的通路识别

同时，为探究携带 *dnfABC* 的细菌在氮循环中的代谢潜能，基于 KEGG 中的同化性硝酸盐还原、反硝化作用、固氮、硝化、反硝化型硝酸盐呼吸及厌氧氨氧化等代谢途径。通过 BlastP比对所有基因组，仅当通路全部关键步骤均被检测到时才判定该途径存在。最终，根据不同氮转化途径的组合模式进行分类。

02 研究结果 Results

图1 潜在 dirammox 微生物的分类多样性

图 3 DnfABC 蛋白的系统发育树

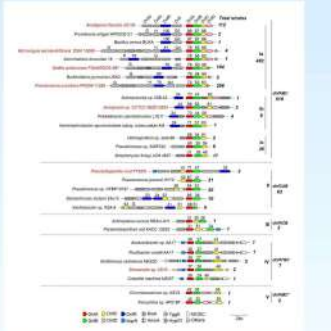

图 2 26 个代表属dnfABC 基因簇的结构排列

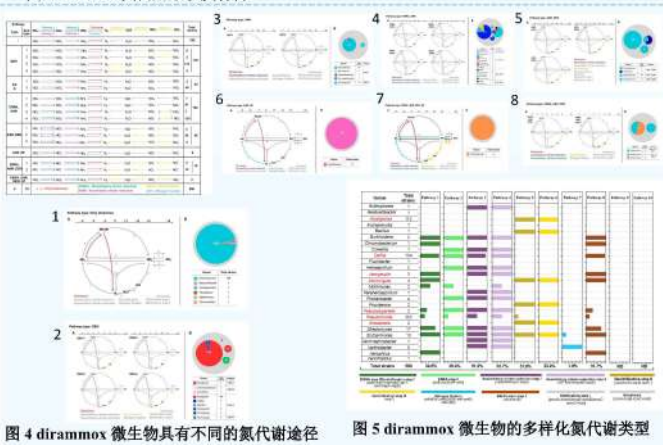

图 4 dirammox 微生物具有不同的氮代谢途径

图 5 dirammox 微生物的多样化氮代谢类型

03 研究结论 Conclusion

1、*dnfABC* 基因簇的广泛但不均匀的属间分布

通过基因组挖掘，发现携带 *dnfABC* 基因簇的细菌，隶属 3 个门、5 个纲、11 个目、17 个科、26 个属。主要分布于 *Pseudomonas*、*Alcaligenes* 和 *Delftia*，占总数 88%。其中 *Alcaligenes* 与 *Delftia* 的Rich factor最高，表明它们是典型的 dirammox 属。携带 dnfABC 的微生物广泛存在于陆地与水域环境，生态分布多样（图1）。

2、*dnfABC* 基因簇有五种排列类型

据统计，*dnfABC* 基因簇可依据三个 ORF 的排列顺序与方向分为五组（I–V）。不同组别在基因结构、调控元件及邻近基因上存在显著差异，表明各属间可能采用不同的氨氧化调控机制与功能策略（图2）。

3、DnfA、DnfB 和 DnfC 分化为三个主要进化支系

系统发育分析显示，DnfA、DnfB 和 DnfC 分化为三个主要支系（clade I–III），其分布与基因簇结构类型高度一致（图3）。

4、dirammox 与多种氮循环途径共存但不与硝化与厌氧氨氧化共存

经过分析，dirammox 可与硝酸盐同化还原、DNRA、反硝化及固氮途径共存，但未与硝化或厌氧氨氧化共现（图4）。进一步分析表明，这些菌株可依据不同氮代谢途径的组合分为八种类型，从仅含 dirammox 到同时具备四种氮循环途径（DNRA、同化还原、反硝化与固氮）（图5）。这种多样的途径组合揭示了 dirammox 在连接多种氮转化过程中的生态重要性。

04 研究前景 Prospects

作为继硝化与厌氧氨氧化之后发现的氨氧化途径，dirammox 展现出广泛的分布与显著的功能多样性。本研究系统分析*dnfABC* 基因簇，发现 dirammox 微生物分布于 26 个属，主要隶属于变形菌门，但仅在 *Alcaligenes*、*Delftia* 与 *Microvirgula* 等少数属中呈高丰度。携带 *dnfABC* 的菌株来自土壤、水体及动植物环境，表明其生态适应性极强。dirammox 可独立将氨氧化为氮气，也可与硝酸盐同化还原、DNRA、反硝化或固氮等途径共存，揭示了其在氮循环中的关键作用。综上，dirammox 微生物可能在多种生态系统中承担比以往认识更广泛的氮转化功能，值得进一步的生态学研究与环境监测。

姓名：韩群　　单位：中国科学院微生物研究所　　邮箱：hanq@im.ac.cn